Strong field ionization of atoms and molecules studied by phase-of-the-phase spectroscopy

Dissertation zur Erlangung des akademischen Grades
doctor rerum naturalium (Dr. rer. nat.)
der Mathematisch-Naturwissenschaftlichen Fakultät
an der Universität Rostock

vorgelegt von

Slawomir Skruszewicz

aus Brześć Kujawski

Rostock
August 2015

https://doi.org/10.18453/rosdok_id00002461

Betreuer: Prof. Dr. Karl-Heinz Meiwes-Broer (Institut für Physik, Universität Rostock)
PD Dr. Josef Tiggesbäumker (Institut für Physik, Universität Rostock)

Gutachter: Prof. Dr. Markus Drescher (Institut für Laserphysik, Universität Hamburg)
PD Dr. Josef Tiggesbäumker (Institut für Physik, Universität Rostock)

Datum der Einreichung: 21.08.2015
Datum der Verteidigung: 07.01.2016

Dedicated to my beloved parents, grandmother and family

"And a new philosophy emerged called quantum physics, which suggest that the individual‘s function is to inform and be informed. You really exist only when you‘re in a field sharing and exchanging information. You create the realities you inhabit."
Timothy Leary, *Chaos & Cyber Culture*

Abstract

Coherent superposition of a fundamental 800 nm (ω) laser field with its second-harmonic (2ω) generates laser pulses with asymmetrical electric field distribution. Controlling a time-lag between the ω-2ω fields with sub-fs precision enables for electron trajectory tagging. Here, we propose two-color *phase-of-the-phase spectroscopy* ($\mathcal{P}o\mathcal{P}$) which applied to rare gas atoms provides relative-phase-tagged photoelectron spectra. We show that a relative phase contrast (RPC) and the-phase-of-the-phase (PP) obtained from Fourier transformed electron spectra gain information which are beyond conventional photoelectron spectroscopy. Applying simple trajectory model including wavepacket spreading and multiple rescattering the universality of the rescattering process is demonstrated. Detailed inspection of PP and RPC spectra reveals target sensitive features which can be used to extract structural or even dynamical information with high accuracy. As a first applications of $\mathcal{P}o\mathcal{P}$ we study ionization of randomly oriented CO_2 and N_2 molecules. We perform *in situ* measurements of the Gouy phase shift in the focal volume. Finally, we demonstrate that $\mathcal{P}o\mathcal{P}$ enables to discriminate thermal contributions in C_{60} thus emphesizing phase-dependent effects.

Kurzzusammenfassung

Die kohärente Überlagerung eines Laserfeldes von 800 nm (ω) mit seiner zweiten Harmonischen (2ω) erzeugt Laserpulse mit asymmetrischen Verteilung des elektrischen Feldes. Die Kontrolle des Phasenzeitunterschieds zwischen den ω-2ω-Feldern mit Sub-fs-Präzision ermöglicht das tagging von Elektronen-Trajektorien. Unser Vorschlag umfaßt eine zweifarbige *phase-of-the-phase spectroscopy* $\mathcal{P}o\mathcal{P}$ welche bei Anwendung auf Edelgasatome Photoelektronenspektren in denen der Beitrag der relativen Phase sichtbar wird. Aus den Fourier-transformierten Photoelektronenspektren erhält man den relativen Phasenkontrast (RPC) und die phase-of-the-phase (PP), welche mehr Informationen liefert als die konventionelle Photoelektronen-Spektroskopie. Ein einfaches Elektronentrajektorien Modell unten Berücksichtigt der, Dispersion des Wellenpakets und Mehrfach Rückstreuung zeigt eine Universalität des Rückstoß-Prozesses die sich in allen Spektren den Edelgas Atomen wieder findet. Die detaillierte Analyse der PP und RPC Spektren offenbart target-spezifische Eigenschaften, aus denen sich Informationen zur Struktur und sogar zur Dynamik mit hoher Genauigkeit ableiten lassen. Als erste Anwendung der $\mathcal{P}o\mathcal{P}$,-Methode haben wir die Ionisation beliebig orientierter CO_2- und N_2-Moleküle untersucht. Dabei wurden *in situ*-Messungen der Gouy-Phasenverschiebung im Brennpunkt des ω-2ω-Laserpulses durchgeführt. Schlussendlich erlaubt die $\mathcal{P}o\mathcal{P}$-Methode die Unterdrückung thermischer Anteile von C_{60}.

Contents

Introduction

Rapid development in laser technology enables the probing of the dynamics of quantum systems in real time. Modern techniques exploit coherence properties of light and quantum-mechanical matter properties which enables the driving of a quantum system to the desired dynamical behaviour [1; 2]. When matter is exposed to light, the electrons react instantaneously to the electric field. Other degrees of freedom are then affected indirectly due to electric charge redistribution. Controlling of electron motion requires the generation of waveforms that tailor the instantaneous electric field on sub-fs time scales. Hence, these waveforms permit access to attosecond physics [3; 4] and femtochemistry [5; 6; 7]. Short laser pulses can be generated over almost the entire spectral range, which is relevant to modern spectroscopy methods. Coherent laser sources, e.g., commercially available Ti:Sapphire laser systems, enable the creation of laser pulses as short as a few fs, consisting of only a few electric field oscillations in the visible and near-IR range [8; 9]. Single-cycle THz radiation from free-electron lasers possesses electric fields strong enough to be employed for a variety of studies [10; 11]. The shortest pulse ever generated by such systems in high- harmonic generation processes HHG in the XUV range have durations of 67 as [12]. Free-electron lasers deliver pulses in the hard X-ray spectral range with durations of 100 fs [13; 14; 15; 16]. Today, physics has reached the point where tailoring of laser pulses on sub-fs time scale has become routine [17; 18; 19; 20]. This permits active manipulation the quantum pathways that lead to certain classes of physical and chemical phenomena, and paves the road towards attosecond control and metrology [21; 22].

Controlling system dynamics with a laser field has been proposed theoretically by Shapiro-Brummer [23; 24] and Tannor-Rice [25; 26]. In the frequency-resolved scheme, the two cw laser fields of frequency ω_1 and $\omega_3 = 3\omega_1$ establish two alternative pathways that the optical transition can follow. By tuning their relative phase, quantum interference between different pathways from a the ground to the final state permits control of the branching ration of the products. The frequency-resolved scheme has been demonstrated in the control of autoionization and predissociation in HI and DI molecules [27; 28]. Alternatively, the time-resolved scheme (often called pump-dump) benefits from time-dependent motion of wave packets prepared by fs laser pulses. Experimentally, the time-resolved scheme has been observed in the selective population of two excited states of I_2 [29]. Over last decade many other schemes for coherent control have been developed [30; 31].

In the past decade, a great many experimental studies have been dedicated to the investigation and control of electron dynamics on natural motion time scales. One elementary example is the superimposition of a carrier wave and a second-harmonic of adjustable amplitude and phase [32; 33]. An attosecond streaking technique has been established by a combination of high-harmonic radiation (attosecond pulse train)[34] with a few-cycle laser field [35; 36; 37; 38]. Such an attosecond transient recorder makes internal atomic process accessible to human perception [36; 39; 40]. The most sophisticated techniques rely on the coherent combination of several laser sources, reaching bandwidths of well over an octave. This permits the synthesising of pulses with arbitrary temporal evolution [41; 42].

Coherent superposition of two laser pulses of different frequencies (two-color laser pulses) has been utilized to control ionization of atoms in intense fields. The precise tuning of a time lag between the fundamental Nd:YAG laser and its second harmonics, which are generated in non-linear crystal, demonstrates control of the ionization rate in Xe [43]. Schumacher *et al.* studied ionization in a two-color field and showed that the observed phase dependencies in above-threshold ionization peaks cannot be explained in the context of a two-step model that includes the optical tunnelling and subsequent propagation of an electron in the laser field [44]. After a decade-long hiatus, a growing number of experiments dedicated to two-color ionization have been performed. The fundamental output of a Ti:Sapphire laser with its second harmonic polarized parallel or perpendicular is typically employed to sculpt a laser field to sub-fs precision, permiting access to fs physics and chemistry. Experiments involving two-color excitation have addressed all important aspects of strong field ionization: high harmonic generation [45; 46; 47; 48; 49; 50; 51; 52; 53; 54], non-sequential double ionization [55; 56; 57; 58; 59], directed photoemission [33; 59; 60; 61; 62; 63; 64; 65; 66], non-adiabatic molecule alignment [54; 67; 68; 69; 70; 71; 72], and control over dissociation and fragmentation [70; 73; 74; 75]. In a pioneering experiment Dudovich *et al.* demonstrated control over even and odd HHG processes [47]. By tuning the time delay between SHG and the fundamental beam, dynamical electron recombination can be controlled with sub-fs precision. Another experiment addressed the problem of the ionization and rescattering times. High-harmonic generation from CO_2 molecules exposed to an orthogonally polarized two-color laser field enables the encoding of subtle delays in ionization times from two orbitals from the CO_2 molecule [53]. Orthogonally polarized two-color laser pulses can be used to control the motion of tunnelling electrons in both space and time [60]. Photoelectron studies are mostly performed in the deep perturbative range where SHG not only significantly perturbs the photoelectron trajectories but also ionizes the system. Xie *et al.* show that the phase of a transiently excited bound wave packet created by two-color laser induced excitations can be retrieved from momentum-resolved photoelectron spectra with attosecond precision [62]. In the angularly-resolved photoemission study of Xe in a two-color laser field, Ray *et al.* demonstrated that by rescattering part of the photoelectron spectrum, a much more robust determination of the relative phase of the two colors can be obtained, compared to the use of direct photoelectrons [61].

Recently, two-color laser pulses as well as CEP have been utilized in our group to study the impact of the collective resonance of a metal cluster on electron acceleration [76]. Strong phase-dependencies have been obtained in both cases. The first studies prove that a sculpted laser field is capable of controlling the dynamics on a sub-cycle time scale.

Information about dynamics of the process is often encoded in a non-obvious manner in electrons, ions and photons emitted following irradiation. Careful modeling is necessary to retrieve dynamical information about the underlying phenomena. A numerical solution of the time-dependent Schrödinger equation (TDSE) is the most accurate formalism to describe non-relativistic electron dynamics in a strong laser field. Due to computational requirements, solutions are practically limited to the single-active electron problem. Although TDSE calculations reproduce features observed experimentally to a high precision, they provide little physical insight since the calculation itself is a numerical experiments. A great simplification of the numerical problem is achieved by semi-classical electron trajectories methods which are outlined in the simple man's theory (SMT) [77; 78; 79; 80]. In the SMT framework, the fundamental physics behind most of the relevant strong-field phenomenacan be described by an electron dynamical model consisting of three steps: (i) optical tunneling, (ii) acceleration in the laser field, and (iii) rescattering/recombination with the parent ion. Semi-classical electron trajectories derived from this approach greatly simplify and unify most of the strong-field phenomena.

Within project A5 of Sonderforschungsbereich (SFB) 625, this thesis addresses the problem of ionization and electron rescattering dynamics in atoms and molecules exposed to strong two-color (ω-2ω) laser fields. Our aim is to introduce small perturbations by the ω-2ω field that do not ionize the system and only slightly modify ionization and rescattering times. The fundamental physics behind these processes is modelled by SMT. A simple classical-trajectory-based model which describes the most important physical phenomena influencing electron rescattering processes in strong laser fields used in this thesis has been developed by Dieter Bauer. Strong-field approximation (SFA) calculations and Coulomb-Volkov corrected SFA (CVSFA) calculations give insight into the mechanisms that are not included in SMT, e.g., the influence of the interference effects between propagating wavepackets; these calculations are performed by Mohammad Adel Almajid (AG Bauer), who also implemented CVSFA. Computationally demanding TSDE calculations are performed by Mathias Arbeiter and Thomas Fennel.

The presented work proceeds as follows:

- Chapter 1 gives an overview of the principal ionization and rescattering dynamics in a strong laser field. We briefly introduce laser techniques which enable control of the electron dynamics in atomic systems.
- Chapter 2 summarizes the theoretical models used to analyse the experimental data. The analytical simple man's theory (SMT) model is developed to render the basic physical mechanisms that impact rescattering dynamics. We describe semi-analytical strong-field approximation (SFA) models together with Coulomb–Volkov SFA (CVSFA) models.
- Chapter 3 introduces the experimental techniques employed in this work. A velocity-map imaging spectrometer (VMI) designed to resolve high energy electrons (1 keV) is tested via ionization of Ne with soft X-ray synchrotron radiation. We describe the optical setup that enables the synthetization of a phase-controlled two-color laser field with sub-fs precision. Finally, we introduce a new method to analyse ω-2ω phase dependent photoelectron spectra, which we dub 'the-phase-of-the-phase' ($\mathcal{PoP}$) method. The $\mathcal{PoP}$ technique quantifies the separation of a relative-phase-dependent photoelectron signal into phase-of-the-phase (PP) and relative-phase-contrast (RPC) spectra.
- Chapter 4 reviews the experimental results from a study of strong field $\omega/2\omega$ ionization of rare gas atomic targets. We discuss experimentally obtained PP and RPC spectra, and compared them with the prediction of SMT, SFA and TDSE.
- Chapter 5 presents a few potential applications of the $\mathcal{PoP}$ technique to the study of controlled emission from molecular systems (N_2, CO_2 and C_{60}) and Gouy phase shift.

1 Theoretical Background

This section gives a brief introduction into a free electron dynamics in a strong oscillatory laser field. Three ionization models of atomic system exposed to a strong oscillatory laser field strong laser field are discussed. Next, an influence of a parent ion on the electron dynamics and its consequences are introduced. Subsequently, three experimental results of other groups which demonstrated control of the ionization and recombination of electrons are shown. Momentum-resolved photoelectron study are in the central point of present work. Thus, short description of typical spectral features and their origin are introduced. Finally, basics related to the focusing of the laser beam are described.

1.1 Free electron dynamics in strong laser fields

A free electron subjected to a spatially dependent oscillating electric field $\mathbf{E}(r,t) = \mathbf{E_0}(r)\cos(\omega t)$ follows an oscillatory motion that can be described by Newton‘s classical equation of motion:

$$m_e\mathbf{a} = -eE(\mathbf{r},\mathbf{t}) \tag{1.1}$$

where $\mathbf{E_0}(r)$ is the field amplitude at position r, m_e is the electron mass and ω stands for the angular frequency of the laser field. To neglect spatial dependencies of the electric field, one can expand it into a Taylor series around the initial position of the electron r_0:

$$\mathbf{E}(\mathbf{r}) = \mathbf{E}(\mathbf{r_0}) + (\mathbf{r}\cdot\nabla)\mathbf{E}|_{r=r_0} + \dots \tag{1.2}$$

and neglect higher-order terms, obtaining the first-order electron trajectory in the oscillating electric field:

$$\mathrm{r(t)} = \frac{\mathrm{e\,E_0}}{\mathrm{m_e}\omega^2}\cos(\omega\mathrm{t}) = \mathrm{r_0}\cos(\omega\mathrm{t}) \tag{1.3}$$

with the amplitude $\mathrm{r_0}$, which is of the order of $\sim 1\,\mathrm{nm}$ for optical frequencies and intensities $10^{13}\dots10^{14}\ \mathrm{W/cm^2}$. The cycle-averaged kinetic energy is called the ponderomotive energy:

$$U_p = \frac{e^2 E^2}{4m\omega^2} \tag{1.4}$$

In general, it is more convenient to express the ponderomotive energy U_p as a function of the wavelength λ and laser intensity I [81; 82]:

$$U_p[\mathrm{eV}] = 9.3 \times 10^{-14} I\,[W/cm^2]\,\lambda^2\,[\mu\mathrm{m}] \tag{1.5}$$

This situation reflects the free-electron motion in a homogeneous field. By performing the necessary substitution and averaging over time, one obtains the effective nonlinear force acting on a free electron introduced into a non-homogeneous electromagnetic field.

$$\mathbf{F} = -\frac{e^2}{4m\omega^2}\nabla\mathbf{E}^2 \tag{1.6}$$

where $\mathbf{E}^2$ indicates the time-averaged square of the electric field. This effective force, also called the **ponderomotive force** accelerates an electron towards the area of least electric field, i.e. against the gradient of the cycle-averaged intensity [83; 84]. If the pulse duration persists long enough($\tau_p \geq 1\,\mathrm{ps}$), the electron leaves the laser focus and gains additional translational kinetic energy equivalent to the ponderomotive energy, see Eq. (1.4).

1.2 Strong field ionization of atomic systems

According to Einstein's theory of light quanta, a photon can ionize matter if its energy is greater than the ionization potential $\hbar\omega \geq I_p$ [85]. Upon absorption of energy and angular momentum from the ionizing photon, an electron transitions into a continuum state. Ionization of matter with photons of energy much smaller than the ionization potential $\hbar\omega \ll I_p$ requires a high photon flux, which can be achieved practically using pulsed laser sources. Only then, a photon flux within the short burst of radiation (typically $t_{pulse} = 1\mathrm{ns}\ldots 1\mathrm{fs}$) is high enough to assure multiphoton absorption between laser-induced virtual states and subsequent ionization [86].

Ionization in a strong oscillatory laser field has been described theoretically by Keldysh [87]. To quantify the conditions between multiphoton absorption and optical tunnelling in a very strong field, an adiabaticity parameter γ_k, also called the Keldysh parameter, has been introduced. The Keldysh parameter is defined as the ratio between tunnelling time τ_t and a half period of the laser field oscillation τ_L; equivalently, it can be expressed by I_p and U_p [88]:

$$\gamma_k = \sqrt{\frac{\tau_t}{1/2\tau_L}} = \frac{\omega\sqrt{2m_e I_p}}{eE} = \sqrt{\frac{Ip}{2U_p}} \tag{1.7}$$

In the following, the ionization mechanisms are briefly described and classified with the Keldysh parameter.

1.2.1 Multiphoton ionization $\gamma_k \gg 1$

Multiphoton ionization (MPI) refers to a process in which an electron overcomes the binding Coulomb potential by absorption of n photons simultaneously, as shown in Fig. 1.1(a). According to the Heisenberg energy–time uncertainty principle $\Delta E \Delta t \geq \hbar/2$, the laser-induced virtual state related to the laser photon energy ΔE and its harmonics can exist within a time at most $\Delta T = \hbar/2\Delta E$. A Ti:sapphire laser photon with energy $\mathrm{E} = 1.55\,\mathrm{eV}$ induces a virtual excited state existing as long as $\Delta t < 2.12 \cdot 10^{-16}\,\mathrm{s}$ which is an order of magnitude lower than the oscillation period of the electric field. Thus, the electronic transition occurs within a fraction of an optical cycle and can be understood as n transitions between n virtual states [89].This scenario is valid if laser frequencies are much higher than the tunnelling time (e.g. XUV) and for low laser intensities, e.g. $10^9 - 10^{12}\,\mathrm{W/cm^2}$. In a non-resonant MPI, an electron is directly transferred into the continuum, i.e. it does not populate any bound excited state. The scaling law based on perturbation theory [90; 91] implies that the n-photon ionization probability is proportional to the n-th power of the ionizing laser intensity [84; 92].

$$\Gamma_{MPI} = \sigma_n I^n \tag{1.8}$$

In resonantly enhanced MPI (REMPI), the excited state can be populated when the energy of an integral number of photons approaches the energy of an allowed electronic transition. Alternatively, they can be shifted into resonance by the AC Stark shift [93; 94; 95]. High-lying excited states, e.g. Rydberg states, are shifted by an energy equivalent to the ponderomotive energy[96; 97]. The laser intensity characteristic for REMPI is $I \sim 10^{13}\,\mathrm{W/cm^2}$, where the ponderomotive energy reaches the order of $1\,\mathrm{eV}$. The REMPI channel usually dominates the photoelectron spectra because of the enhanced ionization cross-section [98; 99]. If an electron absorbs more photons than are required for ionization, the above-threshold ionization (ATI) is established [100]. Upon absorbing m additional photons above I_p, an electron is released into the continuum with an excess energy $E_{kin} = (n+m)\hbar\omega - I_p$. Characteristic features of ATI are a series of equally spaced rings in an angle-resolved photoelectron spectrum, see Fig. 1.10 (2).

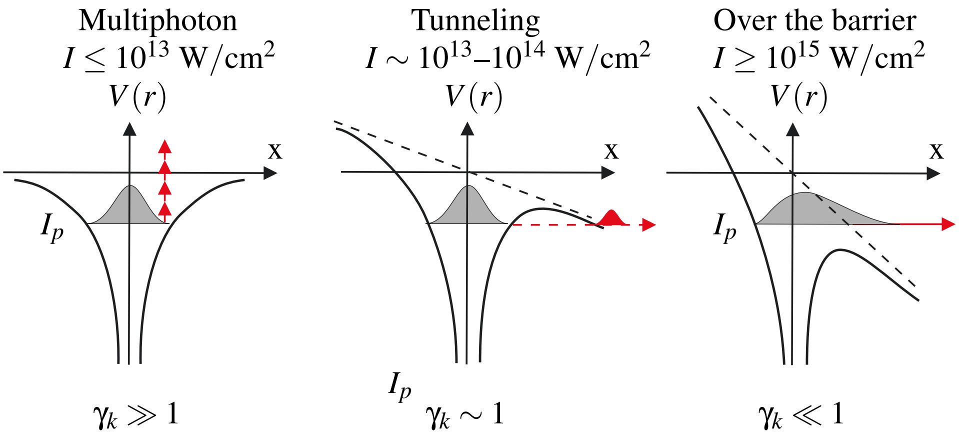

Figure 1.1: Ionization of an atom in a strong laser field classified by Keldysh parameter γ_k. (a) In the multiphoton range, ionization proceeds by absorption of discrete photons. (b) By increasing the laser intensity ($I > 10^{14}$ W/cm^2), the electric field associated with an intense laser pulse becomes comparable with the binding electric field. As a result, it turns the Coulomb potential into an effective tunnelling barrier. In case (c) the Coulomb barrier is suppressed so strongly that the electron is no longer bound.

1.2.2 Tunnel ionization $\gamma_k \approx 1$

The electric field of the laser pulse can turn the Coulomb potential into a tunnelling barrier, as shown in Fig. 1.1 (b). Tunnelling ionization sets in typically at intensities of $10^{14} - 10^{15}$ W/cm^2. Substantial ionization occurs within a fraction of an optical cycle, and the electric field can be regarded as quasi-static on the tunnelling time scale [101]. Landau derived the tunnelling probability from an atom through a triangular barrier that can, however, be used to calculate the ionization probability from hydrogen in the ground state. The general equation for a complex atom or atomic ion in an arbitrary state has been derived by Ammosov, Delone and Krainov (ADK rate) [102].

$$w[a.u.] = (2l+1)\left(\frac{3Fn^{*3}}{\pi Z}\right)^{1/2}\frac{Z^2}{4\pi n^{*3}}\left(\frac{2e}{n^*}\right)^{2n^*}(l+|m|)!\times \left(\frac{2Z^3}{Fn^{*3}}\right)^{2n^*-|m|-1}\frac{1}{2^{|m|}|m|!(l-|m|)!}\exp\left(\frac{-2Z^3}{3n^{*3}F}\right) \tag{1.9}$$

where l is orbital quantum number, m is magnetic quantum number, n^* is effective principal quantum number, Z is total charge of the system, F is electric field strength associated with the laser pulse and e indicates electron charge.

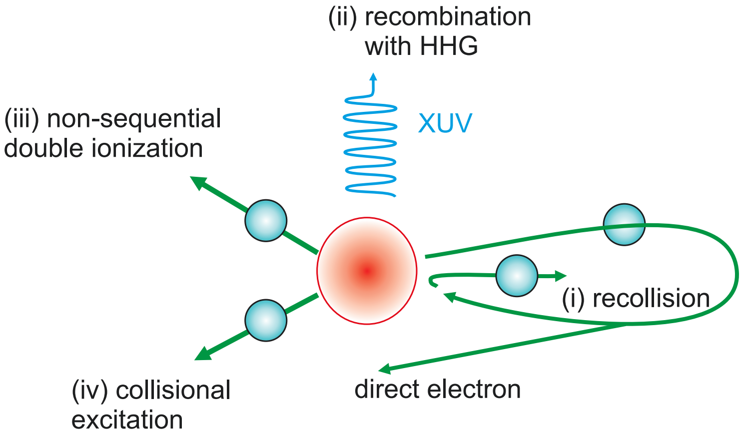

Figure 1.2: Electrons driven by a strong laser field in the vicinity of an atom: Upon optical tunnelling ionization, the electron dynamics is influenced by the parent ion. By elastic recollision (i) the electron can gain energy up to $10U_p$ from the laser field. Recombination (ii) results in high-harmonic generation. In the case of non-elastic recollision, the electron transfers part of its momentum to the parent ion, which results in (iii) additional ionization or (iv) collisional excitation. The figure is adapted from [4].

1.2.3 Over the barrier ionization $\gamma_k \ll 1$

As the laser intensity is increased further, $I > 10^{15}\,\mathrm{W/cm^2}$ ($\gamma \ll 1$), a local maximum of the effective tunnelling potential is suppressed below the ground state. Consequently, the electron is no longer bound and escapes from the atomic potential. This process is known as over-the-barrier-ionization (OBI) and occurs in atomic hydrogen at 1.4×10^{14} $\mathrm{W/cm^2}$ [101]. A threshold or "critical intensity" for OBI is given by:

$$I_{OBI}[W/cm^2] = \frac{\pi^2 c \varepsilon_0^3 I_p^4}{2Z^2 e^6} = 4 \times 10^9 (I_p[eV])^4 Z^2 \tag{1.10}$$

It might be surprising that the critical intensity value for the hydrogen atom is far below the value corresponding to the Coulomb field ($3.5 \times 10^{16}\,\mathrm{W/cm^2}$ at the mean ground-state electron radius. However, it is already high enough to push the distorted potential's local maximum down to the level of the ground state and allow the electron to leave the atom.

1.3 Electron dynamics in the ion vicinity

The presence of a parent ion significantly influences the electron dynamics in a strong laser field. According to the semi-classical two-step model [103], the electron upon

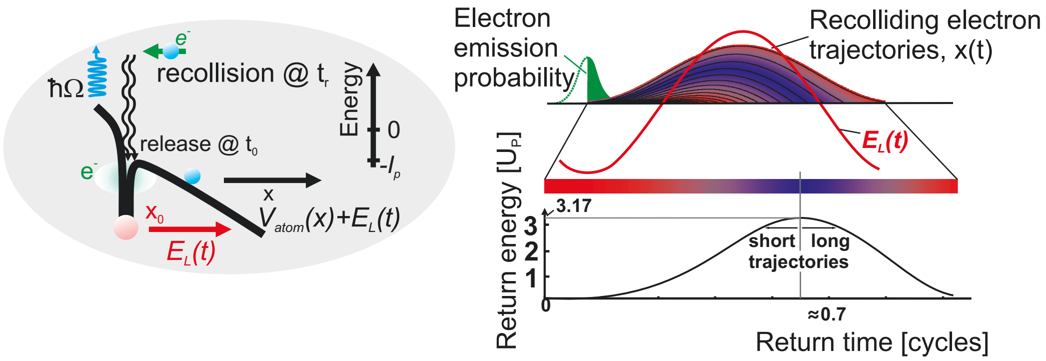

Figure 1.3: High-harmonic generation (HHG) driven by an intense laser field (left). The electron tunnels through a suppressed Coulomb barrier, gains energy in the laser field and is driven back to its parent ion. Recombination into a bound state results in XUV photon generation. Classical recolliding electron trajectories (right). For a given energy there are two contributing trajectories (long and short) that can interfere constructively or destructively. The figure is adapted from [4].

optical tunnelling propagates in an oscillatory laser field. Subsequent propagation is treated classically assuming interactions with the electric and magnetic field of the laser pulse and neglecting the Coulomb field of the parent ion. Further simplification results from the dipole approximation, which neglects magnetic field effects, as described in Section 1.1. Corkum proposed a third step in which the electron is accelerated back and recollides (i) or recombines (ii) with the parent ion [77]. Thus, a three-step model has been established that is schematically illustrated in Fig. 1.3. The recollision process includes a set of physical phenomena observed in the past two decades, such as high-harmonic generation (HHG) or non-sequential double ionization (NSDI). A brief description of the most important processes is given below.

Recombination and high-harmonic generation (HHG)

Focusing of an intense laser pulse with frequency ω_1 on an atom results in generation of high harmonics with frequency $n\omega_1$ [104]. For atomic systems ionized with linearly polarized field, radiation from only $n = 1,3,5...$ is possible. The physical mechanism behind HHG based on a three-step model as illustrated in Fig. 1.3 (left). Upon optical tunnelling and propagation in the laser field, the electron turns back towards the parent ion and recombines with the hole in the valence level, emitting an XUV photon. HHG radiation is emitted along the propagation direction of the driving field [105]. Recolliding electrons that lead to HHG are released within a small time interval. Trajectories resulting in HHG emission calculated from the three-step model for ionization with linearly polarized light are shown in Fig. 1.3 (right) [4]. The tunnelling probability (green) is given by the ADK rate. There are a few important points coming out of this scenario.

The electron excursion and return time are uniquely determined by the ionization time. Depending on the ionization time, the electron returns, gaining kinetic energy up to $3.17\,U_p$ (color bar) with U_p ponderomotive energy given in Eq. 1.5 [77; 106; 107]. This is the well-known cut-off energy for HHG generation. The maximum photon energy upon recombination with the hole in the ground state is thus $h\nu = 3.17\,U_p + I_p$, where I_p is the ionization potential of the atom [105]. Finally, for any given return energy (except $E_{max} = 3.17\,U_p$) there exist two classical trajectories along which the electron can gain the same amount of kinetic energy. They are commonly called *short* and *long* trajectories. Constructive and destructive interference between them is reflected in the signal intensity distribution in the HHG spectrum.

The selection rules for HHG are determined by the combined symmetry of the system target and laser field. If the symmetry is broken either for the target or for the laser field, even harmonics are generated. Recently, generation of even harmonics has been reported for an polyatomic asymmetrical molecule, i.e. CH_3F [72]. Dudovitch *et al.* demonstrated the control of even-harmonics generation in a combined two-color laser field [47]. HHG generation has been reported for atoms, molecules, clusters, surfaces and relativistic plasma. It is possible to reconstruct molecular orbitals from an evaluation of the HHG emission [108].

Elastic scattering

Electrons that scatter elastically from their parent ion are released within a very narrow time window close to the electric peak maximum. The most profound consequence is that electrons gain energy while being elastically scattered. In the classical framework of Simple Man's Theory, electron trajectories relevant for elastic scattering and HHG are the same [112]. Thus, in analogy to the HHG process they can be dubbed *short* and *long* trajectories depending on the excursion they make from their parent ion.

In Fig. 1.4 three types of trajectories are depicted that contribute to the photoelectron spectrum seen by a detector located on the right [111]. The electron most probably tunnels through an effective potential $E_{eff}(z) = -e^2/z - eF(t)z$ (grey surface) near the laser peak. Tunnelling happens twice per laser period T. Subsequently, electrons are driven by the effective field and can reach the detector upon recollision with the ion core or directly. Depending on the electric field phase they are released towards the detector (direct and back-scattered electrons) or opposite to it (forward-scattered electrons). Direct electrons (red) do not rescatter and contribute to the low-energy part of the spectrum ($E_{kin} < 2\,U_p$). Back-scattered electrons (green) contribute to a weaker but broad high-energy plateau ($E_{kin} < 10\,U_p$). Forward-scattered electrons are turned back towards the detector and appear in the low-energy region of the spectrum ($E_{kin} < 2\,U_p$). Detailed discussion of this process is continued in Chapter 2.

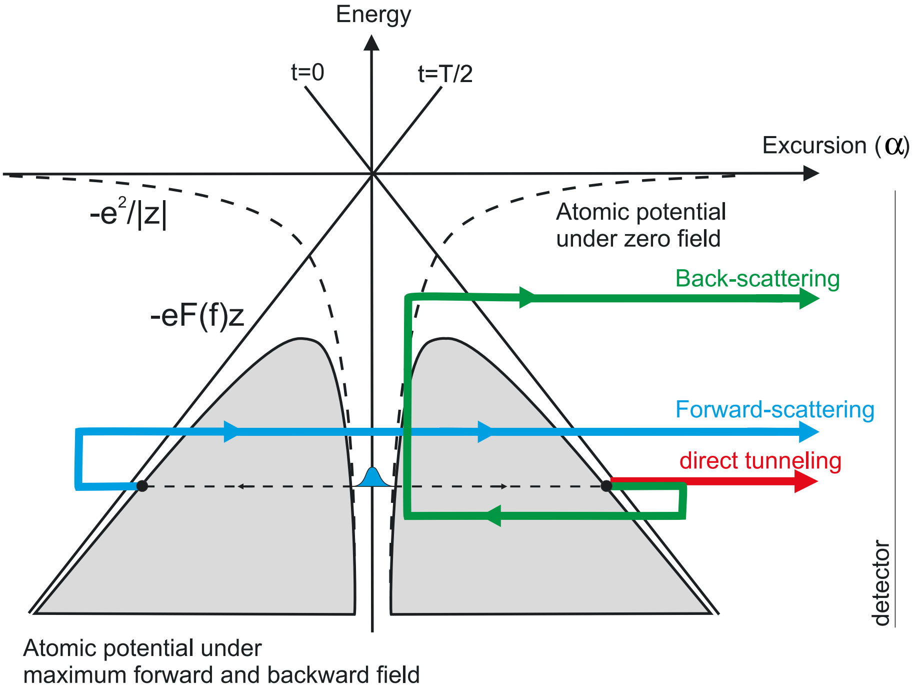

Figure 1.4: Optical tunnelling ionization and elastic rescattering in intense laser fields. Tunnelling occurs twice per laser cycle (T) when the laser field (-eF(t)z) reaches a maximum. Electrons driven by the laser field can arrive at a detector (right) either directly or upon rescattering. Direct electrons contribute to the low-energy structures in the spectrum with classical $2U_p$ cut-off. Back-scattering creates a less intense but broad high-energy plateau with $10U_p$ cut-off [109; 110]. Forward-scattered electrons contribute to the low-energy ($< 2U_p$) part of the photoelectron spectrum. The picture is adapted from [111].

Inelastic scattering

Recolliding electrons can transfer part of their kinetic energy in inelastic collisions. It is the most intuitive example of laser-driven multielectron dynamics in an atomic system [113; 114; 115]. If the energy transfer is high enough, a recolliding electron directly promotes a bound electron via electron-impact ionization, as indicated in Fig. 1.5(left). Because of momentum conservation, both electrons propagate in the same direction. In the other scenario, the recolliding electron excites the parent ion, which is subsequently ionized by the laser field (Fig. 1.5(right)) [116; 117]. The recollision-induced excitation with subsequent ionization (RESI) constitutes the dominant channel for non-sequential double ionization (NSDI) [77]. Recently, this process has been confirmed in an experiment involving CEP laser pulses [118].

In general, high-intensity laser–matter interaction depends on the electric field of the laser pulse which ionize and drives propagating electron wavepackets. Most of the phenomena, e.g. HHG, ATI, NSDI can be understood in terms of classical electron tra-

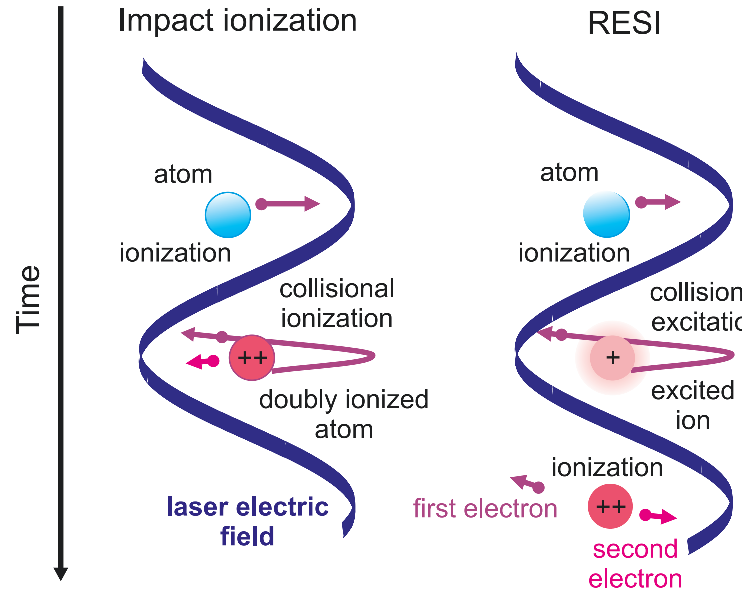

Figure 1.5: Inelastic scattering process in an atom results in non-sequential double ionization. If momentum transfer is high enough, a second electron can be directly promoted to the continuum via electron-impact ionization (left). In RESI (right), the colliding electron excites the parent ion, which can subsequently be ionized in the next cycle of the laser field.

jectories. Because electron motion is sensitive to the electric field of the laser pulse, by manipulating the laser pulse form, particular channels can be controlled. In the following, the control methods are briefly discussed.

1.3.1 Coherent control

Controlling a quantum system's dynamical behaviour is possible due to the rapid development of laser technology. Nowadays, control of the laser pulse form on the sub-fs time scale has reached the status of daily routine [17; 18]. This enables the active manipulation of the quantum pathways that lead to certain classes of physical and chemical phenomena.

Two basic mechanisms leading to coherent control are schematically illustrated in Fig. 1.6. Brummer and Shapiro investigated theoretically a frequency-resolved scheme (left). Two monochromatic laser beams with commensurate frequencies are employed to populate the excited state $|f\rangle$ by two interfering pathways. By tuning the laser intensity and phase outcome, the product can be controlled. Second, the time-resolved scheme, often called pump–dump (right) benefits from the time-dependent motion of the wave packets prepared by fs laser pulses. Experimentally, it was observed in the pump–probe scheme by selective population of two excited states in I_2 [29]. Many

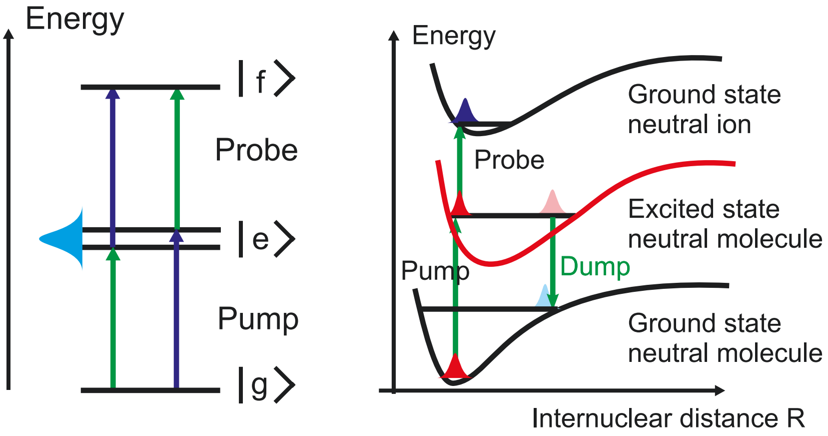

Figure 1.6: Theoretical models of quantum control proposed by Brumer-Shapiro (left) and Tannor-Rice (right). In frequency-resolved scheme (left) two monochromatic laser beams populate state $|f\rangle$ by two interfering pathways. Time-resolved scheme (right) benefits from the time-dependent motion of wavepacket prepared by fs laser. The figure is adapted from [4].

schemes of coherent control have been developed in the past decade ([31] and references therein) showing that by combination of two fields it is possible to study and control electron dynamics with sub-fs precision, which is its natural motion time scale. Two-pathway coherent control was demonstrated with atomic bound–bound transitions in the $\omega/3\omega$ experiment [119]. Bound–free transition control in photoionization with $\omega/2\omega$ fields has been reported in many experiments. Yin *et al.* observed phase-dependent electron angular distributions resulting from quantum interference between even- and odd-parity electron wave functions [120]. Control of the ATI signal has been achieved in Kr [43; 44]. Both groups report on phase-dependent ATI electron yields that cannot be explained within the two-step ionization model, where electron rescattering is not included.

Two other experiments are directly related to this work. In a pioneering experiment by Dudovich *et al.*, control over even- and odd-harmonic generation has been demonstrated in $\omega/2\omega$ excitations [47]. In this case, the electron dynamics are governed by an $I_\omega = 10^{14}\,\mathrm{W/cm^2}$ for 800 nm carrier wavelength. Small perturbations in the form of the second harmonic $I_{2\omega} = 5\cdot 10^{-3}\, I_\omega$ break the symmetry of the system and even harmonics are generated. In Fig. 1.7, a HHG spectrum containing even- and odd-harmonics signals alternate out of phase as a function of the phase of the ω-2ω excitation. Thus, the experiment can be viewed as a coherent control experiment in the fashion proposed by Brummer and Shapiro. It is interesting to note that measuring photoelectrons and HHG may be considered as complementary channels to study electron dynamics because the electron trajectories relevant for photoelectrons are the same as those for HHG up to the first return [112].

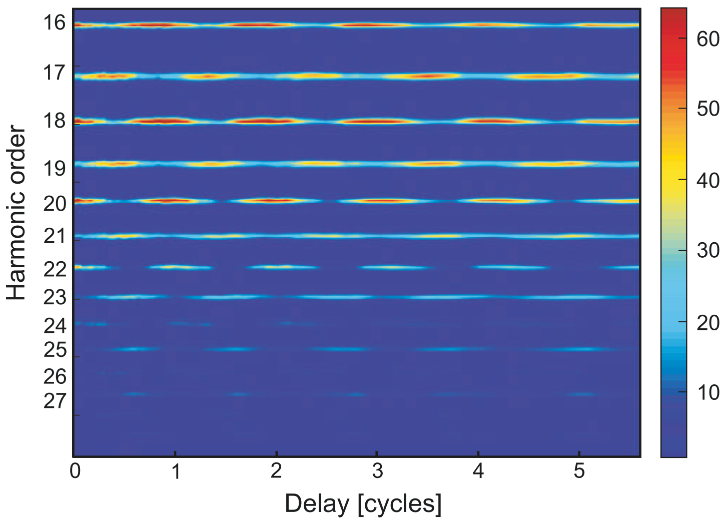

Figure 1.7: HHG spectra recorded as a function of relative time delay between ω/2ω pulses with $I_\omega = 10^{14}\,\mathrm{W/cm^2}$ and $I_{2\omega} = 5 \cdot 10^{-3}\,I_\omega$. Control of the electron recombination results in an out-of-phase signal modulation for even- and odd-harmonics generation. The relative delay controls generation of even- and odd-harmonics. The figure is taken from [47].

The results of an experiment on angle-resolved photoemission from Xe in a ω-2ω field are illustrated in Fig. 1.8. ω-2ω pulses with intensities $I_\omega = 6 \cdot 10^{13}\,\mathrm{W/cm^2}$ and $I_{2\omega} = 2 \cdot 10^{13}\,\mathrm{W/cm^2}$ are utilized to control electron rescattering. The intensity of the 2ω field ($\mathrm{I}_{2\omega} = 0.33 \cdot \mathrm{I}_\omega$) introduces a much stronger perturbation for the system than in the case discussed before. The rescattering part of the photoelectron spectrum exhibits a strong phase-dependent asymmetry and can provide a robust method for determining the relative phase of the ω-2ω field. A detailed analysis of the phase dependencies in the angle-resolved spectrum has so far received little attention.

1.3.2 CEP control

The development of few-cycle laser systems in the mid-IR range enables performance of experiments with pulses consisting of only a few field oscillations [122; 123; 124]. Typically, Ti:sapphire lasers create pulses at a central wavelength of 800 nm, where one period of the electric field oscillation corresponds to 2.7 fs. Thus, the laser pulse with duration 4-5 fs contains only a few oscillations. The most important consequence is that the temporal evolution of the electric field strongly depends on the carrier-envelope phase (CEP), i.e. the phase of the electric field with respect to the envelope. Photoionization is only one example of a process that depends non-linearly on the electric field.

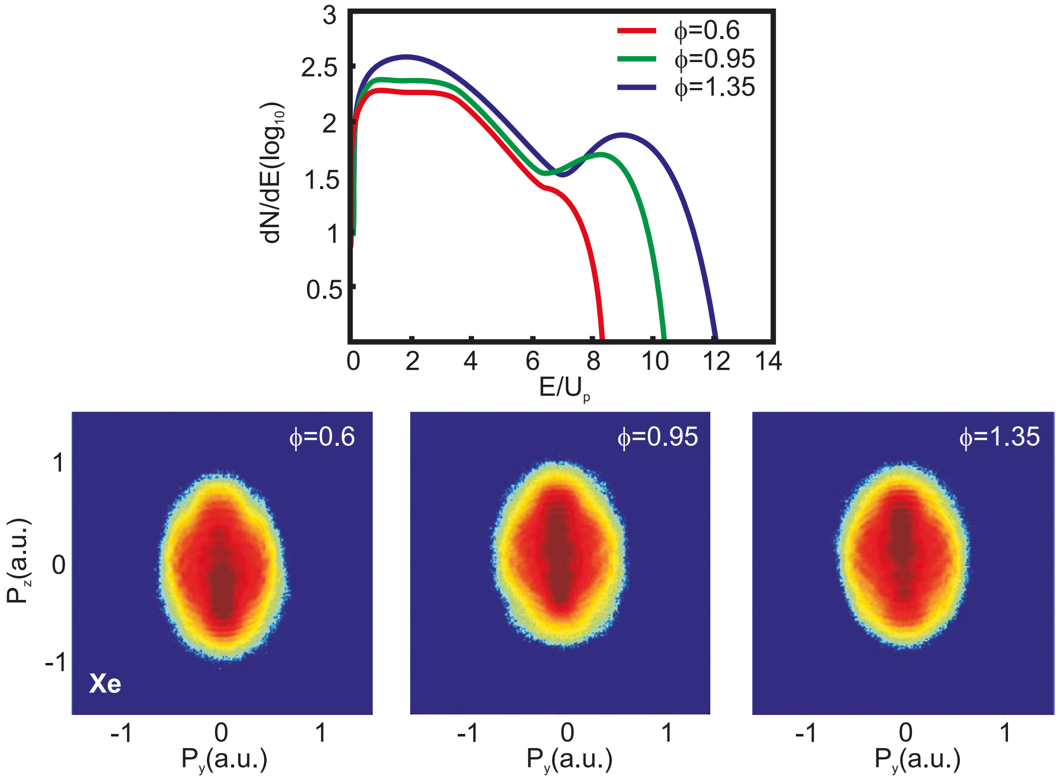

Figure 1.8: Photoelectron spectra (upper panel) integrated over 10° angle with respect to the polarization direction and three different $\omega/2\omega$ phases illustrate the shift of the $10\,U_p$ cut-off. Photoelectron imaging spectra from Xe (lower panel) for $I_\omega = 6 \cdot 10^{13}\,\mathrm{W/cm^2}$ and $I_{2\omega} = 2 \cdot 10^{13}\,\mathrm{W/cm^2}$ recorded for the same phases as in the upper panel [121].

Adjusting the CEP phase enables control of photoemission from an atom target as presented in Fig 1.9. In the experiment, photoelectron spectra from Xe are measured using two detectors (red and black) along the laser-polarization direction (left and right). The CEP phase influences both the high-energy cut-off at 50 eV and the electron yield within the plateau region $(20-40$ eV$)$. Once the CEP stabilization is turned off, no asymmetry is present.

1.4 Typical electron features

Experimental results presented above demonstrates influence of the controlled laser fields on the ionization and electron recollision. In present work, photoelectron channel is systematically studied in fashion resulting from combination of ideas Dudovich and Ray. Investigation of the low-perturbation on the rescattering dynamics are done

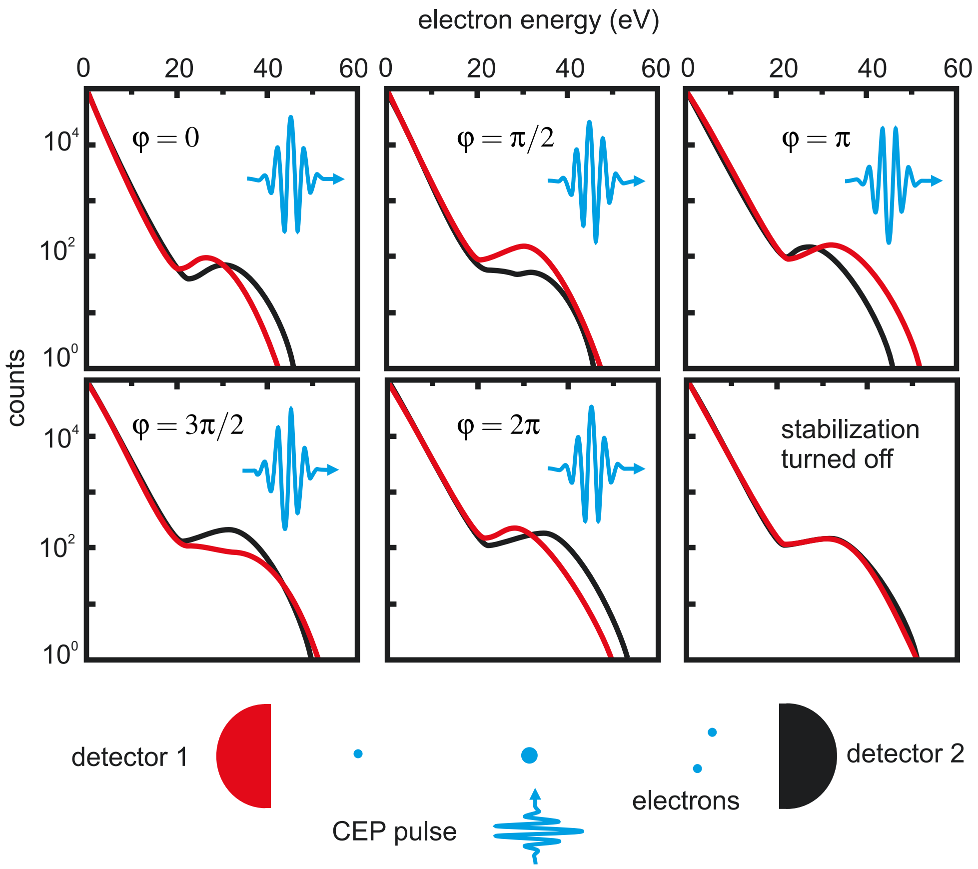

Figure 1.9: Photoelectron spectra recorded for CEP-stabilized laser pulses. Asymmetrical photoemission in left (red) and right (black) along the laser polarization direction is due to the distribution of the electric field of the CEP pulse illustrated in the inset (blue). Spectra show a similar signal distribution as the results obtained with ω-2ω laser pulses. The figure is adapted from [122].

by means of angle-resolved photoelectron spectroscopy with a velocity-map imaging (VMI) system. Momentum-resolved photoelectron spectra result from the projection of 3-D electron wavepackets dynamically interacting with parent ion onto a position-sensitive detector and contains information about recollision dynamics. Thus, typical

---

Figure 1.10 ***(following page)*:** Angle-resolved photoelectron spectrum calculated by solving the time-dependent SchrÃűdinger equation for the Xe atom ionized with a five-cycle laser pulse with peak intensity $I = 5 \cdot 10^{1}3\,\mathrm{W/cm}^{2}$ and a central wavelength of 800 nm (adopted from [125]). Typical features for tunnel ionization and rescattering in a strong laser field are labelled (see text for details).

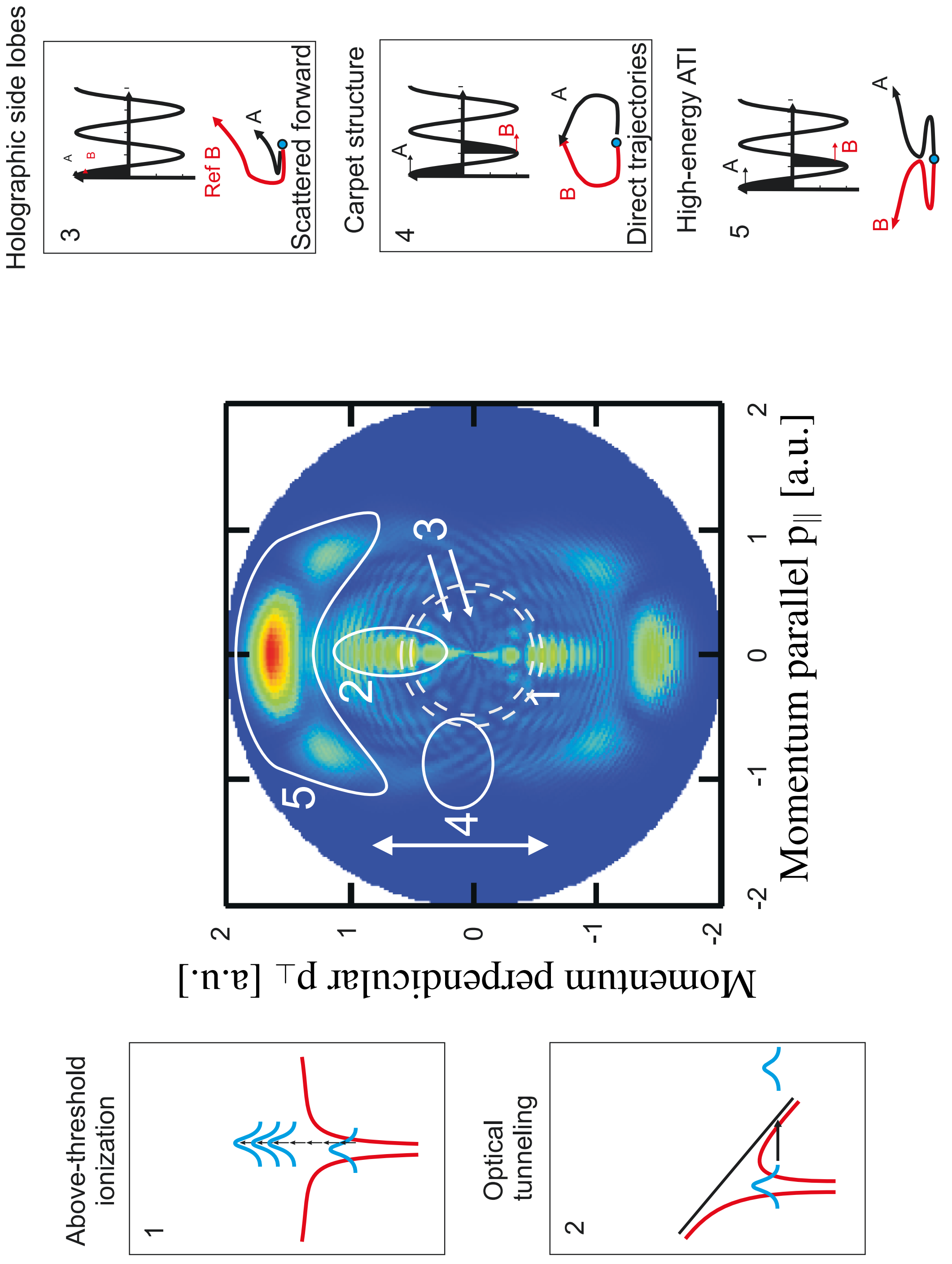
Holographic side lobes
3
A
B
Ref B
A
Scattered forward
Carpet structure
4
A
B
A
B
Direct trajectories
High-energy ATI
5
A
B
A
B
1
2
3
4
5
Momentum parallel $p_\parallel$ [a.u.]
Momentum perpendicular $p_\perp$ [a.u.]
-2
-1
0
1
2
Above-threshold ionization
1
Optical tunneling
2

features relevant to our study are summarized in Fig. 1.10. The following numbering corresponds to the signatures assigned in the figure.

1. Most prominent is the series of ATI rings spaced by the photon energy (here $h\nu = 1.55\,\mathrm{eV}$) [98; 126; 127]. They reflect a constructive interference pattern between wave packets released during different periods of ω [128; 129]. In the multiphoton regime, the ATI structure can be regarded as the absorption of additional photons above the continuum energy [130]. The resulting comb-like patterns originate in this case from the particle-like nature of the photons.

2. Discrete ATI rings are distributed on a continuous "plateau" photoelectron signal resulting from elastic scattering. This is predicted by the "three-step model" of Corkum [77], in addition to two other channels, i.e. HHG [106; 131] and inelastic scattering [132]. It should be noted here that in our experiment only the elastic scattering channel is taken into account. As already shown in the previous section, the photoelectron energy upon rescattering is continuously distributed. Thus, the photoelectrons can end up with any value of energy between 0 and $10U_p$. The tunnelling process is very sensitive to the shape of the barrier [133]. For linearly polarized light, the strongest barrier suppression is in the laser polarization plane. Therefore, the signal enhancement appears along the laser-polarization axis, which reflects the enhanced probability for tunnelling [98].

3. For large angles with respect to the polarization axis, angular patterns with distinct minima and maxima form a carpet-structure [134; 135]. The signal results from interference between the photoelectron wave packets, which for large angles are not significantly disturbed by the Coulomb potential. In contrast, for small angles the carpet structure is not resolved due to the Coulomb field, which strongly affects the electron wave packets propagating at relatively small angles.

4. A low-energy ATI spectrum contains holographic side-lobes located close to the laser polarization axis. They result from the interference between two trajectories ending up with the same final momentum. One of them is strongly affected by the Coulomb potential and therefore accumulating phase, which results in an interference pattern [136]. In other work, the lobes are associated with the number of multiple returns [137].

5. The signal distribution in the high-energy ATI (HATI) shows a target-dependent angular dependency. It has been demonstrated that in the case of ionization with a few-cycle laser pulses, information about the elastic scattering cross-section can be retrieved as predicted by quantitative rescattering theory (QRS) [138; 139]. Morishita et al. have shown that QRS can be applied even for a longer time, e.g. 100 fs pulses to extract differential cross-sections with good agreement.

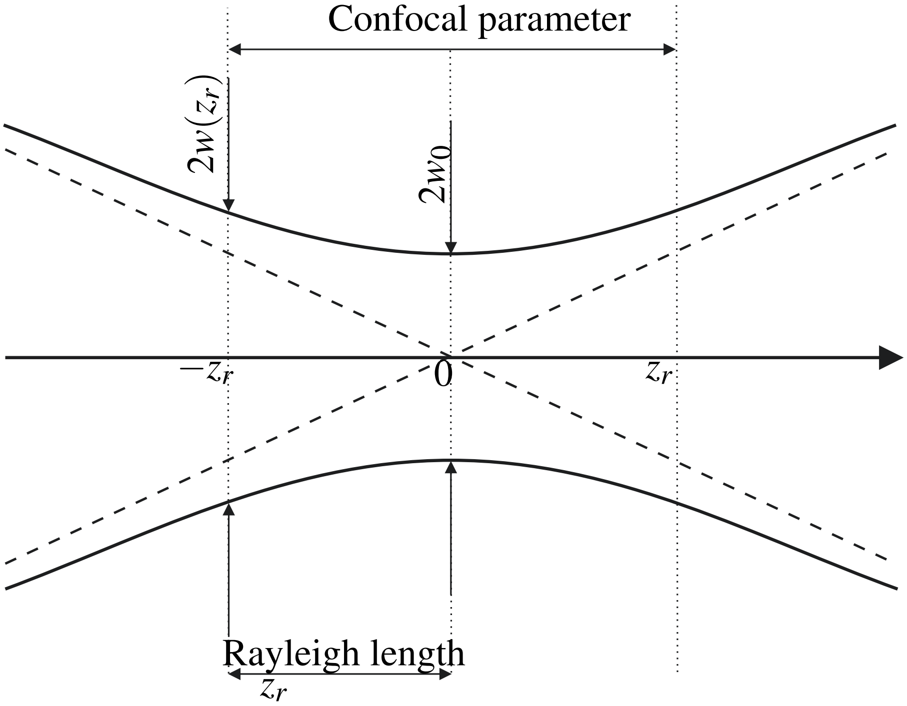

Figure 1.11: Schematic representation of a focused laser beam with Gaussian intensity profile. Beamwaist $2w_0$ and Rayleigh length z_r at which beam expands to $\sqrt{2}w_0$ are labelled. Note that for large distances from focal point beam diameter converge with dotted lines.

Focusing of the Gaussian beam

High laser intensities, which are a prerequisite for tunnelling ionization and successive rescattering, are obtained by focusing the short laser pulses into the interaction point. Assuming a Gaussian radial profile for the laser beam, the intensity in the interaction volume can be expressed by [140]:

$$I(r,z) = \left[\frac{I_0}{1+(\lambda z/\pi w_0^2)^2}\right] exp\left[\frac{-2r^2}{w_0^2(1+(\lambda z/\pi w_0^2)^2)}\right] \tag{1.11}$$

where the beam diameter along the propagation axis is:

$$w(z) = w_0\sqrt{1+\left(\frac{\lambda z}{\pi w_0^2}\right)} \tag{1.12}$$

The Rayleigh range defines the distance at which a focused beam radius expands to $\sqrt{2}w_0$:

$$z_r = \frac{\pi w_0^2}{\lambda} \tag{1.13}$$

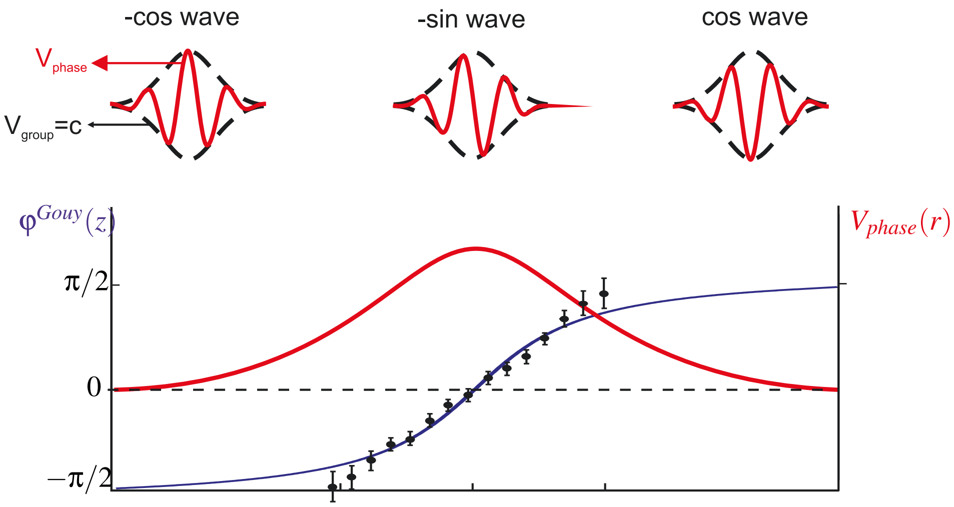

Figure 1.12: The Gouy phase shift of a focused CEP laser beam with radial Gaussian intensity distribution modulates the phase velocity v_{phase}. Note that a wave packet travels with unaffected group velocity $v_{g=c}$. As a result, the CEP phase flips by π as it travels over a distance $2z_r$ (Rayleigh range). Results of Gouy phase measurements for CEP pulses ($\tau_L = 5\,\text{fs}$, f = 25 cm and $z_0 \approx 2\,\text{mm}$) are adopted from [141].

The beam waist describes the minimal radius of the focused beam.

$$2w_0 = \left(\frac{4\lambda}{\pi}\right)\left(\frac{f}{D}\right) \tag{1.14}$$

In the experiment utilizing a VMI spectrometer, the size of the interaction volume strongly influences the resolution. Thus, it is important that the Rayleigh range be minimized. Taking into account the geometrical constraint, i.e. because of the vacuum chamber size, the optimum focusing length for the lens/mirror system amounts to f = 300 mm.

1.5 Gouy phase shift

The Gouy phase shift relates to the phase slip, which is experienced by the light beam as it passes through its focus. The phenomenon was discovered more than 100 years ago by Gouy [142]. It applies for sound [143] as well as for electromagnetic waves [144]. The Gouy phase shift is a geometrical effect that depends on the wave-front geometry, the focusing system and wavelength. A beam with a spherical wave-front experiences

π axial phase shift while a cylindrical wave-front shows only $\pi/2$[145]. The phase slip for the TEM$_{00}$ mode travelling in the $+z$ direction is given by the simple formula [141]:

$$\varphi^{Gouy} = -arctan\left(\frac{z}{z(\lambda)}\right) \tag{1.15}$$

where z refers to the Rayleigh distance, which depends on the wavelength λ. This situation is schematically illustrated in Fig. 5.5. The two-color intense laser pulse (red) travelling from $-\infty$ to $+\infty$ experiences a π phase shift on distance related to $2z_r$ when focused with a spherical mirror. The axial dependency of the shift as a function of the position is plotted as a blue line.

The phase shift has important consequences in the physics of strong laser fields. Focused few-cycle laser pulses experience CEP phase changes because of the Gouy phase shift. This effect has been demonstrated by means of photoelectron spectroscopy [141]. Shivaram has shown that the Gouy phase slip can be measured by means of an IR–XUV pump–probe experiment [146]. Crucial for HHG are the phase-matching conditions governed by the Gouy phase shift and the atomic response [147; 148]. The phase slip can be discriminated by minimizing the laser wave-front, i.e. by sending a focused laser beam through an optical fibre filled with gas [149].

2 Theoretical Methods

This section gives a brief introduction to the theoretical models utilized in this work. To understand the experimental data in terms of classical trajectories, Simple Man‘s Theory (SMT) based on the three-step strong field ionization model [77] has been utilized. Derivation of SMT for a single pulse is adapted from [150]. The SMT model for two-colour fields was developed by Dieter Bauer. The Strong-Field Approximation (SFA) renders any interference between wavepackets emitted during consecutive cycles of the laser pulse. Both models enable the underlying physical mechanism behind two-colour strong field ionization to be understood. The SMT and SFA simulations presented in this work are calculated by codes developed in the group of Dieter Bauer, see e.g. [151]. The time-dependent Schrödinger equation (TDSE) has been implemented by Thomas Fennel and Mathias Arbeiter. Because the SFA and SMT models give intuitive and qualitative pictures of the processes of strong-field ionization and rescattering, we will briefly discuss their basic ideas. Throughout this chapter atomic units are used, if not otherwise stated.

2.1 Simple Man‘s Theory

SMT [78; 79; 80] is a classical approach to describe the electron dynamics in a strong laser field. The process can be divided into three steps [77]. In the first step, the electron tunnels through the Coulomb barrier, which is suppressed by the quasi-static laser field, i.e. the field does not reverse during tunnelling. The tunnelling probability is defined by the Landau rate, which describes the transit through a triangular barrier in the hydrogen atom [152]:

$$w \sim \mid E(t) \mid^{-1} \exp\left(- \frac{2}{3 \mid E(t) \mid} \right) \tag{2.1}$$

A rather strong electric field is needed to turn the Coulomb potential into a tunnelling potential. In the vicinity of the laser pulse peak, the tunnelling amplitude reaches its maximum. In the second step, the electron appears at zero position with zero momentum (in the ion reference frame) and begins to oscillate in the laser field. While being in the continuum, the electron is not affected by the Coulomb field, which greatly simplifies the description. For certain conditions there is a probability that the electron will

re-encounter the vicinity of its parent ion. As a result, it will be dephased from its harmonic motion and rescatter elastically, gaining energy from the laser field (step three) [77].
The electron momentum $p(t)$ and position $r(t)$ at any time instant $t > t_{ion}$ can be calculated from classical equations:

$$\mathbf{p}(t) = -\int_{t_{ion}}^{t} dt' \, \mathbf{E}(t') \tag{2.2}$$

$$\begin{aligned} \mathbf{r}(t) &= -\int_{t_{ion}}^{t} dt' \, \mathbf{A}(t') - \mathbf{A}(t_{ion})(t - t_{ion}) \\ &= \alpha(t) - \alpha(t_{ion}) - \mathbf{A}(t_{ion})(t - t_{ion}) \end{aligned} \tag{2.3}$$

with the excursion defined as:

$$\alpha(t) = \int_{-\infty}^{t} \mathbf{A}(t') \, dt' \tag{2.4}$$

and the vector potential in the length gauge:

$$\mathbf{A}(t) = \int dt' \, \mathbf{E}(t') \tag{2.5}$$

The excursion parameter α defines the spatial position of the electron in the parent ionÂt's reference frame. Without rescattering and assuming that the vector potential vanishes at the beginning T_0 and end of the laser pulse $\mathrm{T_p}$ i.e. $\mathbf{A}(0) = \mathbf{A}(T_p) = 0$, the final momentum and energy are determined by the value of the vector potential at the ionization time t_{ion}, i.e.

$$\mathbf{p}(t_{ion}) = -\int_{t_{ion}}^{T_P} dt' \, \mathbf{E}(t') = -\mathbf{A}(t_{ion}) \tag{2.6}$$

$$\mathcal{E}_{dir,\mathbf{p}}(t_{ion}) = \frac{1}{2}\mathbf{p}^2(t_{resc}) = \frac{1}{2}\mathbf{A}^2(t_{resc}) \leq 2U_p \tag{2.7}$$

with the ponderomotive potential defined as $U_p = \frac{1}{4}\hat{A}^2$. The electron can gain a maximum energy $\frac{1}{2}\hat{A}^2 = 2U_p$ if born at the peak of the vector potential. These electrons are called direct electrons and their maximum kinetic energy is the well-known cut-off law in strong laser physics [153; 154; 155]. One should note that although the ionization rate Eq. 2.1 is determined by the electric field, the electron energies in the continuum depend on the vector potential. If an electron re-encounters an ion, i.e. during the propagation it appears at a distance small compared with the Bohr radius ε:

$$\varepsilon > \mathbf{r}(t_{resc}) = \alpha(t_{resc}) - \alpha(t_{ion}) - \mathbf{A}(t_{ion})\tau \tag{2.8}$$

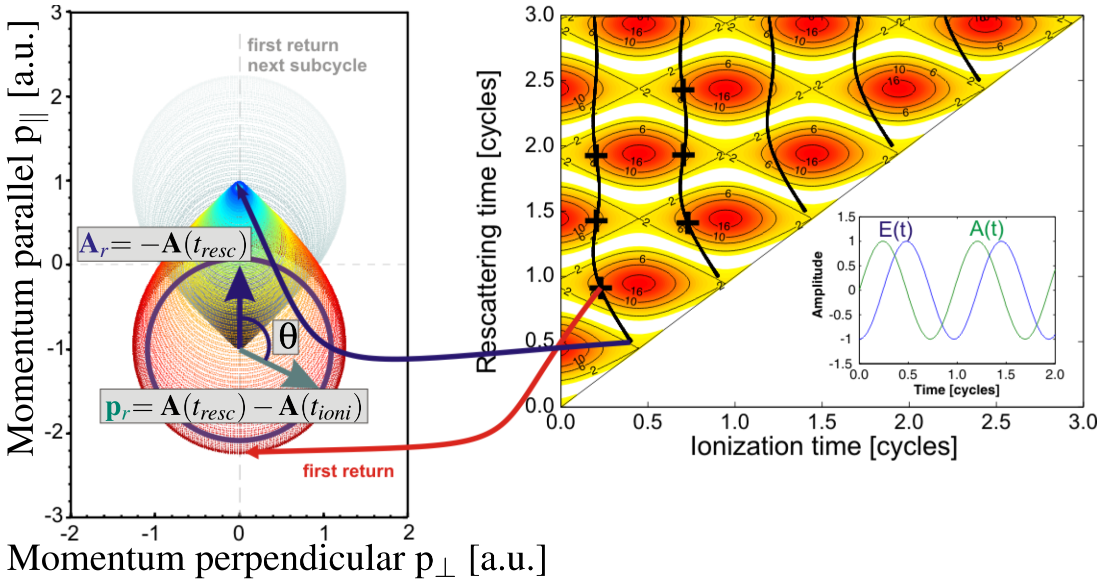

Figure 2.1: SMT-based construction of a momentum-resolved photoelectron spectrum for trajectories scattering at first return. The series of rings represent rescattered electron‘s final momenta in 2-D Fourier space in the laser polarization axis plane. They form two overlapping club-like structures, each created during a sub-cycle of the laser pulse. Black crosses indicates local maxima in the final energy. Black lines indicate possible pairs of ionization (t_{ioni}) and rescattering times (t_{resc}) that are solutions of Eq. 2.8. They enable analytical calculation of the ring centre co-ordinate $(A(t_{resc}))$ and the rescattering ring radius $(A(t_{resc}) - A(t_{ion}))$.The photoelectron signal on the SMT ring is isotropically distributed because no preferential scattering direction is present in the model. The ring colour indicates the electric field amplitude at the ionization time and the high momentum limit corresponds to the $10U_p$ cut-off.Electrons that do not rescatter gain a maximum energy of $2U_p$ and lead to the tip on the opposite side of the imaging spectrum. Calculations were performed with SMT code written by D. Bauer.

it will be dephased from its harmonic motion and gain energy from the laser field [77]. Solutions of Eq. 2.8 are indicated as black points in in Fig. 2.1 (right). In general, the lower ε is the less solution Eq. 2.8 will have.

Immediately after rescattering, the momentum can be written as the difference in the vector potential at the ionization and rescattering times:

$$\mathbf{p}(t_{resc}) = -\int_{t_{ion}}^{t_{resc}} dt' \, \mathbf{E}(t') = [\mathbf{A}(t_{resc}) - \mathbf{A}(t_{ion})] \tag{2.9}$$

After rescattering ($t > t_{resc}$) the electron leaves the vicinity of the atom gaining momen-

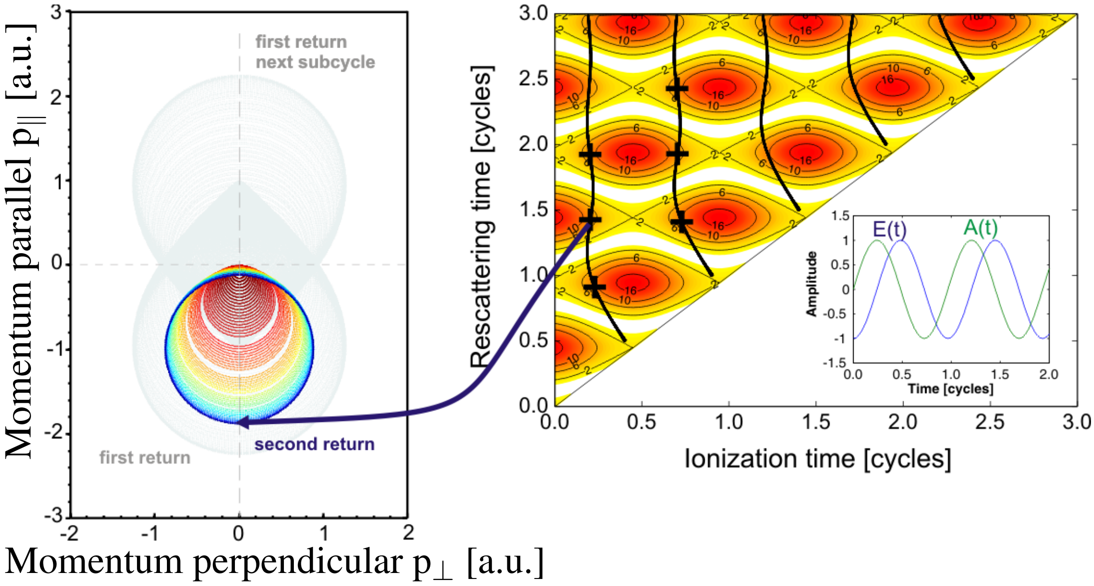

Figure 2.2: The same as in Fig. 2.1 but for second return. Two groups of rings are located on both sides of the SMT momentum spectrum. They are created during one sub-cycle of the laser pulse. Ring colours encode the electric field at the rescattering times. Calculations were performed with SMT code written by D. Bauer.

tum given by:

$$\mathbf{p}(t > t_{resc}) = -\int_{t_{resc}}^{T_P} dt' \mathbf{E}(t') = -\mathbf{A}(t_{resc}) \tag{2.10}$$

Thus, the final energy will be given by the sum of both contributions:

$$\mathcal{E}_{resc,\mathbf{p}}(t_{resc}, t_{ion}) = \frac{1}{2}[\mathbf{A}(t_{ion}) - 2\mathbf{A}(t_{resc})]^2 \leq 10U_p \tag{2.11}$$

Solutions of the above equation are represented as a contour map in Fig. 2.1 (right). For each ionization and rescattering time (t_{ion} and t_{resc} respectively) the final energy is encoded in the colour scale. Based on this approach, a momentum-resolved photoelectron spectrum can be calculated. In SMT, it is assumed that electrons rescatter isotropically and create ring structures in the Fourier momentum space that are parametrized by Eq. 2.9 and 2.10, see Fig 2.1. The ring centre in momentum space is defined by the drift momentum gained by the electron after rescattering (2.10). Correspondingly, the ring radius is defined by the momentum gained in the rescattering process, see (2.9). Thus, the final electron momentum upon rescattering and when the laser pulse is off can be written as:

$$\begin{pmatrix} \overline{p}_z \\ \overline{p}_x \end{pmatrix} = \begin{pmatrix} -a(\tau_2) \\ 0 \end{pmatrix} + [a(\tau_2) - a(\tau_1)] \begin{pmatrix} \cos\theta \\ \sin\theta \end{pmatrix} \tag{2.12}$$

where τ_1 and τ_2 denote the ionization and rescattering times, respectively, and $a = A/A_0$ is the vector potential. The momentum spectrum is calculated for each ionization and rescattering time if the conditions specified in Eq. 2.8 are fulfilled. The corresponding solutions are depicted as black vertical curves in Fig.2.1 which couples specific ionization and rescattering times. In analogy to HHG , one can introduce "long" and "short" trajectories, which are defined by Eq. 2.3. Electrons following "short trajectories" (blue arrow) are born closer to the electric field peak but also rescatter after a short propagation time, gaining rather low energy. In contrast, "the long trajectories" (red arrows) are born well before the laser peak and rescatter at later times and gain maximal energy $10\,U_p$. Rescattering rings for each trajectory are plotted in the momentum spectrum with colour encoding rescattering probability. In SMT, the photoelectron spectrum from one sub-cycle resembles a club-like structure with low-energy electrons located at the opposite side of the momentum spectrum compared with the fast electrons. Because the field changes its sign in the second half of the cycle, the same structure is created but now on the opposite side of the momentum spectrum (here a grey club). For multicycle pulses, such a scenario repeats periodically and a spectrum is formed by combining contributions from all cycles. In the model, only two or three field oscillation periods are considered as important. In the case of short laser pulses with a Gaussian envelope, the electric field strength varies between cycles. Thus, the signal yield and photoelectron momentum distribution both vary from cycle to cycle. To simplify the situation, we introduce a flat-top-pulse where the electric field peak amplitude does not vary between cycles. It is a good approximation for the long pulses used in this work ($\tau = 120\,fs$) where dominating signal contributions originatefrom many successive cycles around the laser peak maximum with slightly different amplitudes. For such an electric field, the electron can follow many oscillations before it finally rescatters during the second, third or even higher-order return. Such a situation and a corresponding momentum spectrum for the second return are depicted in Fig. 2.2. Here, the electrons tunnel in a time interval 0.0-0.25 cycles (light green area in inset) and rescatter after a field period of 2π. Depending on the sign of the vector potential at the time of rescattering, SMT rings are created on both sides of the momentum spectrum. Note that the maximum energy gained during the second and higher-order returns is slightly smaller than the maximum at the first return ($10\,U_p$), see black crosses in Fig. 2.1 and Fig. 2.2.
Electrons that propagate longer will rescatter with lower probability because of the intrinsic wavepacket dispersion. To account for it, a rescattering probability can conveniently be described by [150]:

$$W_r(t_{resc} - t_{ion}) = (t_{resc} - t_{ion})^{-s} \tag{2.13}$$

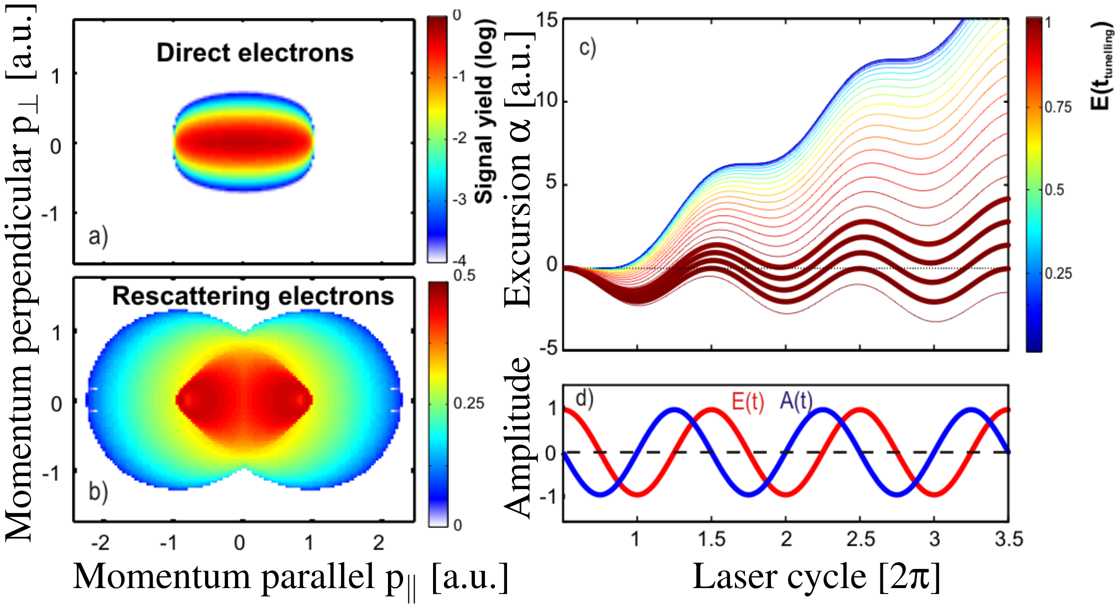

Figure 2.3: SMT spectra calculated for direct (a) and rescattered (b) electrons. Direct electrons appear in the SMT with ionization probability given by the Landau rate in Eq. 2.1. They result from electrons that do not rescatter (blue trajectories in c). For rescattered electrons, the wavepacket spreading probability given by Eq. 2.13 is applied. Only trajectories released within a narrow time window can rescatter multiple times (bold). Note the difference in signal yield (log scale). Calculations were performed with SMT code written by D. Bauer.

Here, the exponent factor (s) accounts for the dispersion rate [79**?**]. Such rescattering does not introduce any angular, momentum or target dependencies. Typically $s = 3/2$ is chosen to mimic the effect of the Coulomb focusing [156]. We will show later in the discussion part that the dispersion factor plays an important role in suppressing higher-order rescattering.

A typical SMT spectrum calculated for direct (a) and rescattered (b) electrons is shown in Fig. 2.3. Upon tunnelling, the electrons are assumed to propagate along the laser polarization axis. Spatial dependencies result from the assumption that the scattering process is isotropic. Direct electrons, i.e. electrons (blue lines in c) that do not rescatter are weighted by:

$$W_i^{(direct)}(\tau_1) = W_i(\tau_1)\exp(-\beta\overline{p}_x^2/\mid \mathbf{e}(\tau_1)\mid) \tag{2.14}$$

with $\beta = 15$. This accounts for the reasonable lateral spread of the direct electron-electron momentum distribution. All rescattering trajectories (red in c) are weighted by $W = W_i W_r$ where W_i denotes the ionization probability (Eq. 2.1) and W_r the rescattering probability, here given by Eq. 2.13. The exponent factor s = 3/2 is chosen to mimic the effect of a Gaussian wavepacket spreading influenced by Coulomb focusing [150; 156**?**].

SMT for two-color fields

We derive an SMT model for two-colour ω-2ω laser pulses by considering the electric field in the dipole approximation:

$$\mathbf{E}(t) = E_0[\cos\omega t + 2\cdot\xi\cos(2\omega t + \phi)] \tag{2.15}$$

and the corresponding vector potential

$$\mathbf{A}(t) = A_0[\sin\omega t + \xi\sin(2\omega t + \phi)] \tag{2.16}$$

Both are related by Eq. 2.5. Here 2ω is the second harmonic, ϕ denotes the relative phase and ξ is the ratio of the electric fields $E(2\omega)/E(\omega)$. The factor ξ is tuned to introduce a controlled perturbation to the fundamental beam.
The phase-dependent electric field of ω-2ω (Eq. 2.15)modulates the tunnelling probability (Eq. 2.1). As illustrated in Fig. 2.5 the electric field (red) and the Landau tunnelling rate (green) exhibit strong dependencies on both the relative phase (φ) and intensity ratio (ξ). For relatively small perturbations (a) $\xi < 0.2$ the tunnelling rate peaks twice per field cycle independently of the relative phase. The tunnelling probability is symmetrical for $\varphi = \pi/2$ and $\varphi = 3\pi/2$, although the tunnelling times slightly change. Asymmetry in the ionization probability builds up and reaches a maximum when $\varphi = \pi$ and $\varphi = 2\pi$. Increasing 2ω intensity up to $\xi = 0.5$ (b) significantly perturbs the electric field. The most profound consequence is an additional ionization time, which can be resolved for $\varphi = \pi$ and $\varphi = 2\pi$. Further increasing 2ω intensity $\xi = 1$ results in four

---

Figure 2.4 ***(following page)*:** Final energy landscape (Eq. 2.11) and rescattering times (solutions of Eq. 2.8) for two-color laser pulses and calculated for weak perturbation $\xi = 0.1$ ($I_{2\omega}/I_{\omega} = 1\,\%$) (left) and strong perturbation $\xi = 0.5$ ($I_{2\omega}/I_{\omega} = 25\,\%$) (right). Black lines indicate possible pairs of ionization (t_{ioni}) and rescattering times (t_{resc}) that are solutions of Eq. 2.8. Black crosses indicates local maxima in the final energy. Pronounced modification of $\mathcal{E}_{resc}$ and ionization and rescattering times can be resolved for strong perturbations. Experimental results presented in this work are recorded for weak perturbations where the final electron energy changes only slightly with the relative phase ϕ. Calculation are performed using SMT code written by D. Bauer.

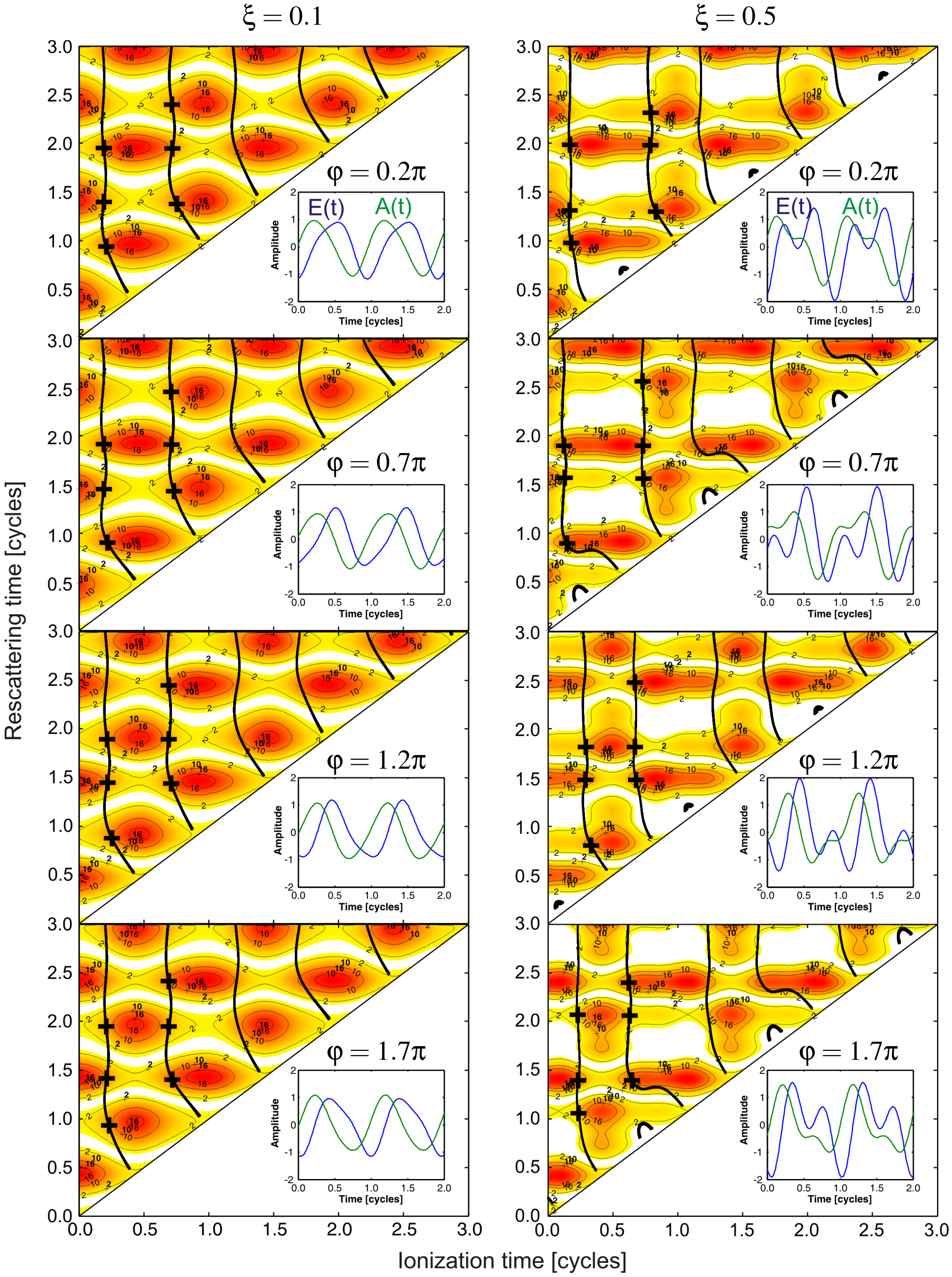
ξ = 0.1
ξ = 0.5
φ = 0.2π
φ = 0.7π
φ = 1.2π
φ = 1.7π
E(t)
A(t)
Amplitude
Time [cycles]
Rescattering time [cycles]
Ionization time [cycles]
0.0
0.5
1.0
1.5
2.0
2.5
3.0
2
10
16

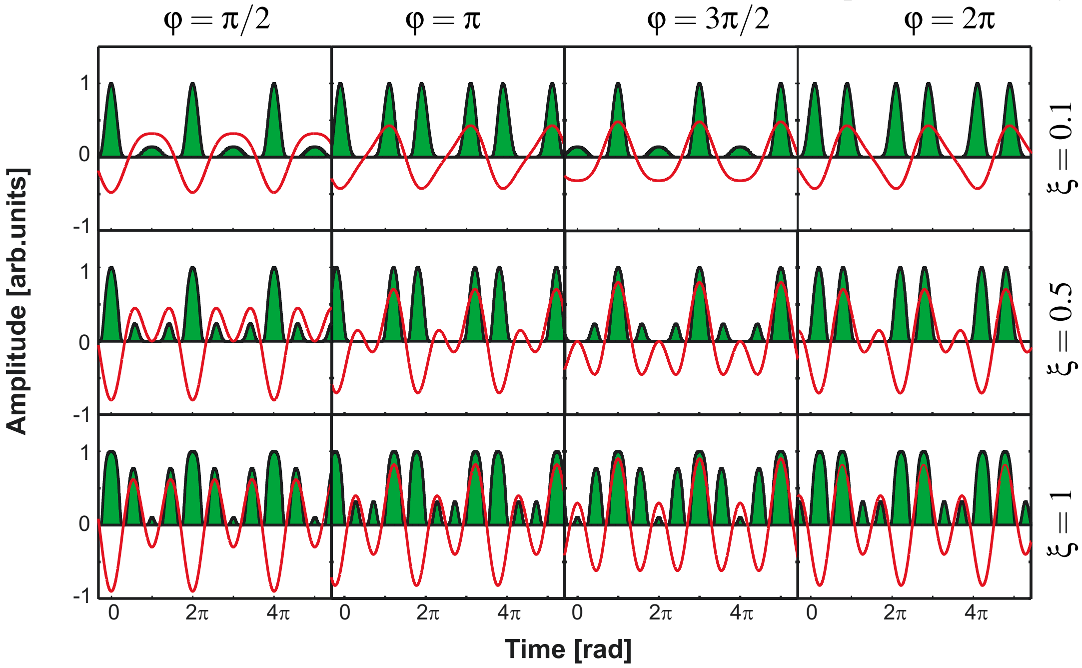

Figure 2.5: Electric field (red) and tunnelling probability given by Eq. 2.1 (green) depend on the relative phase and intensity ratio $\xi = 0.1$ (top) $\xi = 0.5$ (middle), $\xi = 1$ (bottom). Ionization process is weakly perturbed for $\xi = 0.1$ that results in relative-phase dependent ionization time and asymmetrical tunneling probability for $\varphi = \pi/2$ and $\varphi = 3\pi/2$. Strong perturbed electric field ($\xi > 0.2$) generates additional ionization times.

ionization maxima per cycle.

Fig. 2.4 shows the final electron energy (Eq. 2.11) and relation between rescattering and ionization times labelled by black lines (Eq. 2.8).Calculations are performed for two intensity ratios, $\xi = 0.1$ (left) and $\xi = 0.5$ (right) and for different phases ϕ. For $\xi < 0.1$ (left) blue light introduces a weak perturbation to the electron trajectories and the final energy landscape is only slightly perturbed. The electric field and the vector potential vary slightly. A strong perturbation can readily be resolved for $\xi > 0.5$ (right). The final energy map shows a strong dependence on the relative phase ϕ and relations between ionization and rescattering times are strongly perturbed. Interestingly, for $\phi = \pi$ electrons ionized at $t_{ion} \approx 0.2 - 0.4$ recollide at the same time $t_{resc} \approx 0.8$. Physically, it means that many electrons will rescatter at the same time leading to a complicated interference pattern and possibly to an enhanced ionization cross-section and HHG, as reported in [157].

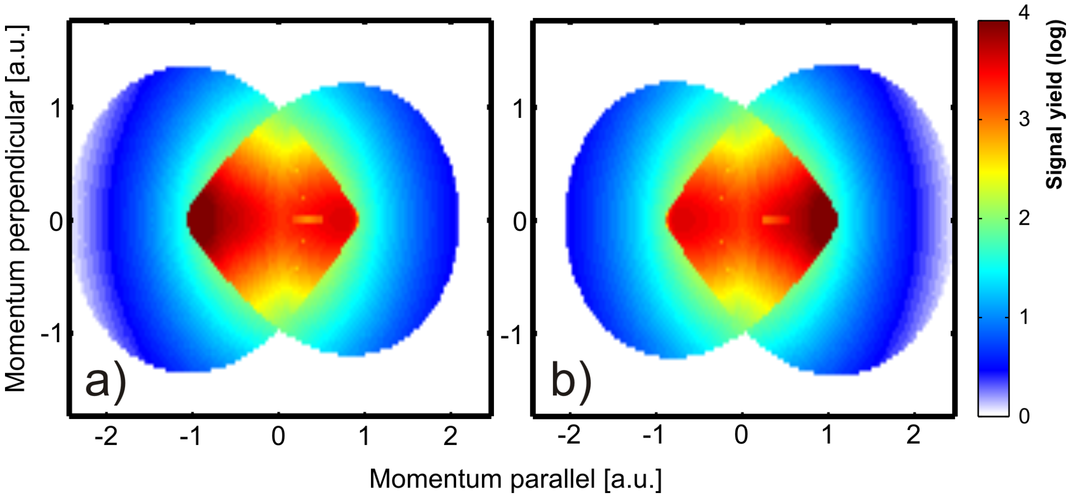

Figure 2.6: SMT-based calculation of momentum-resolved photoelectron spectra for $\varphi = \pi/2$ (a) and $\varphi = 3\pi/2$ (b). $10U_p$ ridge and $2U_p$ tip (red) exhibit strong relative-phase dependencies. Note that because of the classical description where the electron is considered as a particle, no interference effects are present. Spectra were calculated with code developed by Dieter Bauer.

2.2 Refined rescattering model

Now we extend the SMT by including angular dependence in the scattering cross-section. Because the returning electron energy is not relativistic ($E_{max} = 3.17U_p$) and during elastic scattering its energy does not change the scattering process, the hydrogen atom can be described by Rutherford‘s formula. The Rutherford scattering is included in the rescattering probability by introducing a differential scattering cross-section (DSC):

$$W_r(\tau_2 - \tau_1)\sigma(q,\theta) \tag{2.17}$$

In the first Born approximation it has the form [158]:

$$\sigma(q,\theta) = \frac{(2Z)^2}{[\mu^2 + 4q^2\sin^2(\theta/2)]^2}, \qquad q = a(\tau_2) - a(\tau_1) \tag{2.18}$$

for a screened potential in the form of the Yukawa potential $V(r) = -Z\exp(-\mu r)/r$. Here, θ denotes scattering angle, μ is the screening parameter, q indicates momentum and Z is charge. It is known that such a scattering cross-section can be derived from the Lippmann–Schwinger equation using the first Born approximation [158]. Fig. 2.7 illustrates angular DSC dependence on electron impact momentum for $\mu = 0.5$ and $Z = -17$. In general, DSC favours electrons that scatter at small angles, and with lower momentum. Such cross-section introduces angular dependencies to photoelectron spectra. Because the Coulomb potential acts on an infinite range, the scattering amplitude

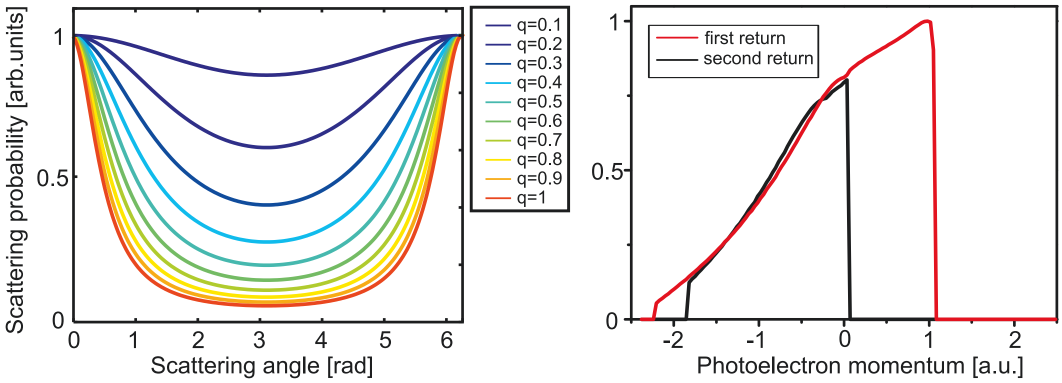

Figure 2.7: Left: DSC (including wavepacket dispersion) as a function of scattering angle for various momenta q [a.u.] and $\mu = 0.5$, $Z = -17$ shows that electrons with low momenta scatter with higher probability at smaller angles. Right: DSC for first and second return shows that second return trajectories scatters with higher probability for low momenta ($-1.2 < p < 0.5$) and dominates SMT spectra. Calculation are performed using SMT code written by D. Bauer.

does not converge. Thus, the Yukawa potential with screening parameter μ has to be employed to overcome convergence problems. In the refined model we use the effective charge $Z = -17$ to mimic the Ar atom and the screening parameter $\mu = 0.5$.The DSC is a function of the scattering angle and momentum. It shows $\omega/2\omega$ dependence because the vector potential at the ionization and rescattering times ($a(\tau_1)$ and $a(\tau_2)$, respectively) depend on ϕ. Thus, it modifies the phase dependencies in the SMT model. In Fig. 2.6 SMT spectra calculated for $\xi = 0.1$ and two values of relative phase ϕ are shown. Asymmetrical photoemission can be resolved as an enhanced signal in the $2\,\mathrm{U_p}$ region (dark red) and changes in the high momentum cut-off.

2.3 Beyond SMT theory

The time-dependent Schrödinger equation (TDSE) is the most accurate theoretical formalism describing non-relativistic electron dynamics in a strong laser field. Computational requirements limit its capability, however, mostly to a single active-electron problem. In Fig. 2.8 PP and RPC spectra are calculated for Ar in 1s, 2p ground state from numerical solution of TDSE. Binding potential is defined in cylindrical co-ordinates and consists of both Coulomb and Yukawa potential:

$$V(r) = -1/r - (Z_{eff}/r \cdot \exp -\mu \cdot r) \tag{2.19}$$

where Z_{eff} is effective charge, μ is screening parameter and r is radial coordinate. The experimental ionization potential has been imposed by tuning the screening parameter and the effective charge ($Z_{eff} = -12$ and $Z_{eff} = -17$ for $3p$ and $1s$ respectively). Although TDSE calculations reproduce typical features observed in the experiment with

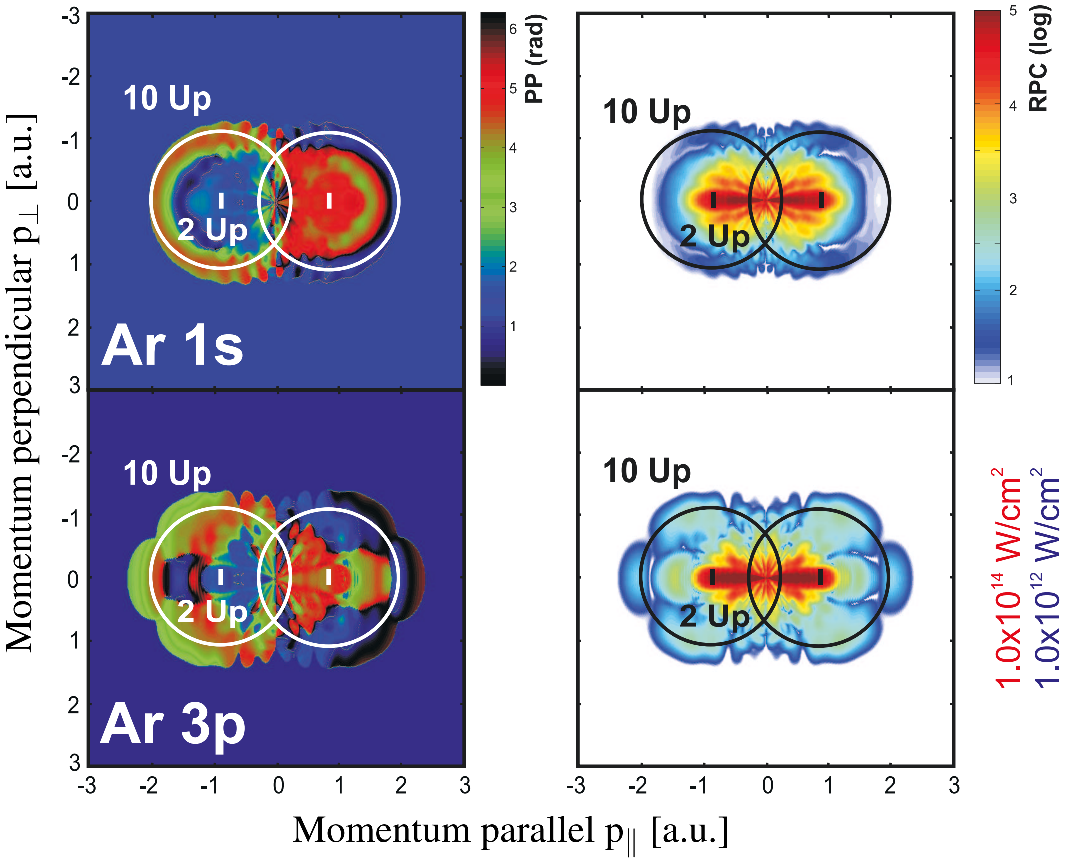

Figure 2.8: TDSE calculations for a single-electron system with ionization potential that mimics the Ar atom and with the electron in the 1s and 2p configurations. The clear influence of ground state on PP and RPC spectra can be resolved. Laser intensity is indicated in the figure. Calculations performed by M. Arbeiter.

high accuracy (e.g. holographic pattern, ATI, angular distribution, etc.) it suffers because of the lack of physical insight, which remains hidden behind the theoretical formalism.

This problem is partially overcome in semi-analytical SFA , also called Keldysh–Faisal –Reiss theory [159; 160; 161]. SFA describes electron dynamics in a strong laser field in terms of interfering waves. The key point is to neglect the Coulomb interaction, which greatly simplifies the problem. Thus, a picture of interaction with a strong laser field is realized as follows:

- In the first step, the electron is considered to be bound in the ground state. At this step, the atomic potential is dominant and the oscillatory laser field is neglected. The electron follows a transition into the continuum by applying the

Gordon–Volkov propagator.

- Starting from now, the electron is not affected by the ionic Coulomb potential and the electron is described as a plane wavepacket driven by the laser electric field and creating a rich interference pattern.

- The contributions from bound states to the evolution of the system are neglected except for the ground state.

The main reason for discrepancies between SFA and TSDE is lack of Coulomb interaction due to neglecting atomic potential in Hamiltonian and replacing final state by Gordon–Volkov state which describes free electron in oscillatory field. The main reason for discrepancies between SFA and TDSE is the lack of a Coulomb interaction because of neglecting the atomic potential in the Hamiltonian and replacing the final state by a Gordon–Volkov state, which describes a free electron in an oscillatory field. There are a few points at which the given approximations may lead to errors. In general, problems appear from lack of interaction with short- and long-range Coulomb potentials. The tunnelling process is very sensitive to the shape of the barrier and the binding potential. Thus, the ionization probability will be hardly affected by the binding potential. It was shown that including corrections for the short-range Coulomb potential can explain features observed in experiments such as the fan-like structures in the momentum distribution at low energies and low-energy structure [112]. Propagation in the continuum is also affected by the Coulomb potential because electrons scatter from it. However, even without further Coulomb corrections, SFA can reproduce fairly well the pronounced interference structure. To include short-range Coulomb transition, the Gordon–Volkov final state is replaced by a Coulomb–Volkov (CV) state and a distortion potential is included in the evolutionary operator [162].

3 Experimental Techniques

This chapter contains a brief description of the experimental set-up utilized for studying phase-dependent photoemission. Photoelectron momentum spectra were recorded by means of a velocity map imaging (VMI) technique (VMI) [163; 164; 165]. The system generating sculpted ω-2ω laser pulses is similar to one utilized elsewhere [47; 61]. To analyse a relative phase-dependent momentum spectrum, we introduce two-colour 'phase-of-the-phase' spectroscopy ($\mathcal{P}o\mathcal{P}$). Key point of this method is the extraction of periodic (phase-dependent) changes in a momentum-resolved photoelectron spectrum by means of Fourier analysis. $\mathcal{P}o\mathcal{P}$ introduces two quantities that quantify for each projected momentum a relative-phase contract (RPC) and a phase-of-the-phase (PP) describing how much and with what phase lag, respectively, the yield changes with respect to the relative phase.

3.1 Laser system and two-color set-up

Short and intense laser pulses are delivered by a commercial Ti:sapphire laser system Model Solstice Spectra-Physics. The laser system generates 130 fs pulses at a central wavelength of 793 nm with maximum power of 3 mJ at 1 kHz repetition rate. A neutral density filter is used to control the laser power in the experiment. The generation of two-colour ω-2ω pulses requires a non-linear crystal with second-order susceptibility $\chi^{(2)}$. A beta barium borate $\beta - \mathrm{BaB_2O_4}$ (BBO) crystal is one of the most versatile materials used in second-harmonic generation (SHG) with ultra-short lasers [166; 167]. We generated a p-polarized second harmonic (SH) at 397 nm with an I-Type BBO crystal of 200 μm thickness using the fundamental harmonic (FH) of the laser field (s-polarization) after passing through a BBO crystal, generating the SH (p-polarization). The residual FH is still present in the beam. Because of intrinsic BBO crystal dispersion, SH and FH are offset in time so that the fundamental beam leads. The time lag is compensated by a calcite crystal. The FH is sent along the ordinary (slow) and SH along the extraordinary (fast) axis. A quartz half-wave plate ($\lambda/2$) rotates the polarization axis of FH by 90° and SH by 180°. As a result, we obtain a coherent superposition of FH and SH with the polarization vector oscillating in the same plane and overlapped in time. The SHG conversion efficiency is optimized by tilting the BBO crystal. For a detailed view of the set-up see Fig. 3.1.

Precise control of the time overlap between FH and SH is achieved by two fused-silica

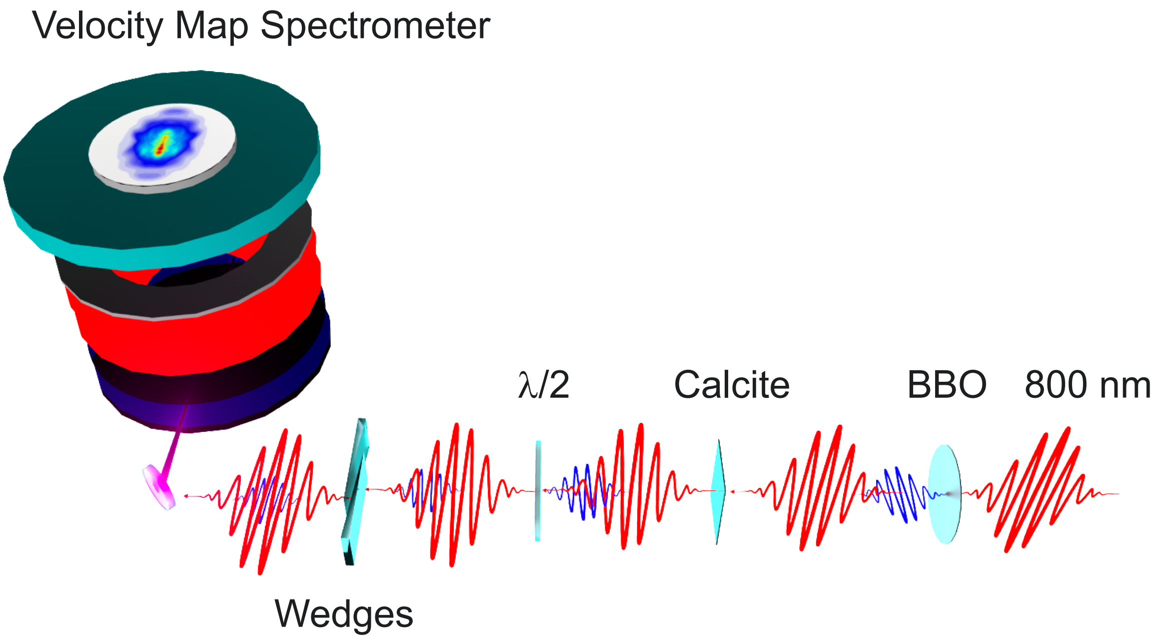

Figure 3.1: Experimental set-up utilized to study momentum-resolved photoemission in a strong ω-2ω field. Coherent superposition of carrier 793 nm beam with its SH generates an asymmetrical electric field. The relative phase of the ω-2ω field is controlled with sub-fs precision. A high-energy velocity map imaging spectrometer (HEVMI) [168] is employed to study photoemission with angular resolution. Laser pulses are focused using a spherical focusing mirror (f = 300 nm) located on the back of the HEVMI spectrometer.

wedges mounted on a piezo-motor-driven stage (SmartAct) operating with 1 nm resolution. We ensure that the laser propagates normal to the wedge surface by monitoring a back reflection. A zero point has been found in analogy to a single-slit diffraction. Typically, scanning a relative phase interval of about 3π, 200 motor steps each of 1μm are needed. The present configuration enables experiments with various polarization configurations, e.g. perpendicular oriented lasers or elliptical, to be performed.

We carefully checked how tilting and rotating the BBO influences the polarization of the SH. The result of the procedure described below is shown in Fig. 3.2. Polarization at 400 nm is characterized by measuring the transmission through a high-contrast wire grid. The first step is to measure the SH polarization for the optimized phase-matching condition (maximized efficiency). By means of a harmonic separator, which reflects SH and transmits FH radiation, the FH and SH beams are separated. In addition, a band pass filter ($T_{800nm} = 0.006\,\%$) is used to attenuate the residual FH. To test the performance of the set-up, a wire-grid polarizer is rotated in steps of 10°. At each position, the average power transmitted through the grid is determined using a thermocouple ($P_{min} = 1$nJ).

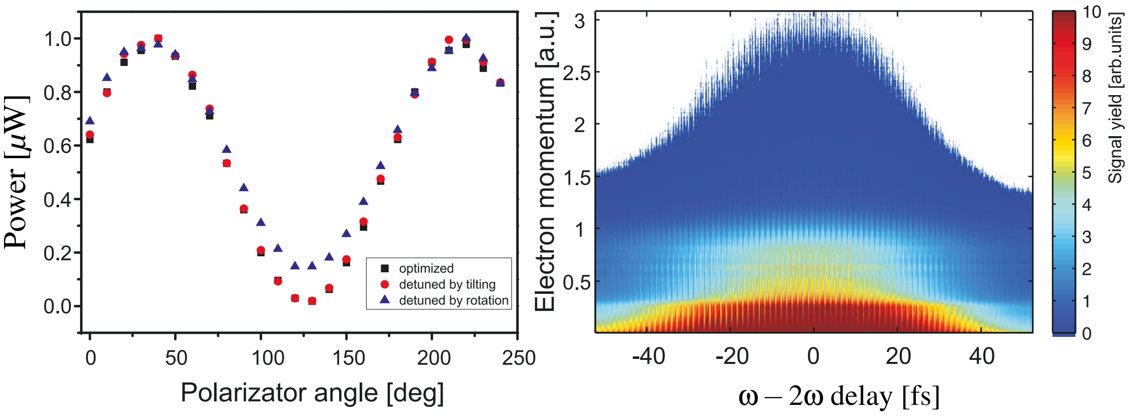

Figure 3.2: Influence of tilting and rotating the BBO crystal on the SH polarization (left). Tilting (circles) does not influence the polarization of an optimized beam (squares). When rotating the crystal, the polarization change is clearly seen (triangles). Right: cross-correlation scan performed by moving the wedges over a large distance. The resulting photoelectron yield is measured and plotted as a function of motor position, which corresponds to the relative phase.

Subsequently, the efficiency of SHG is reduced by a factor of two by (i) tilting and (ii) rotating the BBO crystal. The results in Fig. 3.2 are normalized to the maximum signal. The modulation contrast clearly shows that tilting does not affect polarization at the optimized efficiency. When the crystal is rotated, the modulation contrast is weaker because of the additional vertical SH component present. With these findings, it is clear for the experiment that controlling SH intensity by means of crystal tilting does not influence the polarization of the SH.

3.2 Characterization of the HEVMI spectrometer

Photoelectron momentum-resolved spectra were recorded using a home-built VMI [168]. Its technical realization with extended energy detection range is shown schematically in Fig. 3.3 (left). Five cylindrical electrostatic lenses generate a non-uniform field that guides the electrons through the spectrometer preserving information about the 3-D photoelectron momentum. Repeller and extractor electrodes have negative polarity with a potential ratio of $U_{rep}/U_{extr} = 1.6$. An additional pair of equipotential positive polarity electrostatic lenses are kept at a ratio of $U_{rep}/U_{lens} = -1.6$. An effusive gas injector (500 μm diameter pinhole) is integrated at the centre of the repeller electrode. For detection, a position-sensitive detector is used consisting of multichannel plates (MCP) and a phosphor screen (P43). We use two types of detectors: (i) an 80 mm diameter self-constructed system consisting of a single MCP (RoentDek) with phosphor screen (Proxivision), and (ii) a 40 mm double MCP stack (Chevron) with P43 phosphor screen (Photek). Sufficient amplification of the photoelectron signal is achieved by applying a

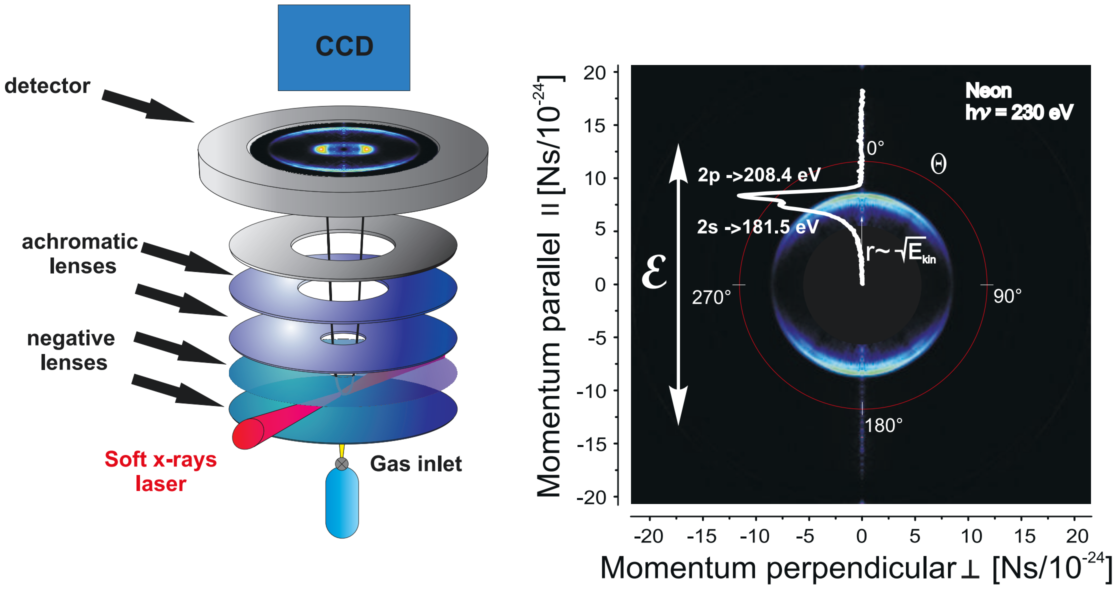

Figure 3.3: HEVMI spectrometer utilized to study bichromatic emission from atoms and molecules. The five-electrode set-up is capable of mapping photoelectrons with angular distribution and energy up to 100 eV/kV (applied kV on the repeller electrode). Right: imaging spectrum from Ne ionized with 230 eV photons. The two rings correspond to ionization of the 2p and 2s levels.

voltage of 960 V (single MCP) and 1600–1900 V (double stack) at the bottom side of the MCP. The front side of the phosphor screen is supplied with 6.5 kV (80 mm detector) and 4 kV (40 mm detector), respectively. To suppress background contributions, as for example signals from detector noise or secondary electrons, the MCP voltage has been gated using a high-voltage switch (Behlke, HTS-30) with a gate width of 70–150 ns. Alternatively, the semiconductor-based Medipix2 [169] or a delay line detector [170] can be utilized. The photoelectron images resulting from ionization are recorded by a 12-bit CCD camera (Hamamatsu, ORCA-ER). Taking into account cylindrical symmetry of the emitted electrons with respect to the polarization axis, complete 3-D information about the photoelectron emission direction can be retrieved using e.g. the Abel inversion algorithm [171].

The VMI spectrometer can operate in two modes: velocity map imaging and spatial imaging as illustrated in Fig. 3.4. In the velocity imaging mode (Fig. 3.4 left) all electrons emitted with the same momentum are projected onto the same ring. Thus information about angular distribution is preserved and can be retrieved from signal angular distribution. In the spatial imaging mode (Fig. 3.4 right) electrons originating from different points in the focal volume are projected onto rings with center distributed along a line which form cigar-like shape and directly reflects the ionization volume.

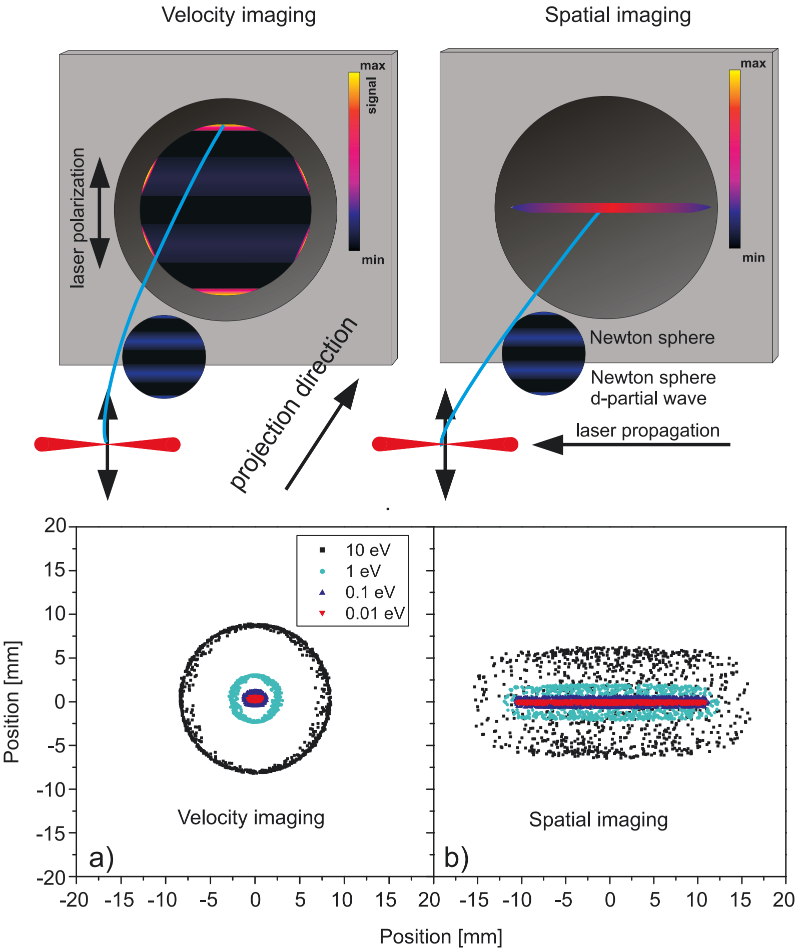

Figure 3.4: Top: Two operation modes of the velocity imaging spectrometer: velocity imaging mode (left) and spatial imaging mode (right). In velocity imaging mode, all electrons are emitted from a focal volume with a given momentum are projected onto the same ring in the detector plane. Volumetric effect leads to ring broadening. Thus, information on angular distribution is preserved and encoded in the angular ring coordinate. In spatial imaging mode, in turn, projections form a cigar-like shape in the detector plane which directly reflects an ionization volume. Bottom: Calculated with SIMION projection of electrons emitted from a focal volume of 10 mm length in the velocity imaging mode (bottom left) form characteristic rings. In spatial imaging mode (bottom right) only very slow electrons ($E_{kin} < 0.1$ eV) are projected onto a line with high signal intensity. Whereas the velocity imaging mode is employed to study momentum-resolved photoeletron/ion spectra. The spatial imaging mode can be employed to align laser in the VMI spectrometer and to investigated e.g. Gouy-phase shift in the focal volume, see Chapter. 5.3.

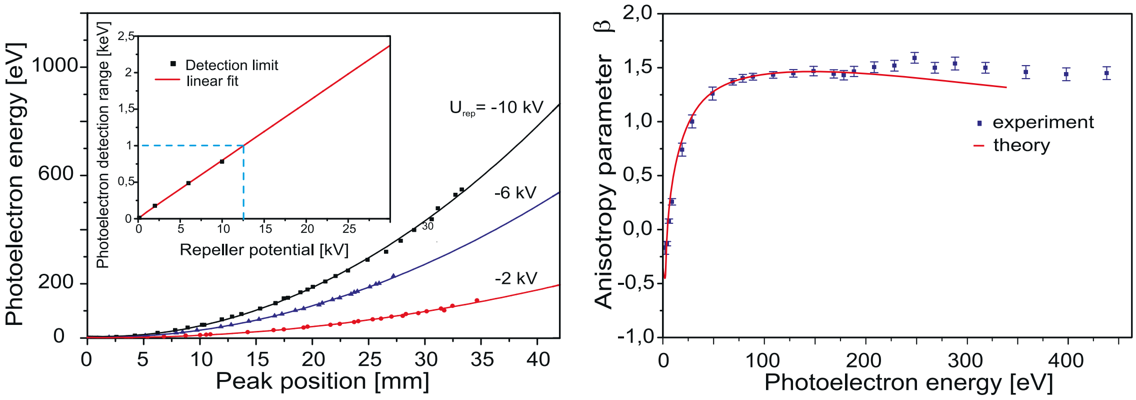

Figure 3.5: HEVMI characterisation by means of XUV photoionization of Ne. Left: calibration curves for three repeller settings show a typical quadratic dependence. The maximum accessible energy detection range for a given repeller setting is shown in the inset. Right: extracted anisotropy parameter of 2p photoemission as a function of XUV photon energy. The strong energy dependence of the angular distribution (points) is in good agreement with the theoretical calculations (solid line [176]).

Thus, electrons with very low momentum form practically a line on the position sensitive detector. In the lower panel SIMION calculations performed for extended focal volume illustrate this effect. Whereas the velocity imaging mode is employey to study angular-resolved photoelectron/ion specta, the spatial imaging mode is typically employed to align a laser focus position and can be utilized to investigate e.g. the Gouy phase shift in the focal volume as shown in Chapter 5.3.

Transmission and focusing properties of the HEVMI spectrometer design have been tested at different photoelectron energies. Ti:sapphire laser system and the synchrotron source DORIS (at DESY Hamburg)served as light sources. For higher energies (15 to 600 eV) the experiments have been conducted at the monochromator beam line BW3 at HASYLAB DORIS in Hamburg [172]. We choose 2s and 2p photoemission from atomic neon because of the optimal balance between ionization cross-sections and electron binding energies [173]. The HEVMI spectrometer was located at a distance of 0.7 m from the focal point of the monochromator, which results in an elliptical spot (162 μm in the vertical by 410 μm in the horizontal (full width half maximum)) at the interaction point with a divergence of about 0.1 mrad. Further details can be found elsewhere [174; 175]. Photoelectrons with energy up to 600 eV were detected with the 80 mm VMI detector.

In Fig. 3.3 (right) the angular-resolved spectrum from Ne ionized with soft x-ray photons of $h\nu = 230\,\mathrm{eV}$ is shown. Single-photon absorption leads to the emission from 2s and 2p levels having binding energies of 21.7 and 48.5 eV, respectively. The electrons form ring-like patterns on the detector with well-known angular distributions [177].

Because of the larger 2p ionization cross-section, the outermost ring exhibits a higher intensity. At the chosen photon energy, the 2p fine splitting of $\Delta E = 0.1\,\mathrm{eV}$ cannot be resolved. Neon photoemission over a broad energy range has been recorded by scanning the photon energy up to 600 eV. We adapted a repeller voltage to the photon energy in three steps to use the full width of the active detector area. By integrating the angular signals, the photoelectron spectra have been extracted and used for calibration (Fig. 3.5). Above a photon energy of 500 eV, the 2s and 2p states can no longer be resolved and an average energy value has been used in the calculations. This implies that the resolution at higher energies is still about 10 %. It has to be emphasized that the experiment has been performed with an unfocused beam. Thus, photoemission proceeds along the entire axis of the soft x-ray beam. This leads to a significant photoelectron peak broadening because of the volumetric effect, which reduces the effective resolution of the VMI system. The resulting calibration curve as depicted in Fig. 3.5 (left) can be approximated by a second-order polynomial. This procedure assures an assignment of the electron energy with a precision of about 4% in further experiments.

The absorption of a photon results also in a transfer of angular momentum. Optical transition rules state that for linearly polarized light $\Delta l = \pm 1$. Thus the emission from the 2s orbital results in a p-type partial wave. The angular distribution mapping capabilities at higher energies are studied by considering the energy-dependent anisotropy parameter β. For linearly polarized light the angular distribution $I(\Theta)$ can be described by:

$$I(\Theta) = 1 + \beta(\frac{3}{2}cos^2\Theta - \frac{1}{2}) \tag{3.1}$$

where β denotes the anisotropy parameter and Θ the angle between the direction of the ejected electron and the polarization axis of incident light [177]. Emission from 2p states leads to s- and d-waves, which experience a photon energy dependent phase shift because of interaction with the Coulomb potential. If they interfere destructively, a negative value of β is expected, and a positive value for constructive interference [178]. The results in Fig.3.5 (right) show a strong dependence on β as a function of the ionizing photon energy. Up to $\hbar\omega = 50\,\mathrm{eV}$ the anisotropy parameter increases rapidly from $\beta = -0.2$ at low energies to approaching a value of $\beta = 1.3$ being followed by a plateau. The strong dependence of β as a function of photon energy agrees well with theoretical calculations, which however predict a slightly lower value of β for photon energy range above 250 eV [176]. This deviation is caused by the increasing overlap between 2p and 2s contributions because of the focus conditions, which limit the resolution.

3.3 ω-2ω experimental procedure

In the experiment, noble gases (He, Ne, Ar, Kr, Xe) CO_2 and N_2 molecules are ionized with ω-2ω laser pulses. No attempt was made to align the molecules initially. Intense

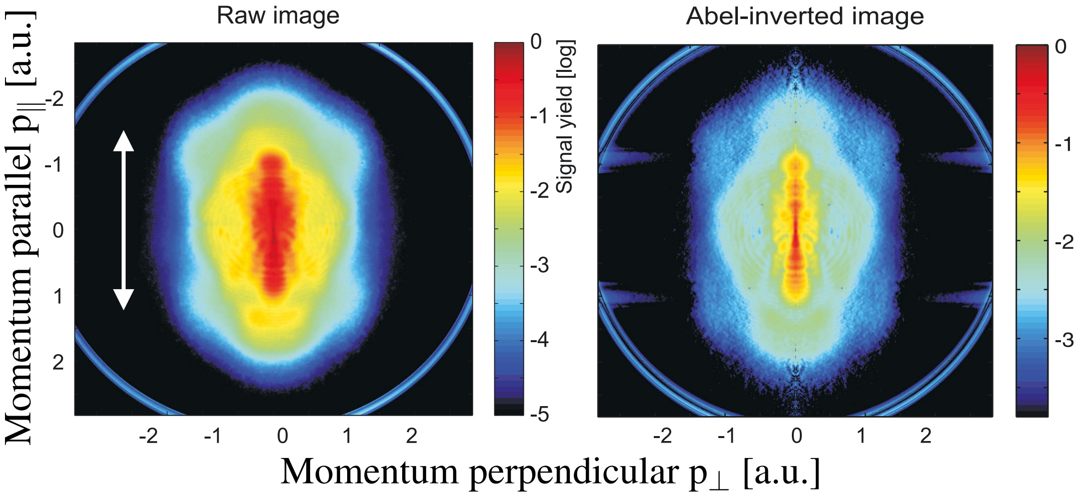

Figure 3.6: Raw and Abel-inverted imaging spectrum of Xe ionized with strong bichromatic laser pulses. The inverted spectrum is cut through a 3-D momentum distribution in the laser polarization plane. The characteristic noise line along the laser polarization axis is an artefact resulting from integration.

ω pulses with 130 fs pulse length were frequency doubled in a BBO crystal. The pulse length of the ω component is measured at the output from the laser system and in front of the focusing mirror. No significant pulse broadening was detected ($\Delta t_{\omega} < 5\,\%$). To find the optimum time overlap between ω and 2ω the photoelectron energy is measured in a cross-correlation scan (for details, see Fig. 3.2 right). The peak in the cross-correlation scan has been chosen as a starting point for the measurements. In each scan, the fused-silica wedges were moved in 200 motor steps, which corresponds to a relative phase interval of about 3π. The averaged intensity of the $I_{2\omega}$ is about $1\,\%$ of the lowest I_{ω} utilized. The power of both components is measured using a thermal head averaged over 10 ms. It should be noted that the average laser power is monitored before and after each scan. Thus, we ensure that the laser power drift is not larger than a few percent. To calculate the intensity, the Gaussian beam approximation is employed. Most of the measurements are performed for constant 2ω intensity, which is controlled by detuning the BBO crystal from phase-matching conditions. As demonstrated above, the polarization of the SH is not affected by tilting the crystal (see Fig. 3.2).

During operation of the HEVMI, the residual pressure is kept to about 10^{-9} mbar. The gas pressure during the experiment is about 5×10^{-7} mbar. This condition ensures that space charge effects are excluded. A further increase in the gas pressure induces discharges between the elements of the gas injection system, which is integrated in the repeller electrode. To resolve electrons with $E_{kin} = 120\,\mathrm{eV}$, the repeller potential was adjusted to $U_{rep} = -12\,\mathrm{kV}$. Suppressing the background contribution from the residuals is achieved by applying a 130 ns pulse from a high voltage switch (Behlke Model HTC),

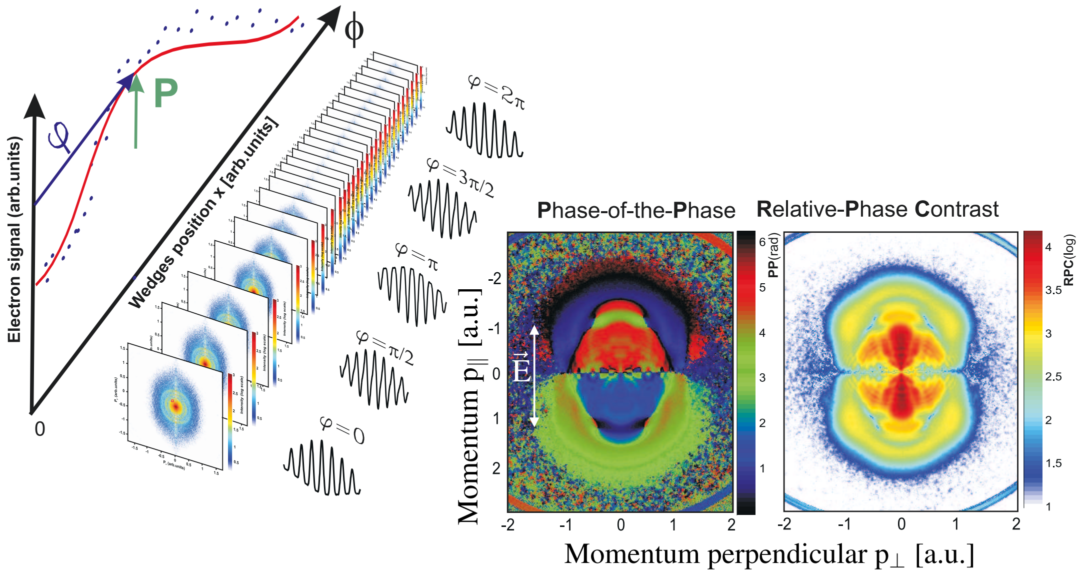

Figure 3.7: Principle of the $\mathcal{P}o\mathcal{P}$ spectroscopy. The phase-dependent angular-resolved photoelectron signal is analysed via the Fourier transform. For each final momentum, PP and RPC corresponding to FH in the Fourier power spectrum can be plotted. PP quantifies a time lag at which the photoelectron's signal oscillates with respect to the relative $\omega/2\omega$ phase (ϕ) whereas RPC describes how strongly the signal oscillates. The laser polarization direction is indicated by arrow.

which gates the back plate of the MCP. Such a procedure leads to a significantly reduced background. To record a typical spectrum, the signals from 100–300 laser shots are accumulated (camera shutter open for 100–300 ms). Thus, each image is accumulated over 100–200 spectra depending on the signal strength. To avoid signal saturation, we carefully set the maximum signal on the camera by fine-tuning the acquisition time and controlling the MCP amplification. By this, even single electron events can be detected, which is important to identify the $10U_p$ energy cut-off.

3.4 Abel transformation

The angular-resolved photoelectron spectra obtained with a VMI spectrometer are projections of Newton spheres onto the 2-D plane of a position-sensitive detector. Mathematically, it can be viewed as a projection of a function $f(x,y,z)$ representing electron density in the continuum, along the spectrometer axis by the electric field ($\overrightarrow{E_{el}} = [0,E_y,0]$) of the HEVMI spectrometer. The projection is defined as:

$$P(x,z) = \int_{-\infty}^{\infty} f(x,y,z)\,\mathrm{d}y = 2\int_{0}^{\infty} f(x,y,z)\,\mathrm{d}y \tag{3.2}$$

and can be considered as projection of a sum of slices where z co-ordinate is considered as a parameter:

$$\sum_n f(x,y,z_n+dz) = \sum_n f_z^n(x,y) \tag{3.3}$$

For linearly polarized light, the photoelectron distribution on the Newton sphere is axially symmetric with respect to the polarization direction, here along z. Thus, the distribution is independent of the azimuthal angle, i.e. the angle in the slice plane. Consequently, both of the Cartesian coordinates x and y can be substituted by a radial coordinate $r = \sqrt{x^2+y^2}$:

$$f_z(x,y) = f_z(\sqrt{x^2+y^2}) = f_z(r) \tag{3.4}$$

Including slicing and substitution above, the projection defined in Eq. 3.2 can be rewritten:

$$P_z(x) = 2\int_0^{\infty} f_z(r)\,\frac{dy}{dr}\,dr = 2\int_0^{\infty} f_z(r)\,\frac{r\,dr}{\sqrt{r^2-x^2}} \tag{3.5}$$

This equation is called the Abel integral and describes the forward projection of a slice of a 3-D distribution with an axial symmetry onto the 2-D plane [179]. It is possible to retrieve $f_z(r)$ from the projection by the so-called inverse Abel integral (Abel transformation)

$$f_z(r) = -\frac{1}{\pi}\int_r^{\infty} \frac{dP_z(x)}{dx}\,\frac{dx}{\sqrt{x^2-r^2}} \tag{3.6}$$

Many other algorithms have been invented in previous years. As they are not used in present work, they are not discussed. Detailed information can be found in other publications [180; 181; 182; 183; 184; 185; 186; 187].

Figure 3.8 ***(following page)*****:** PP (left) and RPC (right) spectra from Xe corresponding to first, second and higher-order harmonics in the Fourier power spectrum. Although the RPC signal decreases significantly for second and higher harmonics, the PoP signal persists up to $\Omega = 4$.

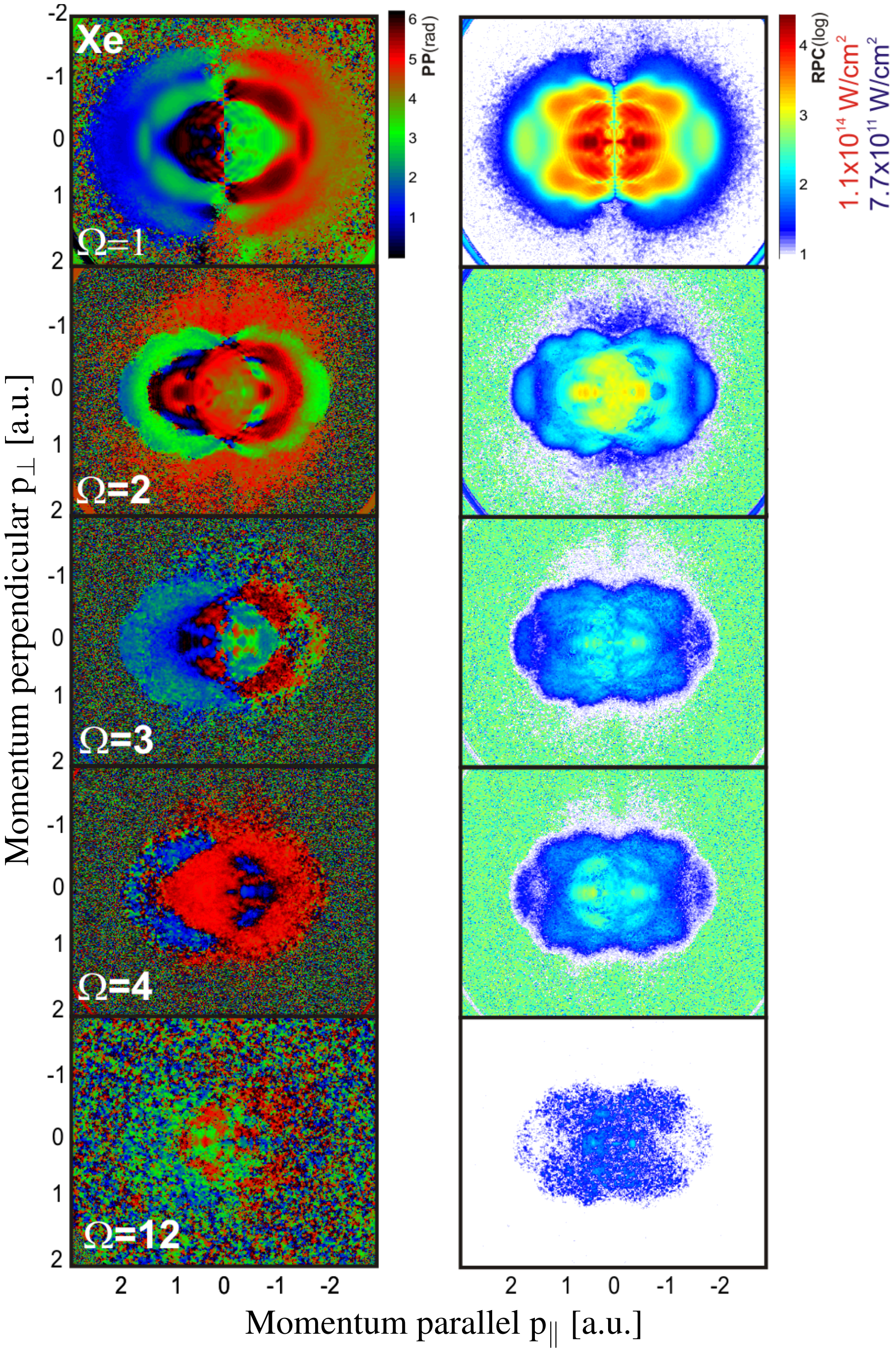
Xe
Ω=1
Ω=2
Ω=3
Ω=4
Ω=12
PP(rad)
6
5
4
3
2
1
RPC(log)
4
3
2
1
1.1x10^14 W/cm^2
7.7x10^11 W/cm^2
-2
-1
0
1
2
Momentum perpendicular p⊥ [a.u.]
Momentum parallel p|| [a.u.]

3.5 Data analysis

The electron wavepacket upon dynamical evolution and rescattering is emitted into 3-D Fourier space. The observable is a projection of the spatial momentum distribution onto the position-sensitive detector. Therefore, detailed information about the momentum-resolved photoemission requires analysing the signal in each point of the imaging spectrum. Two methods are employed to visualize $\omega/2\omega$ dependent momentum-resolved electron yields. The Fourier transformation of the phase-dependent electron yield can be performed as illustrated in Fig.3.7. For a given momentum (p_{x_i}, p_{z_i}) the relative phase ϕ

dependent signal is analysed by means of the fast Fourier transform. As a result we obtain the complex entity:

$$\mathcal{P}(p_x, p_z, \Omega) = P(p_x, p_z, \Omega)e^{i\varphi(p_z, p_z, \Omega)} \tag{3.7}$$

where P $\geq$ 1 stands for Relative Phase Contrast (**RPC**) and φ for Phase-of-the-Phase (**PP**). The modulation of the PP is assumed to follow the 2ω frequency ($\Omega = 1$). Although higher-order terms are present ($\Omega = 2, 3, ...$) the corresponding RPCs are weak and are neglected in this work, as illustrated in Fig. 3.8. The RPC signal for $\Omega = 2$ drops already by about two orders of magnitude. However, the corresponding PP persist up to $\Omega = 4$.

It is convenient to represent RPC and PP in a momentum-resolved colour scale. The

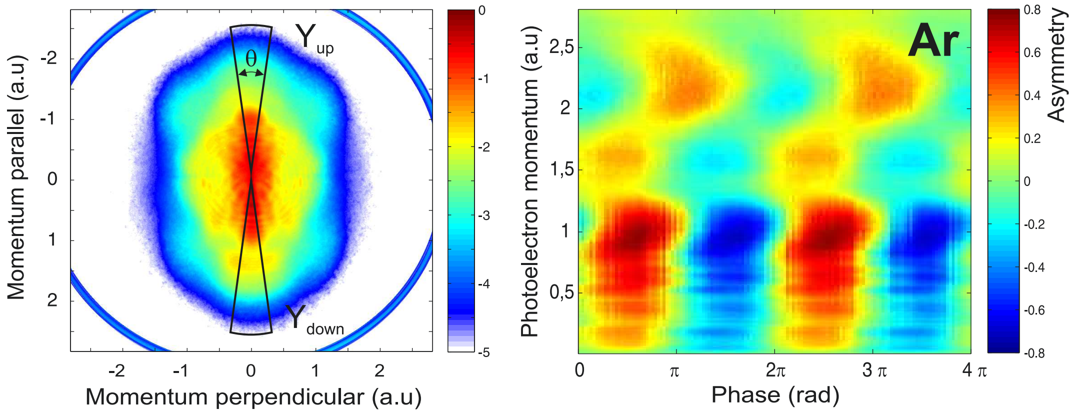

Figure 3.9: Left: Ar photoelectron momentum spectrum ionizes with ω-2ω laser pulses of intensity $I_\omega = 1 \cdot 10^{14}$ W/cm^2 and $I_{2\omega} = 1 \cdot 10^{12}$ W/cm^2. Right: phase-dependent asymmetry parameter calculated from the angular section of the imaging spectrum for each ϕ. Variation of asymmetry in various segments of the momentum spectrum are readily resolved.

phase convention is chosen such that the yield changes as $\cos(\phi + \varphi)$. The absolute phase is not determined by the experiment but by comparison with theoretical calculations. PP are plotted in a colour map where $\varphi = 0$ and $\varphi = 2\pi$ are encoded by the same colour (black). RPC spectra are encoded in a log colour scale. Note that the background level in RPC is offset and encoded as white. We emphasize that a similar method (based on fitting sin functions) has already been utilized to analyse phase-dependent photoelectron signals from SiO_2 nanoparticles and for CEP laser pulses [188; 189].
The asymmetrical signal can conveniently be described by means of an asymmetry parameter [124]. The $\omega/2\omega$ dependent photoemission is asymmetric due to the doubled periodicity of the 2ω component. Every half-period, the maximum electron energy changes from p_z to $-p_z$. Therefore, it is quite intuitive to represent the ω-2ω phase dependency as an asymmetry parameter:

$$A(p_r, \phi) = \frac{Y_{up}(p_r, \phi) - Y_{down}(p_r, \phi)}{Y_{up}(p_r, \phi) + Y_{down}(p_r, \phi)} \tag{3.8}$$

As illustrated in Fig. 3.9 (left) for a given angular range θ the signal is integrated in radial segments centred around p_z i.e. the laser polarization axes. Fig. 3.9 shows the asymmetry map $A(p_r, \phi)$ resulting from ω-2ω ionization of Ar with intensities $I_\omega = 1 \cdot 10^{14}$ W/cm^2 and $I_{2\omega} = 1 \cdot 10^{12}$. Althoughinformation on angular distribution is lost due to signal integration, the asymmetry calculation is robust and enables analysis of data practically in real time.

4 Photoemission from atoms in intense ω-2ω fields

In this chapter we examine important aspects of electron rescattering dynamics in an atomic system subjected to ω-2ω fields. Understanding of these dynamics is a prerequisite for applying $\mathcal{PoP}$ to larger systems, e.g., molecules or clusters. We discuss PP and RPC spectra from rare gases, which exhibit universal patterns independent on the laser intensity and ionized atomic system. We implement simple man's theory (SMT) to model the phase dependent photoelectron yield in momentum resolved spectra. The PP spectra reveal the influence of both the spreading of the photoelectron wavepacket and of the differential scattering cross-section (DSC) on the rescattering dynamics. In parallel, we employ SFA and TDSE methods to validate SMT. To the best of our knowledge, SMT has not been applied to analyse the phase-dependent photoemission in ω-2ω laser fields in the manner we present in this work.

4.1 Experimental results

We perform the experiments with laser intensities that range up to $I_\omega = 10^{14}\,\mathrm{W/cm^2}$. The Keldysh parameter [159] for most cases is $\gamma_k = 1$, i.e., tunnelling ionization conditions, see Section 1.2 [190]. The intensity of the streaking 2ω field is about $1\,\%$ of the intensity of ω field. Thus, we can treat it as a weak perturbation [1] [47]. These conditions ensure that the electron dynamics (tunneling and rescattering) are dominated by the ω field only. A proof will be presented below.

Fig. 4.1 illustrates a typical angularly-resolved photoelectron spectrum resulting from ω-2ω ionization at $\phi = 0$. We indicate signatures such as ATI as well as side lobes, and describe them briefly in section 1.4. Spectra like this one can be recorded for different Φ settings, see Fig. 4.2 on the left side.

---

[1] Dudovich et al investigate HHG driven by a ω-2ω field. In their experiment HHG enters the perturbation range when $I_{2\omega}/I_{omega} = 0.1\%$ while for 1% onset of control on electron trajectories sets up. In our convention, we examine ionization process and we assume that perturbative range ranges up to 1%

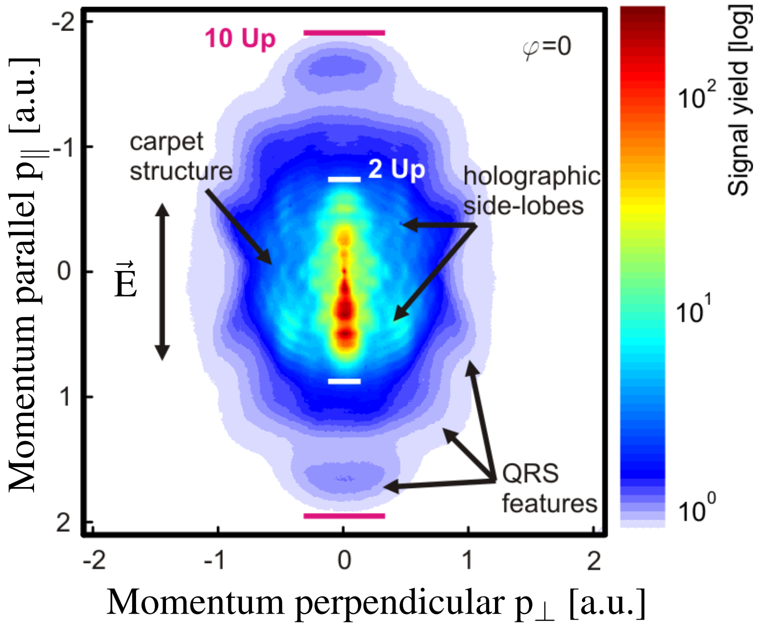

Figure 4.1: Angularly resolved photoelectron spectrum of Xe ionized with ω-2ω pulses of intensity $I_\omega = 1.3 \cdot 10^{14}\,\mathrm{W/cm^2}$ and $I_{2\omega} = 1.5 \cdot 10^{12}\,\mathrm{W/cm^2}$. The laser polarization is linearly polarized in the vertical direction. Asymmetrical emission along the laser polarization axis reflects probable asymmetrical ionization in the ω-2ω laser pulse. Classical cut-offs for direct ($2U_p$) and rescattered ($10U_p$) electrons are indicated by lines. Characteristic features labelled in the spectrum are discussed in section 1.4.

The photoelectron momentum spectra are taken from Xe ionized with ω-2ω pulses. Obviously a clear phase effect is present, with a variety of spectra features being sensitive to the ω-2ω phase. Similar observations have been reported by Ray *et al.* [61], but for a much stronger 2ω field. Due to graphics limitations not all of the spectral features can be rendered in Fig. 4.2. Briefly, the strongest variation in signal yield from electron emission along the laser polarization axis is due to optical tunnelling ionization, which is favoured in the polarization direction. Weaker oscillations are resolved in the region of the holographic side-lobes. Both contributions oscillate in phase. In the HATI range ($4-10U_p$), the signal oscillates out of phase with a smaller amplitude. A similar effect has been already reported for few-cycle laser pulses [122]. Maxima in the carpet structure change their polar coordinates periodically. We discuss this effect in more detail later (see section 4.4).

In Fig. 4.2 (right) we present the photoelectron spectra extracted along the laser polarization axis for $p_z < 0$ (green) and $p_z > 0$ (blue), which illustrate energy dependent signal yield. Relation of low energy and HATI electrons can be resolved as signal yield being asymmetrical for different phases. The weak 2ω component introduces perturbations to the ionization and rescattering times, as shown in Fig. 2.4. As a result, the

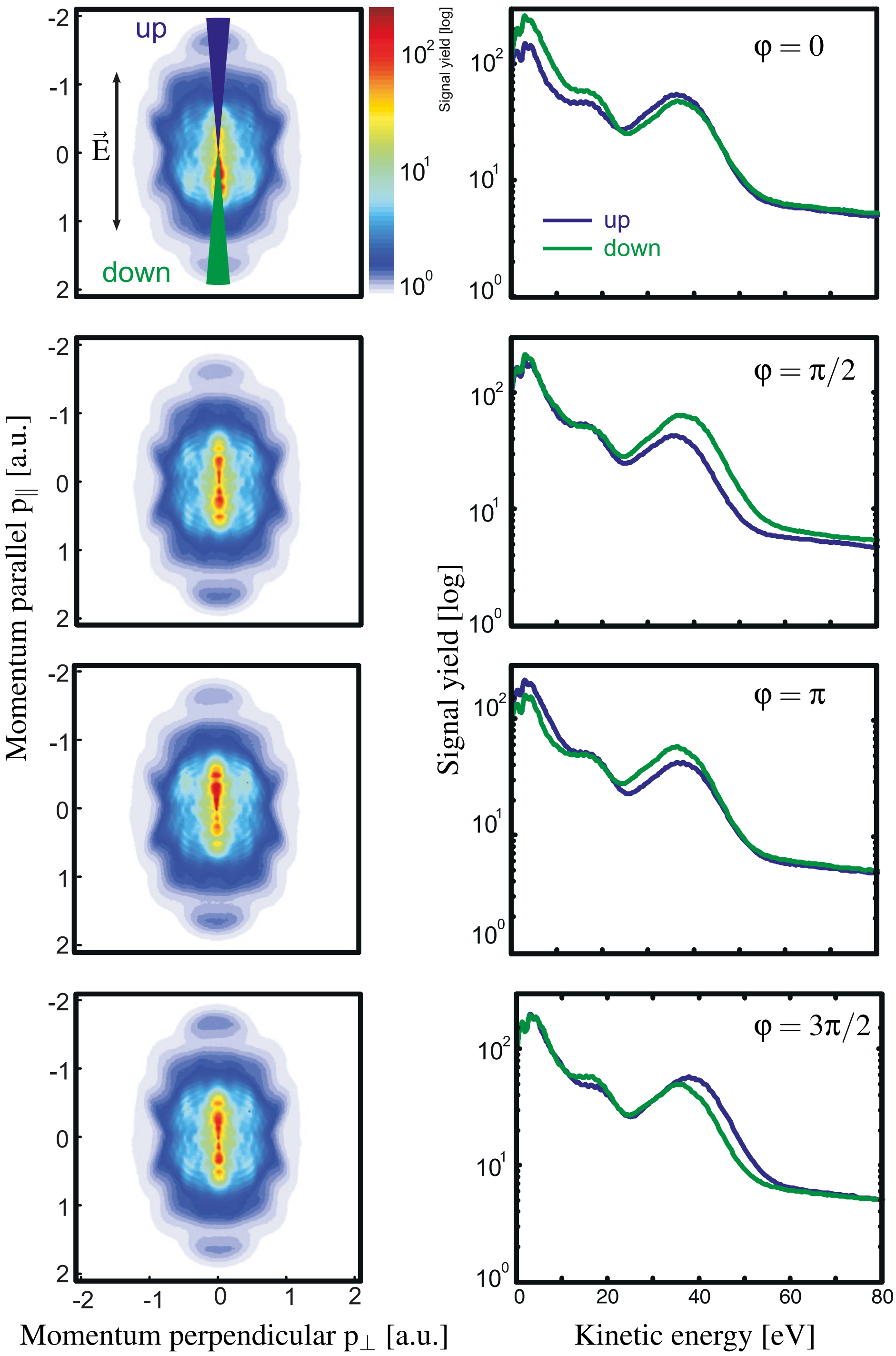

Figure 4.2: Left: Phase-dependent momentum spectra of Xe ionized with asymmetrical pulses with the same intensity as in Fig. 4.1. The laser is liearly polarized in the vertical direction. Right: Photoelectron spectra are extracted upwards (green) and downwards (blue) along the laser polarization direction to illustrate detailed phase dependencies. Asymmetrical photoemission is due to an asymmetrical ω-2ω field. Note similarities with results obtained by Paulus (fig. 1.9).

electrons end up with slightly different kinetic energies depending on the relative phase of the ω-2ω field. This effect can clearly be seen in the slope and cut-off of the rescattering electrons as well as in the energies at which minima (10 eV and 25 eV), maxima (15 eV and 40 eV) occur; these energies vary as a function of relative phase. The ponderomotive energy of the 2ω component (1 meV) makes a negligible contribution to the final electron momentum. Note, that $\phi = 0$ can be identified when compared with theory, as presented in further discussion.

A question arises as to whether the control of the electron dynamics by ω-2ω is similar to CEP-dependent excitation in few-cycle laser pulses. The two-color experiment shows some similarities to results obtained for few-cycle phase-stabilized pulses with a comparable intensity [122], (see Fig. 1.9). The rescattering electrons in the HATI range show strong asymmetry that depends on the CEP phase. The direct electron yield (up to 10 eV) oscillates with phase shift of $\approx \pi/2$ relative to the rescattering component (up to 50 eV). HATI electrons create a "plateau" which extends up to the $10U_p$ cut-off. The most striking difference from [122] is the presence of signal modulation in the direct electrons and in the HATI regime. This signal modulation arises from constructive and destructive interference between trajectories that end with the same final momentum [61]. Similar effects are observed in the HHG channel [191]. Since the signal for a ω-2ω excitation pulse consists of many cycles, the electron dynamics is not limited to a single period of the electric field. Thus, multiple returns, or rescattering events at second and higher returns, are possible which modulates the interference pattern and electron yield. This effect will be a central point of further discussion. In contrast, for the few-cycle CEP laser pulses, multiple returns are suppressed.

4.1.1 Phase-dependent photoemission

In order to quantitatively study the phase-dependent photoelectron imaging spectra, we employ $\mathcal{PoP}$ spectroscopy to obtain PP and RPC spectra. Fig 4.3 displays a typical example of PP and RPC spectra. In this section we briefly discuss a prominent features in such spectra.

The PP spectra enable a straightforward identification of regions where the phase of the signal is related. The color scale Fig 4.3(left) encodes the relative phase lag (φ) with respect to the relative phase of ω-2ω pulse (ϕ) at which the photoelectron signal oscillates. Note that the overall absolute phase is not determined experimentally, but can be assigned when compared with theory. For clarity, the $10U_p$ limit for the rescattered electrons and the $2U_p$ limit for direct electrons are labeled. Note that the $2U_p$ limit separates the region accessible to direct electrons from the region where rescattering electrons appear. Direct electrons ($E_{kin} < 2U_p,\ p < 1$) create a tip-like structure. Rescattered electrons, in turn, oscillates with the same phase φ as the direct electrons on the "opposite side" of the PP spectrum. Both phase-related regions create a club-like shape due

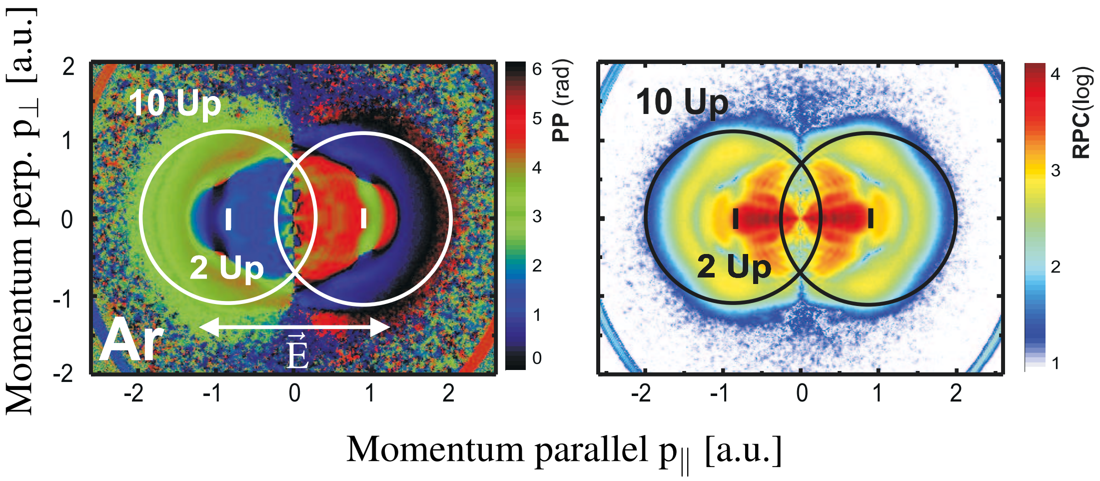

Figure 4.3: PP and RPC spectra for Ar ionized with ω-2ω field with intensity $I_\omega = 1.1 \cdot 10^{14}\,\mathrm{W/cm^2}$ and $I_{2\omega} = 1.5 \cdot 10^{12}\,\mathrm{W/cm^2}$. The linear color scale in PP spectrum encodes the relative phase lag at which the electron signal oscillates with respect to the relative phase $(0-2\pi)$. The blue to black color range $(p_z > 0)$ indicates that the electron yield exhibits $\sin\varphi$- to $-\cos\varphi$-like variations. The green to red color range $(p_z < 0)$ indicates that electron yield exhibits predominately $\cos\varphi$- to $-\sin\varphi$-like variations. PP enables the identification of the area where the electron signal variations are phase-related. The RPC spectrum (encoded in log scale) reflects how strongly the signal oscillates. The laser polarization direction is indicated by arrow.

to electrons released during the common laser subcycle, which is directly reflected in SMT, (see Fig. 2.1). On both sides, there is a region which exceeds the $2U_p$ limit for direct electrons. Notably, it follows the phase-wise behaviour of direct electrons, which appear on the same side of spectrum. These universal structures are a central feature of our further discussion, and are modelled by refined SMT. Besides continuously distributed universal structures, alternating patterns can be resolved. An ATI pattern can be recognized as fine phase oscillations within the direct electron range. Perpendicular to the polarization axis, alternating patterns reflect changes in the position of interference maxima. These features result from interfering wavepackets and are discussed separately.

The RPC spectra encode the amplitude of the signal oscillation and enhance the con-

---

Figure 4.4 ***(following page)*****:** Comparison of spectra for noble gases ionized with ω-2ω laser pulses of similar intensity. Left: PP spectra. Right: RPC spectra. For Xe only, $I_{2\omega}$ is reduced by factor of 2 to account for the lower ionization potential. Laser parameters are indicated on the right side of the figure. Classical cut-offs for direct $(2U_p)$ and rescattered $(10U_p)$ electrons are labelled. PP spectra show very similar phase dependence, forming overlapping club features on both sides of the PP spectrum. For RPC, a logarithmic color scale is used.

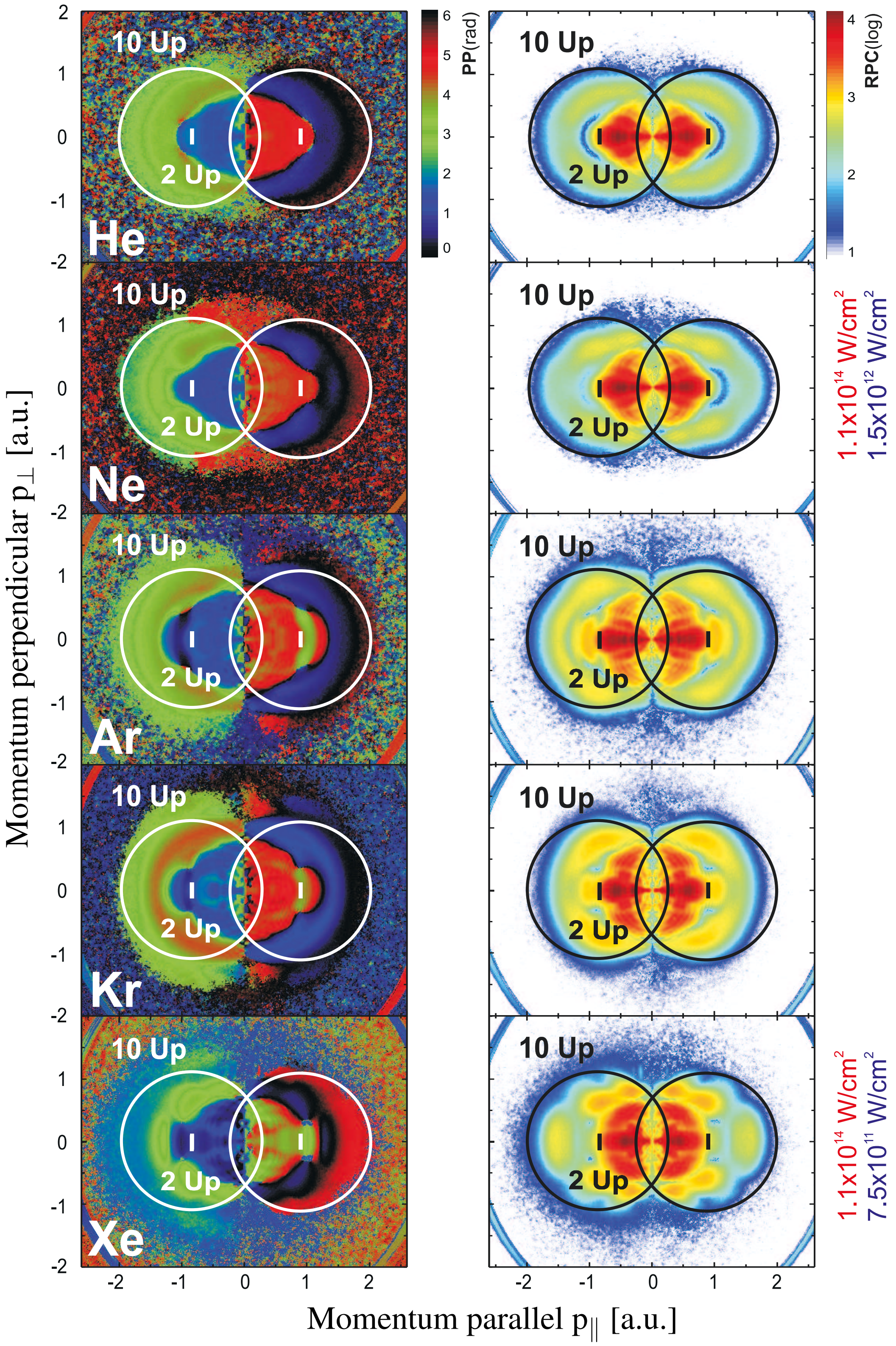
10 Up
2 Up
He
Ne
Ar
Kr
Xe
PP(rad)
0
1
2
3
4
5
6
RPC(log)
1
2
3
4
1.1x10^14 W/cm^2
1.5x10^12 W/cm^2
1.1x10^14 W/cm^2
7.5x10^11 W/cm^2
Momentum perpendicular p⊥ [a.u.]
Momentum parallel p|| [a.u.]
-2
-1
0
1
2

trast of typical photoelectron features. The strong RPC signal appears along the laser polarization axis, reflecting the high sensitivity of direct electrons on tunneling. Symmetrical to it on both sides, holographic side lobes can be resolved. ATI rings and HATI electrons show target dependent angular distributions.

4.1.2 Target dependence

In SMT, the scattering process depends only on the vector potential of the ω-2ω pulse. Thus, target-independent features can easily be identified in the PP experimental data by comparison with the predictions of SMT shown in PP spectra. All spectra in Fig. 4.4 were obtained for similar laser parameters and show very similar universal patterns independent of the atomic species. Direct electrons are distributed within a tip-like shape. The PP rescattering signals are closely phase-related to the direct electron on the opposite side of the PP spectrum. Both contributions form a club-like structure. Notably, a circle-shaped region extending beyond $2U_p$ can be resolved on top of the low momentum tip in all spectra. Boundary regions in the PP spectrum (between red and blue, and between blue and green on the color scale in Fig. 4.4) have angular patterns whose complexity increase with target mass. In the low-momentum regions, one can resolve fine fluctuations in PP arising from interference between wavepackets. These features exhibits target dependencies.

Target-dependencies can be resolved with much higher contrast in the RPC spectra that in PP, (see Fig. 4.4, right panel). Most notably, the angular dependencies for direct electrons exhibit increasing complexity. For He and Ne targets, for instance, they exhibit fan-like structures. For other targets, a lobster-tail shapes are observed with stronger signal variation at larger angles relative to the laser polarization axis. Target-dependencies are also resolved in the rescattering part of the RPC spectrum. In particular, Xe exhibits multiple nodes in the angular distribution, in contrast to the rather uniform distributions found for the lighter elements. Before we proceed, we first describe how PP and RPC depend on the intensity of both ω-2ω components.

4.1.3 Influence of the 2ω intensity

We systematically investigate the laser intensity dependence in order to study the influence of the 2ω field on ionization and rescattering. The $I_{2\omega}$ field intensity is tuned so as to introduce a weak perturbation and therefore must to be kept far below the ionization threshold. In Fig. 4.5, we present PP and RPC spectra from Ar ionized with $I_\omega = 2 \cdot 10^{14}\,\mathrm{W/cm^2}$ and various 2ω intensities. No significant changes in the PP and RPC spectra are observed when $I_{2\omega}$ intensity is increased. The rescattering cut-off only shifts slightly towards higher momentum. In the PP spectrum in Fig. 4.5 this feature forms a red envelope beyond $10U_p$ cut-off. For $I_{2\omega} = 3.3 \cdot 10^{12}$ W/cm^2 an isotropically

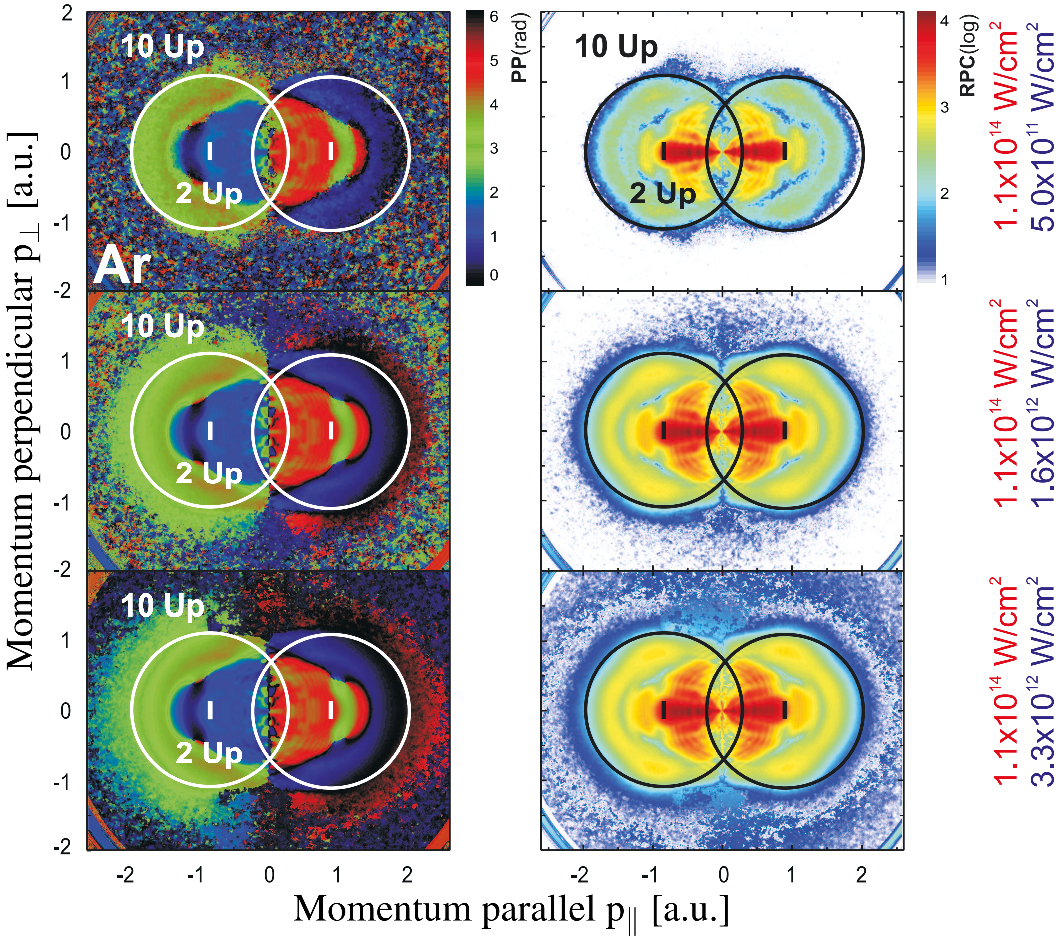

Figure 4.5: The PP (left) and RPC (right) spectra for Ar illustrate dependence on $I_{2\omega}$. No significant changes in overall structure are resolved in the entire momentum range for the SHG field, where $I_{2\omega}/I_{\omega} = 0.5-2\%$. Note that a signal beyond $10U_p$ (red envelope in PP) is generated when the 2ω field intensity is increased.

distributed background signal appears in PP with a constant phase (plotted in blue). In Fig. 4.6, cuts through the PP signal along the laser polarization axis are plotted. We intentionally introduce a phase offset in order to distinguish between spectra for different intensities. The rescattering cut-off shift is clearly seen in this case. Note that noise beyond cut-off is plotted in grey. Other regions of the spectra are not affected. A detailed inspection reveals that even small phase oscillations corresponding to the ATI peaks perfectly overlap. We conclude that for these intensities only a weak perturbation is introduced by ω-2ω field leading to almost no additional ionization. Throughout our study we thus will use $I_{2\omega} = 1.6 \cdot 10^{12}\ \mathrm{W/cm^2}$. Only for Xe lower intensities were applied, $I_{2\omega} = 8.3 \cdot 10^{11}\ \mathrm{W/cm^2}$, to suppress 2ω-ionisation due to the low ionization

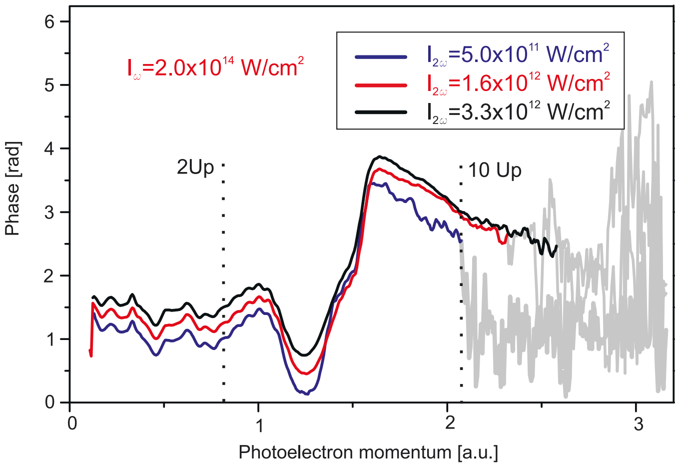

Figure 4.6: The cuts through PP spectra along the laser polarization axis from the spectra shown in Fig. 4.5 illustrate the influence of the 2ω intensity. Spectra show nearly the same course with a characteristic phase jump beyond $2U_p$ ($p > 1$). An offset is introduced to illustrate fine features in the low energy range. Note that noise beyound cut-off is plotted in grey.

potential.

4.1.4 Influence of the ω intensity

The impact of the ω component on the phase-dependent photoemission is illustrated in Fig. 4.7 for two examples: Ne and Xe. For the sake of simplicity, we plot cut through the PP signal along the laser polarization axis. It is convenient to normalize the photoelectron momentum to a value corresponding to $E_{kin} = 10U_p$. The general features of the PP spectra are very similar to before. A low momentum "plateau" extends up to $p_{||} = 0.5 - 0.6$ (corresponding to $E_{kin} \approx 3U_p$). Note that the $2U_p$ limit for direct electrons (dashed line) is still in the plateau region. A small dip at $p_{||} = 0.5 - 0.6$ occurs predominantly at higher laser intensities. For $p_{||} > 0.6$ ($3U_p$) a phase slope builds up that decreases slowly for higher values. For the lowest intensity in Xe the phase slope begins at $p_{||} = 0.45$ (corresponding to $2U_p$). Detailed inspection of the PP spectrum reveals more intensity and target dependencies like intensity dependent slope course and phase signal for $p_{||} > 0.7$. In general, changes in PP phase slope are smoother for lower intensities I_ω. For Xe, the onset of the phase slope is found at $2U_p$, for the lower intensities.

We find that general features of PP are target independent but there are features which show strong target dependencies, especially in RPC. To account for the complexity of both PP and RPC the discussion is divided into sections that are dedicated to particular

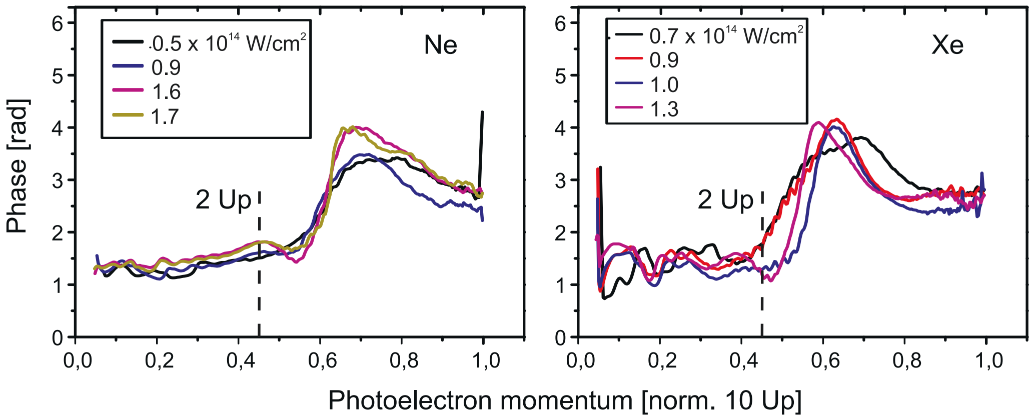

Figure 4.7: The same as in Fig. 4.6 but now for different I_ω, for Ne and Xe. The momentum axis is normalized to $10U_p$. Ne spectra show nearly the same I_ω dependence in the PP, with phase jumps beyond $2U_p$, whereas for Xe the phase jump is shifted towards lower momentum for lower laser intensity.

groups of features. First, we compare the universal club-shaped phase course with SMT. In this manner, we can model processes which affect electron scattering in intense laser fields. Next, we show the influence of the screening parameter and wavepacket dispersion, based again on SMT calcualtions. We describe the angular signal oscillation in PP and compare them with carpet structure discussed elsewhere []. Finally, we address the question of target dependencies by comparing experimental spectra with those obtained from the numerical solution of TDSE.

4.2 Discussion of ω-2ω results with atoms

Fig. 4.8 compares some PP and RPC spectra from SMT with the experimental results for Ar. Calculations performed for $W_r(s=0)$ (a) and $W_r(s=3/2)$ (b) reveal the importance of the wave-packet spreading factor (see Eq. 2.13). Without a $(\tau_2-\tau_1)^{-s}$ "penalty", (s=0) trajectories from the second and third returns scatter with the same probability as from the first return, independent of their propagation time. The wave-packet dispersion favours the first return trajectories due to the exponent factor s in the penalty expression. A clear phase relation emerges from the spectrum when $W_r(s=3/2)$ is included. Two overlapping club-like structures (plotted in blue and red in Fig. 4.8) on both sides of the PP spectrum are due to rescattering during two succesive subcycles of the laser pulse, see the SMT spectrum in Fig. 2.1. The tip of the club at $p_\parallel=1$ a.u. corresponds to the emission of direct electrons. The maximum momentum at $p_\parallel^{max}=\sqrt{5}$ a.u. corresponds to the well-known $10U_p$ cut-off energy. The thin stripe with an opposite phase

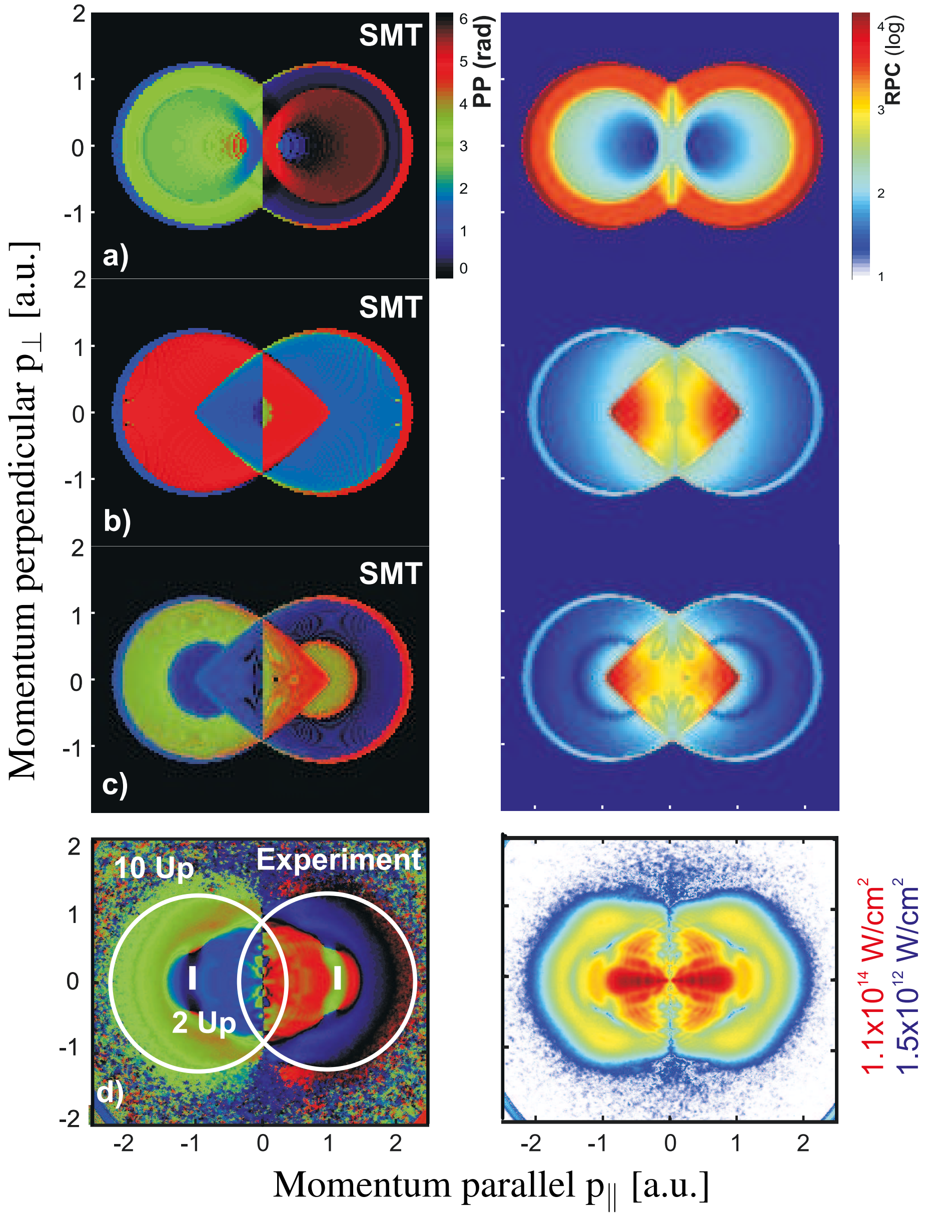

Figure 4.8: Illustration of the importance of the scattering probability on spectra. Left:Model SMT PP spectra. Right: Model SMT RPC spectra. Bottom: Experimental spectrum for Ar. Different effects are included in the SMT calculations: a) tunneling probability, b) wavepacket dispersion for s=1.5, c) DSC in first Born approximation. Spectra for Ar were obtained with $I_\omega = 10^{14}\ \mathrm{W/cm^2}$ and $I_{2\omega} = 10^{12}\ \mathrm{W/cm^2}$. Calculations were performed with SMT code written by D. Bauer.

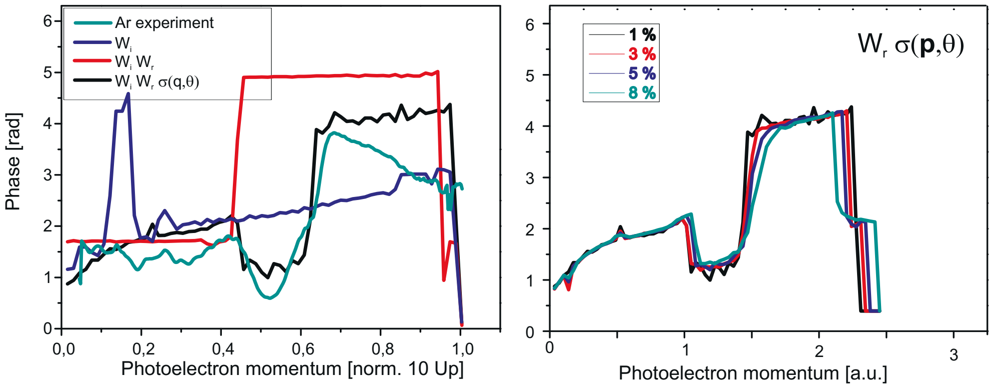

Figure 4.9: Left: cut through the PP spectra in Fig. 4.8 along the laser polarization axis. A model spectrum (black) that includes the DSC shows good quantitative agreement with the experimental results obtained for Ar (green). Right: Influence of the 2ω components on PP spectra from SMT calculations. Note the shift of the high momentum cut-off that accompanies an increase of the 2ω field.

beyond $10U_p$ results from the electrons that gain an additional momentum kick due to the presence of a weak 2ω component. The presence of a weak "tagging" field influences ionization and re-scattering times which we have discussed in Chapter 2. Thus, electrons "feel" the increase in the vector potential when rescattered, (see Fig. 2.4).

By comparing the PP and RPC results presented in Fig. 4.4 with PP adn RPC from SMT Fig. 4.8(right) main discrepancies between experiment and model can be identified:

1 The experimental PP spectra contain far more complex patterns than SMT produces, including wavepacket dispersion (b) which generates essentially only two club structures with a phase offset of π.

2 In all experimental PP spectra, we observe tip extending beyond the $2U_p$ cut-off.

3 The angular distribution pattern in the experimental PP and RPC spectra shows target-dependent features which are not present in SMT. Constructive and destructive interference between propagating photoelectron wavepackets that end up with the same momentum is reflected by maxima and minima in the signal distribution [134]. In SMT, if two trajectories end up with the same momentum, the one which has higher probability is the primary contributor. Thus, interference effects are not included in the calculations.

A PP resulting from refined modelling is shown in Fig. 4.9 (c). Much better agreement with experimental results Fig. 4.9 (d) is achieved. The club tips are extended in the forward direction in a semi-circular pattern. This region behaves phase-wise as forward scattered electrons from first return. This already solves the problem with the phase

jump which occurs at higher momentum (see Fig. 4.7). Another improvement is that the phase in the backward scattering regions is lowered by about $\pi/3$ (from red to green in the PP color scale in Fig. 4.8). Consequently, when including DSC, the phase corresponds much more closely with the experimental spectra.
In the following detailed discussion of the universal phase dependence and the origin of the extended tip beyond $2U_p$ is presented. For the sake of clarity, we simplify the problem of the angular PP dependence by extracting the signal along the laser polarization direction axis. Discuss the origin of the fine structure and the angular dependence in section 4.4.

4.2.1 Universal structures

In Fig. 4.9, the cut through SMT-PP signal along laser polarization axis (Fig. 4.8 (a-c)) are compared quantitatively with the experimental PP for Ar (Fig. 4.8 (d)). In the following discussion, the momentum axes are normalized to the momentum corresponding to $E_{kin} = 10U_p$. When rescattering is weighted by the Landau rate W_i (blue), PP shows a monotonic behaviour with two peaks at low momentum. The phase jump is located at momentum corresponding to $E_{kin} = 2\,U_p$ in the model including W_r, while in the experiment it occurs at momentum corresponding to $E_{kin} \approx 3\,U_p$. This is connected to an extended circular feature beyond the tip which shows phase-wise behaviour with direct electrons. Such phase relations suggest that there is another family of trajectories with enhanced scattering probability that is not included in the model. The model predicts a phase jump $\approx \pi/3$ higher than in the experiment (red curve in Fig. 4.9 left). Moreover, in the experimental spectra a valley in PP precedes the phase-jump, (compare also with Fig. 4.7). The flat PP course indicates, that the signal of all trajectories released during the same half laser cycle oscillates with the same phase. Lowering of the phase-jump indicates that there is another dependency that influences trajectories from the first return. In Chapter 2, we have demonstrated that trajectories that scatter at the second revisit create features that overlap with the first return features up to momentum corresponding to about $E_{kin} = 7\,U_p$. This is, surprising, however, since the penalty W_r (Eq. 2.13) favours the first return contributions, which should have cross sections higher than that from the second return. If the circular pattern originates from the second return there must be an enhanced scattering probability that compensates for W_r and favours much longer trajectories. SMT calculation shows that DSC (including wavepacket dispersion) favours second return trajectories for low momenta and small angles as shown in Fig. 2.7. Such feature should be independent on target.

In Fig. 4.10 (left), we show a comparison of the refined SMT model and TDSE calculations with experimental results obtained for Ar. Independent of the I_ω, all spectra show good agreement with the refined model. Discrepancies are seen at high momentum $p = 0.6 - 1.0$, where the model predicts a rather flat phase behaviour, whereas all experimental spectra show a phase slope. One explanation for the discrepancy may be focal averaging. In the experiment, photoelectrons from an extended focal volume are collected onto the detector. TDSE results correctly predict the phase at low momentum and the phase jump for $p = 0.6 - 1.0$. However, the phase jump is much higher than in the experiment and occurs at lower momentum. We note that classical SMT calculations, which require relatively low computational time, can be performed in order to quantify the importance of both intensity distribution and Gouy phase. The same can be done for TDSE but with much higher computational costs.

The universal character of the PP signal is illustrated in Fig. 4.10 (right). Independent of the target, the experimental PP signal shows nearly the same phase behaviour, in agreements with SMT, but some discrepancies with TDSE are evident. Possible explanation for this discrepancy are discussed in next section. The phase jump position and slope depend on the target as well as well as behaviour at high momentum $p_{\|} = 0.6 - 1.0$. This reflects the sensitivity of the second-return cross section on the scattering potential. Since the SMT model can only predict an universal phase behaviour, in the following we briefly discuss the influence of dispersion (s) and screening parameter (μ) on SMT spectra.

4.2.2 Dispersion rate and Debye potential screening

An electron experiencing oscillatory motion in the multicycle laser pulses can re-encounter the parent ion multiple times [156]. Consequently, it can re-scatter during the first, second or higher-order returns. The rescattering is influenced by both the scattering potential and the wave-packet dispersion in vacuum, a well-known phenomenon in quantum mechanics [192]. Thus, in the refined model there are two main parameters which can be considered as free: the dispersion exponent factor (s) of the wave packet (Eq. 2.13)and the screening parameter in the Yukawa potential (μ) (Eq. 2.18). For the sake of comparison between experimental data and the SMT model it is interesting to see how (μ, s) influence the spectra.

Figure 4.10 ***(following page)*:** Left: comparing SMT and TDSE to experimental data obtained for Ar. Note that the momenutm axis is normalized to a momentum value corresponding to a $10U_p$ cut-off. Experimental data are recorded for constant $I_{2\omega} = 1.5 \cdot 10^{12}\,\mathrm{W/cm^2}$. The TDSE spectrum is calculated for $I_{\omega} = 1 \cdot 10^{14}\,\mathrm{W/cm^2}$ and $I_{2\omega} = 1 \cdot 10^{12}\,\mathrm{W/cm^2}$. The Ar ground state is 3p and the ionization potential is rendered by choosing $Z_{eff} = -17$ and $\alpha = 2.11357$. The DSC calculation (red) shows good agreement with experimental data for all intensities. Right: the same comparison for similar laser intensities but for different targets illustrates the universal character of the PP spectra. The explanation for deviations from TDSE is discussed in section later.

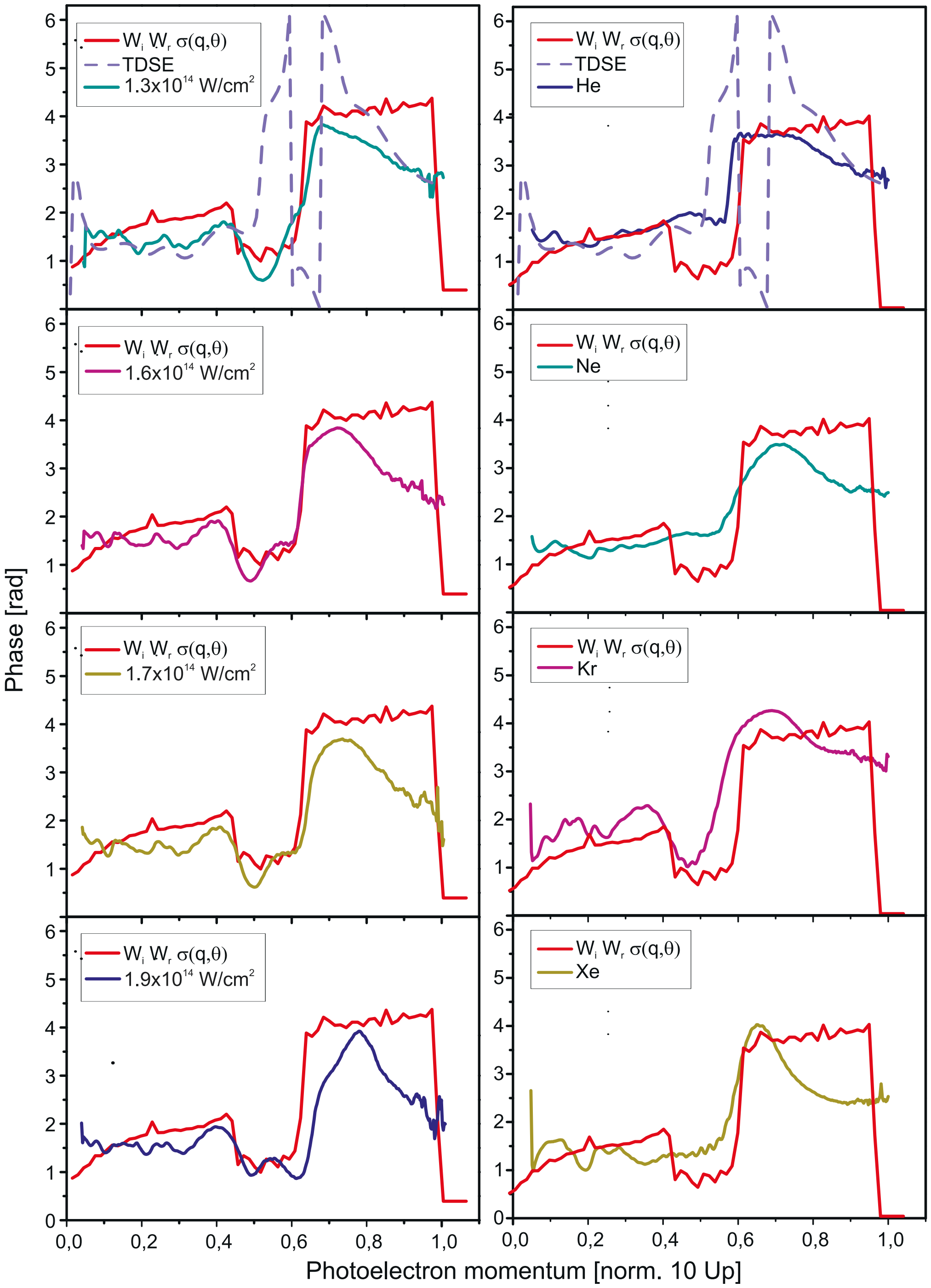
W_i W_r σ(q,θ)
TDSE
1.3x10^14 W/cm^2
W_i W_r σ(q,θ)
TDSE
He
W_i W_r σ(q,θ)
1.6x10^14 W/cm^2
W_i W_r σ(q,θ)
Ne
W_i W_r σ(q,θ)
1.7x10^14 W/cm^2
W_i W_r σ(q,θ)
Kr
W_i W_r σ(q,θ)
1.9x10^14 W/cm^2
W_i W_r σ(q,θ)
Xe
Phase [rad]
0
1
2
3
4
5
6
0,0
0,2
0,4
0,6
0,8
1,0
Photoelectron momentum [norm. 10 Up]

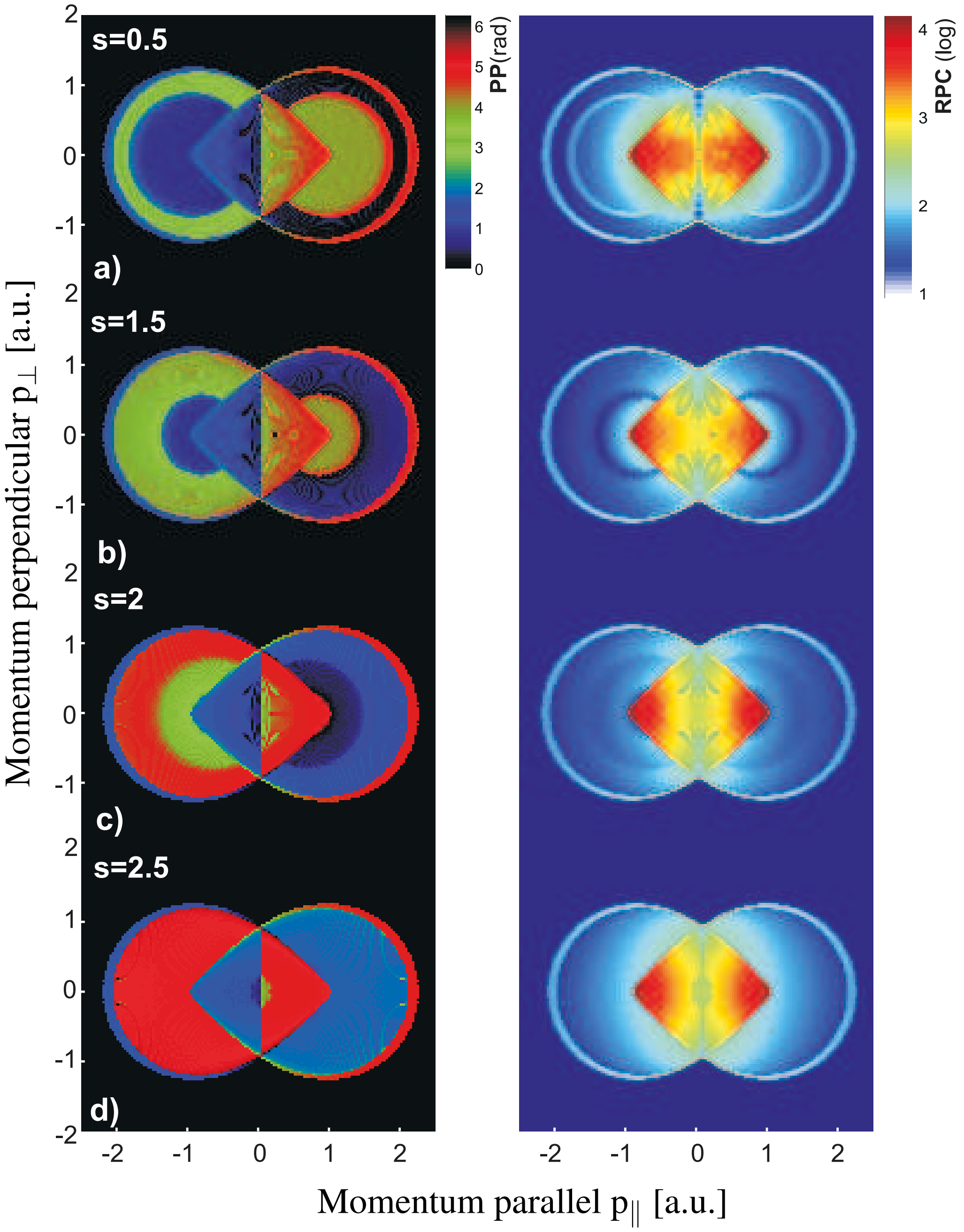

Figure 4.11: Influence of wavepacket spreading on PP and RPC in SMT. Note that the second return contribution, which creates the circular pattern beyond the $2U_p$ cut-off, shrinks as **s** increases. For $s \geq 2.5$, differential cross section effects cannot be resolved. Calculations are performed for screening parameter $\mu = 0.5$ and $\xi = 0.04$. Calculations were performed with SMT code written by D. Bauer.

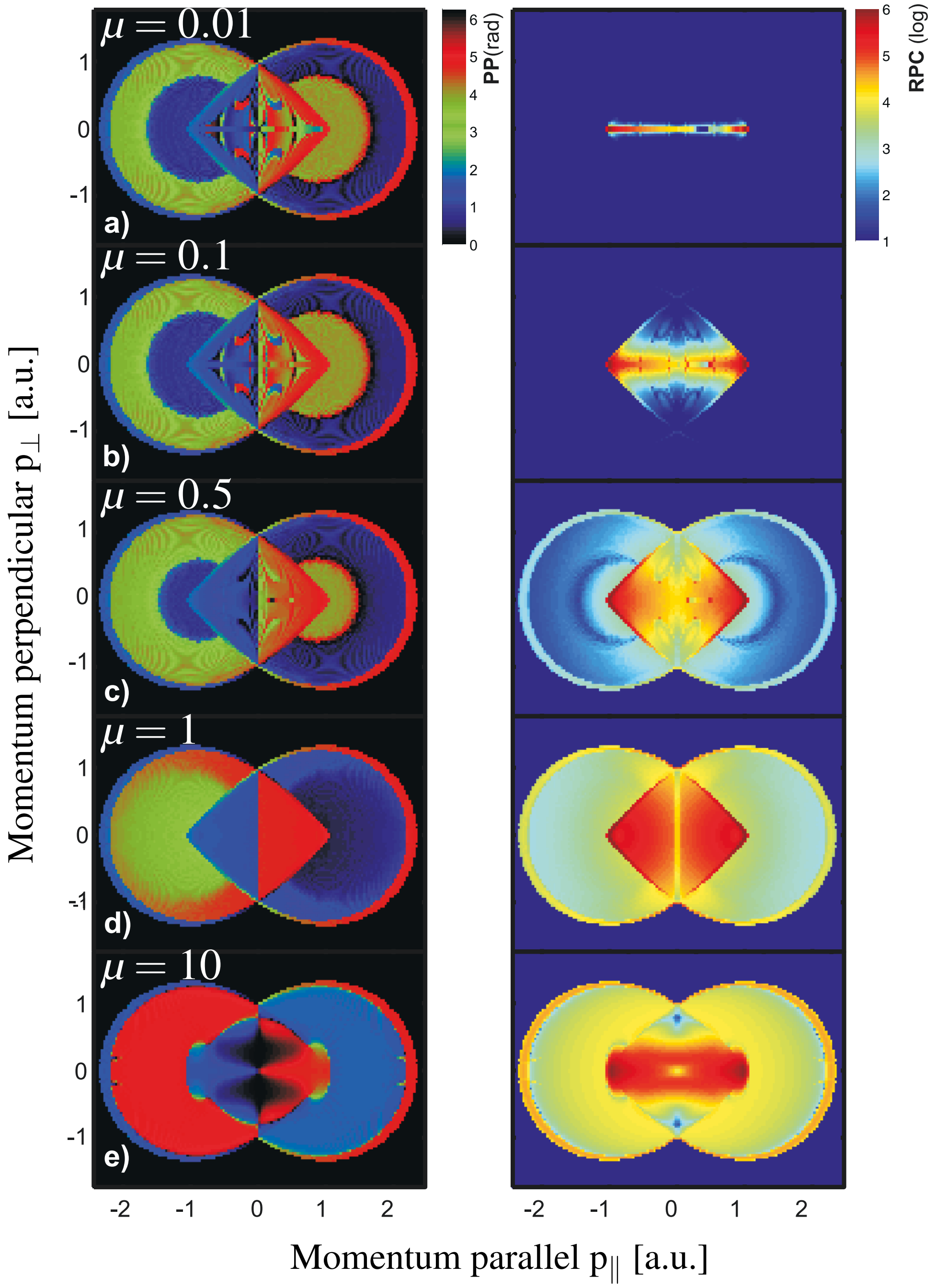

Figure 4.12: Influence of screening parameter μ on PP spectra, based on SMT modelling. Strong phase dependencies can be resolved for $\mu > 0.6$. Second-return contributions are present only for a very narrow range of μ. Angular scattering dependencies are not present for $\mu > 10$. Calculations are performed for $s = 3/2$ and $\xi = 0.04$. Calculations were performed with SMT code written by D. Bauer.

Dispersion rate

Most of the wave packets miss the nucleus at the first return [156]. Coulomb attraction between the electron and ion, however, focuses electrons which are close to the position of the ion and may collide upon the second revisit. In the refined model, electrons scatter elastically depending on their initial conditions upon tunnelling [77]. Since the field is linearly polarized and no spatial dependency arises during tunnelling, the electron motion can be considered as a 1D problem which can be quantified by the excursion α (Eq. 2.4). The trajectories can thus be calculated by means of the classical equation of motion (Eq. 2.12). In the refined SMT modelling the wave-packet dispersion s is described by Eq.2.13. The longer the electron propagates the lower the probability will be for rescattering. The exponent factor $s = 3/2$ is used to mimic Coulomb focusing [79]. Note that for $s = 0$ no dispersion effects are present, (see Fig. 4.7 (a)). In Fig. 4.11, PP and RPC spectra show a strong dependency on s. The radius of the extended circular shape of the second-return contributions depend on s. The calculations show that this radius decreases as s increases (Fig. 4.11 (a,b)). As shown in Fig. 4.11(c), the first return trajectories are also noticeably influenced by increasing value of the dispersion factor. Finally, when $s = 2.5$ (d) PP and RPC spectra are identical to the case with isotropic scattering (compare with Fig. 4.8 (b)).

Screening parameter

In Fig. 4.12 (left) the screening parameter μ for the Yukawa potential is treated as a free parameter (Eq. 2.18). For $\mu < 0.5$, the rescattering component of PP is not influenced and only some fine changes can be resolved in the tip area. In analogy to the s-parameter case, the second-return contributions gradually disappear for $\mu > 1$. Note that the first return contributions that scatter in the forward direction (towards the tip) become less affected by the differential cross-section. Finally, when $\mu = 10$ angular dependencies in the differential cross section cannot be resolved in the PP spectrum.

The Yukawa potential $V(r) = -Z\exp(-\mu r)/r$ reduces to a Coulomb potential for $\mu = 0$. In result, scattering cross-section becomes divergent in forward direction. The Coulomb scattering potential acts on an infinite range and, practically, scatters all trajectories in forward direction [112]. Such scenario is illustrated in RPC spectrum for $\mu = 0.01$ in Fig. 4.12 (right). The dominant RPC contribution is distributed along a line within the energy range $E_{kin} < 2U_p$ which relates to classical limit for forward scattering electrons (see Fig 1.4 [111]). Back-scattering trajectories give negligible contribution to RPC. Note that corresponding PP signal shows clear phase-dependencies since it does not depend on the scattering probability. For $\mu = 0.1$ in Fig. 4.12 (right) the forward-scattered trajectories exhibit more angular dependencies. For $\mu = 0.5$ a RPC contrast (ratio between forward-scattered and backward-scattered regions) reproduces typical value obtained in the experiment (4 orders of magnitude). For $\mu > 1$ the RPC contrast decreases significantly, and corresponding PP dependencies for second-return contributions wash out.

4.2.3 Fine structure in the angular distribution

Interference effects between propagating wavepackets are neglected in SMT. In the experiment, however, periodically distributed maxima and minima at large angles with respect to the polarization axis can be resolved, (section 1.4). Their polar coordinates change periodically as function of the relative phase. This so-called "carpet structure" can be regarded as an interference pattern between electron wave packets released during a single optical cycle in opposite directions around the electric field peak [134; 135]. Its origin can be understood in terms of the quantum orbits that result form an approximation to the SFA matrix element(s), namely saddle point approximation [193]. Trajectories that are emitted at large angles with respect to the polarization axis are moderately influenced by Coulomb interaction with the parent ion. Thus, the interference patterns are pronounced at large angles. Plain SFA can reproduce these signatures very well [134]. Some features can already be resolved in Fig 4.1 in the direction perpendicular to the polarization axis. However, they become more pronounced when studied with $\mathcal{PoP}$ spectroscopy. In Fig. 4.13, an alternating pattern shows up along the direction perpendicular to the polarization axis. Oscillations become less pronounced for smaller angles with respect to the polarization axis due to Coulomb interaction influencing trajectories released at smaller angles. In result, holographic side lobes resulting from two standard SFA trajectories are generated, (section 1.4). We note that similar dependencies can be resolved in PP spectra for other targets.

The origin of fine oscillations in the carpet structure in a ω/2ω experiment can be understood in analogy to [134]: two standard SFA trajectories emitted during subsequent laser subcycles interfere at larger angles. However, in bichromatic laser pulses the weak 2ω field introduces a perturbation to both the ionization and rescattering times (see Chapter 2). Consequently, both the electron quantum trajectories and the accumulated phase during their propagation is modulated. As a result, the interference pattern shows a dependence on the ω-2ω phase. For pure ω pulses it has been demonstrated that within SFA the phase difference between interfering trajectories can be expressed as [134]:

$$\Delta S = \left[\frac{1}{2}(p_\perp^2 + p_\parallel^2) + I_p + U_p\right](t_2 - t_1) - \frac{p_\parallel^2}{\omega} \times \tan(\omega Re t_2) - \frac{2U_p}{\omega}\sin(\omega Re t_2)\cos(\omega Re t_2) \quad (4.1)$$

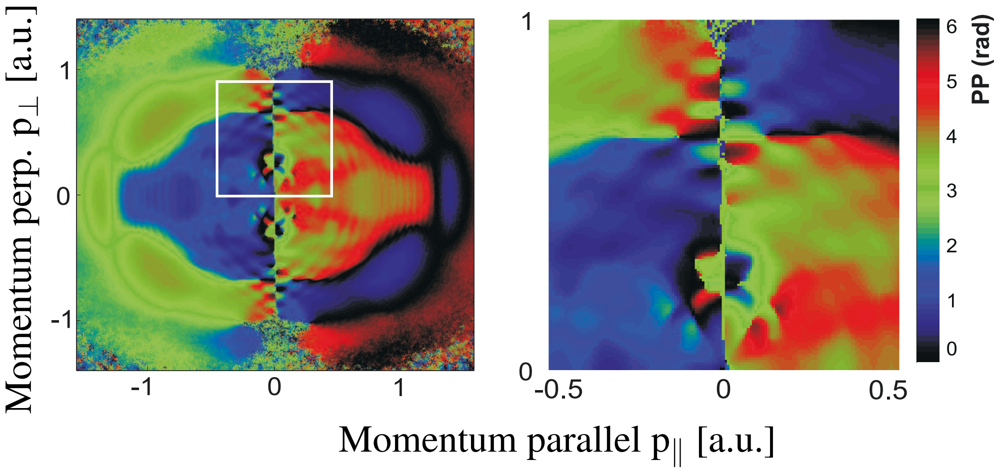

Figure 4.13: The experimental PP spectrum enables us to identify oscillations in the interference pattern, e.g., the so-called carpet structure at large angles with respect to the polarization axis [134; 135]. For smaller angles, oscillations gradually wash out due to the stronger influence of the Coulomb field on the quantum trajectories [136; 193].

where $p_{\perp}^2, p_{\parallel}^2$ are momentum coordinates, t_1 and t_2 are ionization times for interfering trajectories. The phase difference for destructive interference must satisfy:

$$\Delta S = 2\pi(n) \tag{4.2}$$

where $n = 1, 2, 3\ldots$ for odd-parity ground state. For even parity, $2n$ has to be replaced by $2n+1$ [134]. Thus, the positions of the minima in the carpet structure can be found analytically. They are distributed on a family of ellipses intersecting the $p_{\parallel} = 0$ axis [134]. Eq. 4.1 indicates that they can be parametrized by t_1 and t_2 which are the emission times of two interfering trajectories. Similar solutions could, in principle, be found for ω-2ω pulses. Mathematically, we must find solutions for t_1 and t_2 from the saddle-point approximation for the two-color vector potential. The conditions for phase-dependent constructive interference may be derived analytically. Since, in the experiment, the 2ω field is weak ($\xi < 0.1$) compared to the ω field, solutions for t_1 and t_2 might change slowly as a function of ω-2ω phase. One could thus speculate that the ellipses defined in Eq. 4.1 change their coordinates only slightly. The corresponding ionization times can be extracted from the experimental data with sub-fs precision. Hence, a ω-2ω experiment is an alternative to a two-color HHG experiment, where it was demonstrated that ionization and recollision times can be reconstructed [53].

In conclusion, we observe periodical changes in the position of interference maxima and minima at large angles with respect to the polarization axis. They are generated by two wavepackets emitted within two successive, oppositely directed laser half-cycles that

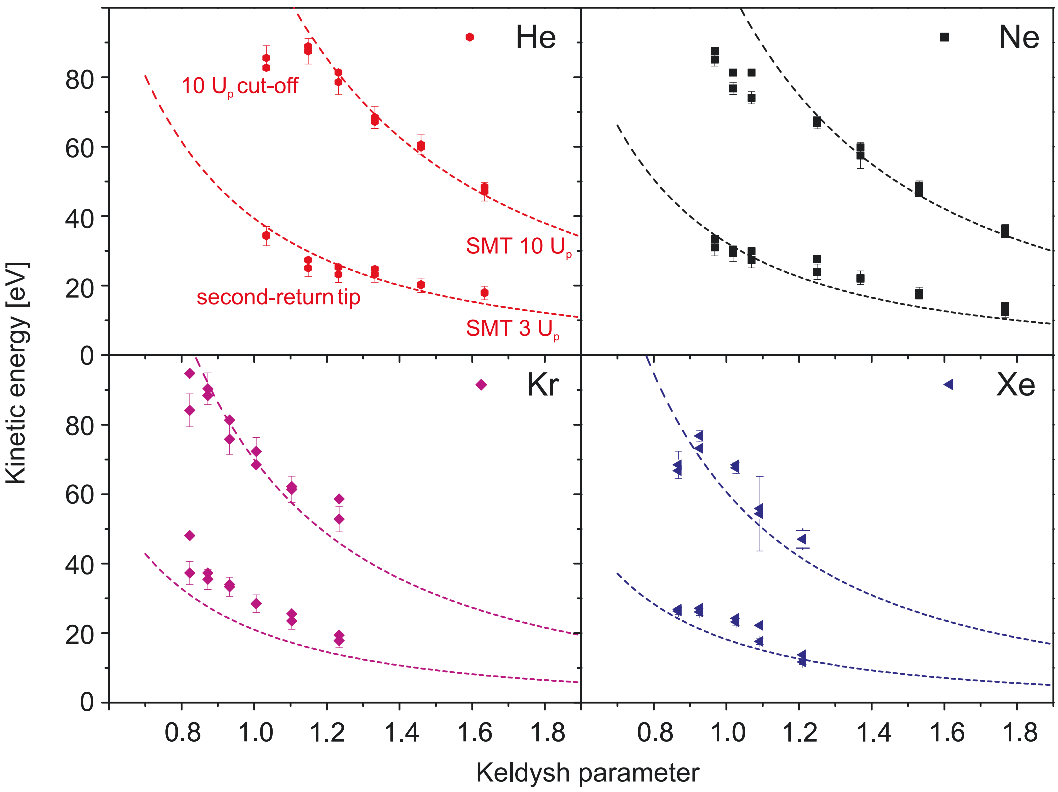

Figure 4.14: Experimental $10U_p$ cut-off and phase-flip for second-return extracted from PP spectra. Dashed lines indicate $3U_p$ and $10U_p$ calculated from the Keldysh parameter. Points below $10U_p$ identifies the ionization saturation. Good agreement between experiment and theory is obtained. Such procedure can be employed to calibrate the laser intensity. Error bars are put for points if no clear phase flip can be identified.

are barely affected by the Coulomb potential, analogous to the result of [134]. Trajectories emitted closer to the polarization axis are strongly perturbed by the ion field and contribute to holographic side-lobes [136; 193]. Oscillation in the interference pattern can potentially be reproduced by SFA and CVSFA calculations. In order to qualitatively evaluate the fine oscillation in the interference pattern, quantum orbit calculations must be performed.

4.2.4 Intensity dependencies

In Fig. 4.14 the energetic position of the $10U_p$ cut-off and $3U_p$ are plotted as function of the Keldysh parameter [159]. Note that $3U_p$ corresponds to the position of second-return tips in mometum-resolved PP. The dashed lines represent calculated functions. Values that are below the dashed lines indicate ionization saturation, i.e., all atoms in the focus are ionized before the laser intensity peak. Thus, $10U_p$ electrons are created well before the laser peak intensity and gain less energy than expected. For atoms with high ionization potentials (e.g., He and Ne) ionization saturates before $\gamma_k \leq 1$. Ionization saturation for Kr and Xe occurs at much lower values of γ_k. It is curious that He and Ne reach saturation, while Kr and Xe do not, for the same γ_k values. One should keep in mind that the Keldysh parameter describes the ratio of ionization potential and laser intensity. For a given laser intensity, targets with lower I_p, also have lower γ_k. Experimental values for the second-return tip are distributed along the $3U_p$ curves. This agreement with theory suggests that the second-rescattering process is independent on the target. This behaviour appears to be consistent with SMT, which includes no dependence on target.

A more quantitative comparison can be performed by comparing experimental PP spectra with TDSE results, as shown in Fig. 4.15. Abel-projected TDSE results are obtained for an Ar atom in the single-active electron approximation. The ionization potential was mimicked by choosing the $3p_0$ orbital and treating it as a ground state for the effective potential :

$$V(r) = -[1 + 17\exp(-2.11375r)]/r \tag{4.3}$$

For low intensity, satisfactory agreement is obtained for overall universal structures. Structures (a) and (b) appear, however, at lower momenta than in the experimental spectrum. TDSE at higher intensities shows that a part of the tip (Fig. 4.15 blue and red features) is dominated b more intense contribution (green arc-like feature). $10U_p$ cutoff at much lower momentum that expected is because of ionization saturation. The rescattering signal in RPC shows a characteristic angular pattern that is very well reproduced by TDSE. However, in the experimental RPC, the low momentum region of spectrum resembles a 'lobster-tail' structure in both cases. In TDSE, this structure is more concentrated along the laser polarization axis.

4.2.5 Target dependencies

PP and RPC spectra strongly enhance target-dependent features as shown in Figs. 4.4 and 4.10. Both the ground state configuration and the scattering potential are important in ionization and rescattering dynamics. In order to quantify the influence of the ground state on TDSE, calculations have been performed for Ar atom with 1s and 3p ground state configurations. Fig. 2.8 demonstrates the strong PP and RPC signal dependence on the ground state configuration. For 1s, PP shows an extended and broadened tip feature and the RPC signal is distributed in narrow cone along the laser polarization axis with characteristic side lobes. The rescattering region of the spectra displays a characteristic minimum in the angular signal distribution. Emission from the 3p ground state results in a fan-like pattern in PP, and a characteristic nodes in angular distribution for rescattered

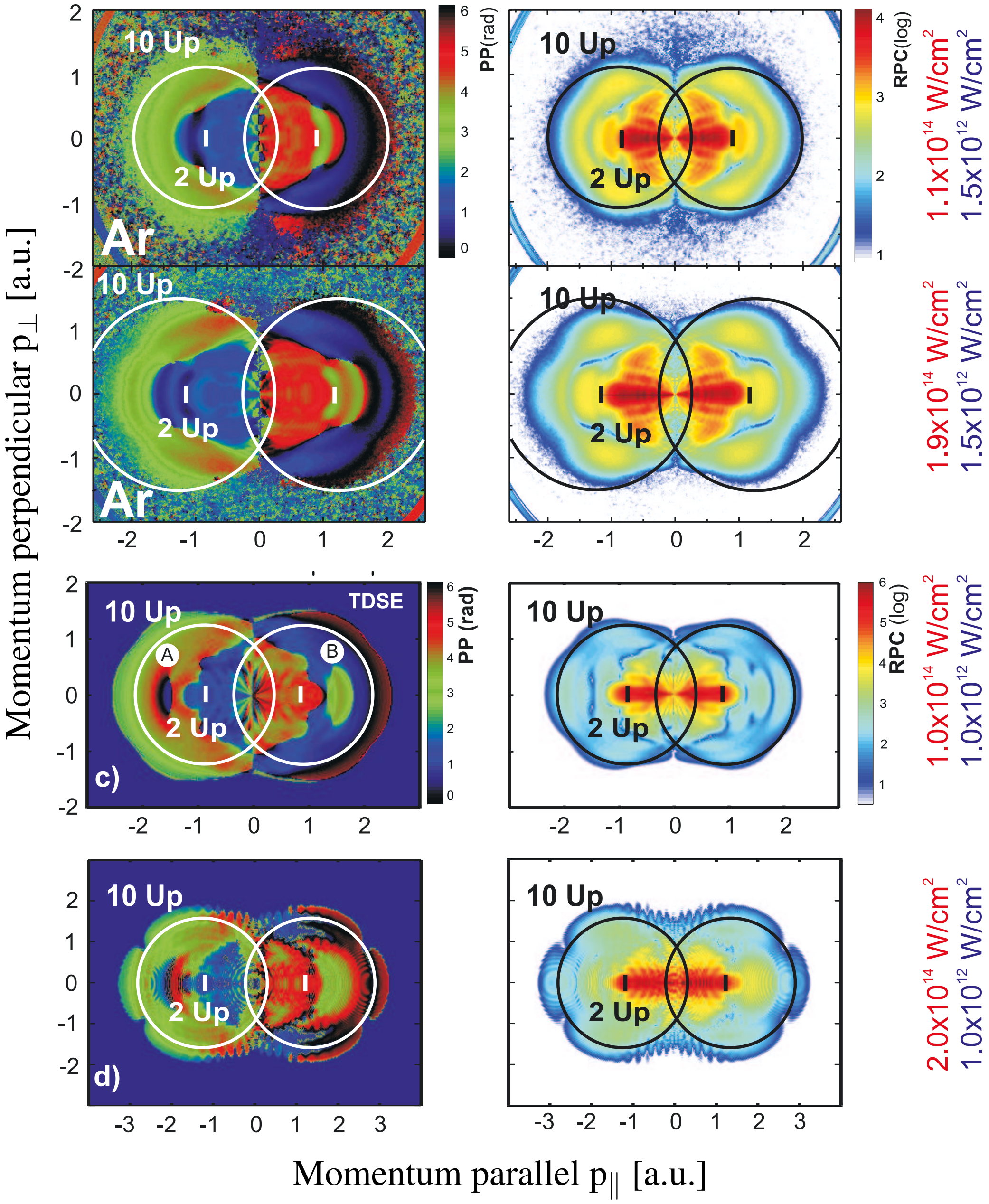

Figure 4.15: PP (left) and RPC (right) spectra obtained in experiment on Ar (a,b) and TDSE (c,d) for similar intensities. Note the different dynamic range in TDSE (6 orders of magnitude) compared to the experimental result (4 orders of magnitude). Fine structure in TDSE is not reproduced by the experiment. TDSE calculations performed by M. Arbeiter.

electrons. Differences can be resolved in RPC with higher contrast.
To compare emission from 1s and 3p ground state configuration, experimental He and

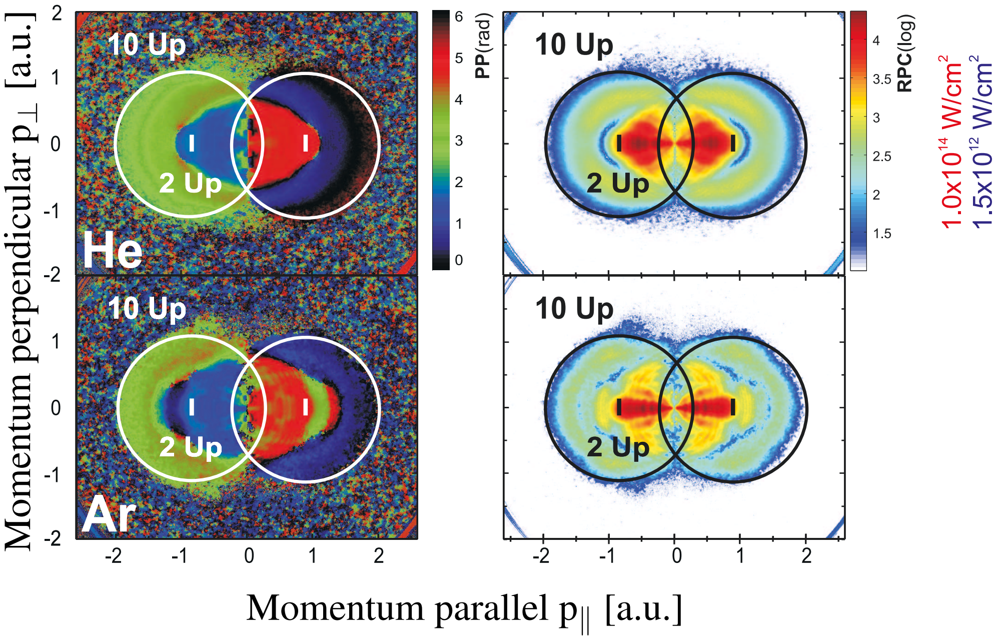

Figure 4.16: PP and RPC spectra resulting from ionization of He and Ar with ω-2ω pulses with two different intensities. Note that ionization originates from 1s (He) and 3p (Ar). Influence of a ground state on PP and RPC spectra cannot be disentangled by analogy to TDSE spectra Fig 2.8 due to influence of scattering center which is evident from TDSE calculations.

Ar PP and RPC are shown in Fig. 4.16 for similar laser intensities. We resolve a characteristic minimum in rescattering RPC along laser polarization direction and characteristic nodes in PP and RPC angular distribution for Ar in agreement with TDSE solutions. Contrast of spectral features in PP and RPC is, however, much weaker than the TDSE predicts. Surprisingly, tip feature in PP experimental spectrum from He is much smaller than in TDSE. One should note, however, than scattering center is TDSE is different than in the experiment. Additional calculation for He in 1s ground state could clarify this discrepancies.

In general, discrepancies can be attributed to idealized laser conditions, which assume shorter pulses (60 fs, vs. 120 fs in the experiment). In addition, the Gaussian intensity distribution in the focus is not taken into account. On the other hand, the TDSE is solved for the SAE approximation which neglects multielectron dynamics and scattering from a realistic potential. In conclusion, the success of PP and RPC implies that *PoP* spectroscopy is a sensitive tool that enables us to identify contributions originating from e.g. wavepacket spreading, first and second returns, wavepacket interference. When applied to other systems it can be applied to study a wide variety of effects.

5 Application of $\omega/2\omega$

In this chapter, we present results of ω-2ω ionization of molecular targets. Comparison between N_2, CO_2 and the reference spectrum (Ar) reveals common features that are fingerprints of the first and second return scattering. C_{60} is presented as an example of a system with a large number of degrees of freedom. We wish to emphasize that thermal and statistical ionization dominate the excitation when relatively long pulses (100 fs) are applied. Finally, we present *in situ* measurement of the Gouy phase shift of ω-2ω in the focus volume.

5.1 Molecule ionization

Experiments on ionization of small linear molecules are performed by using ω-2ω pulses. In analogy to the results presented in the previous chapter, a 2ω field introduces only a small perturbation, so the dynamics is driven by the ω field. Electronic structure of systems such as CO_2 or N_2 is not significantly more complex, compared to the structure of atoms. The highest-occupied molecular orbitals (HOMOs) for N_2 and CO_2 have (σ_g) and (π_g) symmetry, respectively [194]. In contrast to atoms, molecules possess additional rotational degrees of freedom, which introduce an orientation dependent ionization probability. For CO_2, it peaks at 45° with respect to the molecular axis, while for N_2 it is distributed around 0° [195]. Both systems are typically used as a benchmark to reconstruct the molecular orbitals from HHG spectra [196; 197; 198], and to test HHG itself. With our experiment we address the question: Is the scattering dynamics similar to those of atoms even though the ionization rate is orientation-dependent ?

We perform experiments under similar conditions to those we used for atoms. Fig. 5.1 shows spectra resulting from two-color field ionization of randomly oriented N_2 and CO_2. A reference signal from Ar is recorded for sake of comparison. PP and RPC spectra for both molecular systems very much resemble results from Ar. In particular, the club structure with a characteristic $10U_p$ cut-off and a tip exceeding $2U_p$. The phase relation in PP is nearly the same as for the rare gases. Detailed inspection of PP and RPC spectra reveals some fine differences especially in the low momentum range. Most distinct is an arc-like feature at the $2U_p$ ($p_z = 1$) region of the PP signal for N_2 and Ar. Note that this signature is not present for CO_2. The structure corresponding to the second return for N_2 and Ar is more rounded than for CO_2. More details can be resolved in

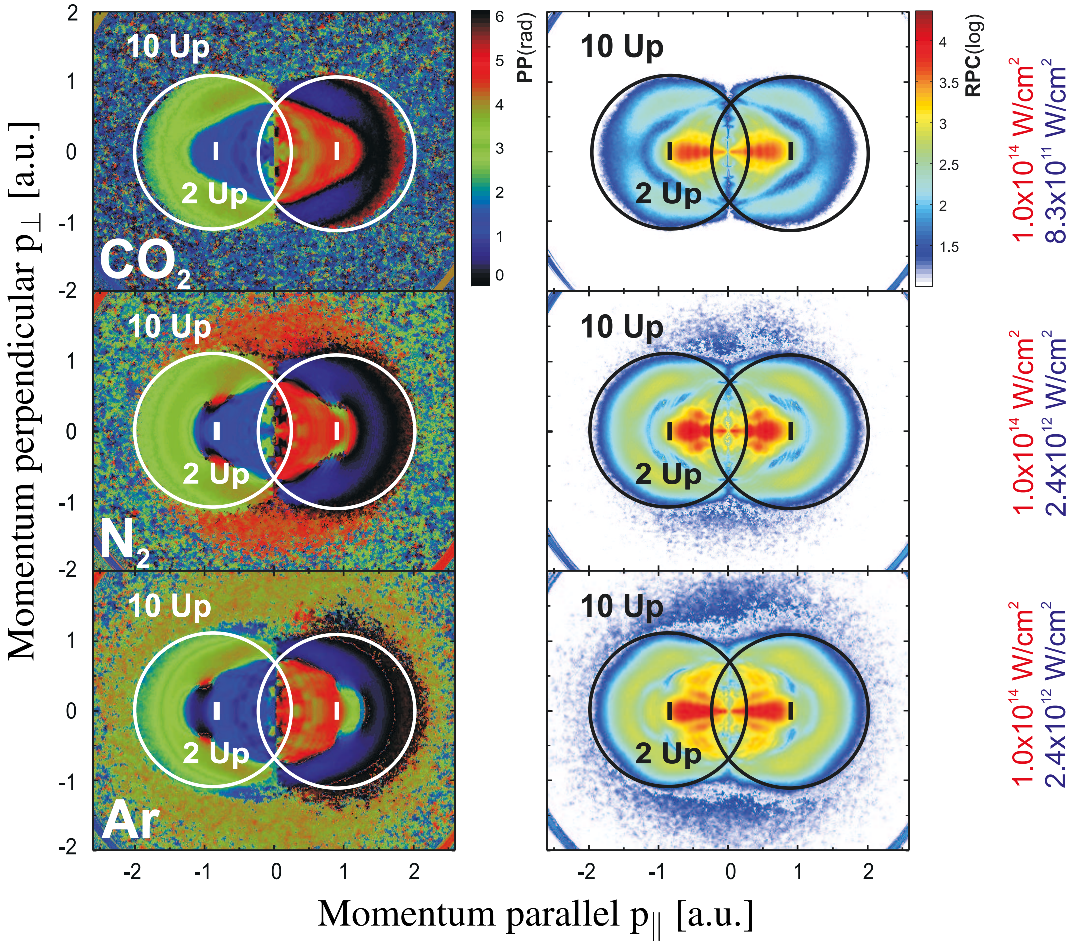

Figure 5.1: Comparison of PP (left) and RPC (right) spectra for Ar with randomly oriented CO_2 (a) and N_2 (b) molecules ionized with ω-2ω pulses. Characteristic club-structures are obtained for both atomic and molecular systems, and result from electrons scattering during first return. A tip feature that extends beyond the $E_{kin} = 2U_p$ cut-off corresponds to electrons that scatter during the second return. $E_{kin} = 10U_p$ and $E_{kin} = 2U_p$ cut-offs are labeled.

the low momentum part of the RPC spectra. For molecules the momenta of very high RPC are oriented along the laser polarization axis whereas for Ar it is distributed over larger angle. The CO_2 RPC spectrum resembles those from He or Ne, (Fig. 4.4). Two side lobes emerge in RPC for N_2, and the signal along the laser polarization axis shows more fine details. The $10U_p$ ridge exhibits a characteristic target-specific angular distribution. Since analysing target-dependent features requires a sophisticated quantum model, in the following discussion we concentrate only on comparing PP spectra with the prediction of SMT. Target-dependent features are analysed only qualitatively.

PP signals extracted along the laser polarization axis for N_2, CO_2, Ar and the refined

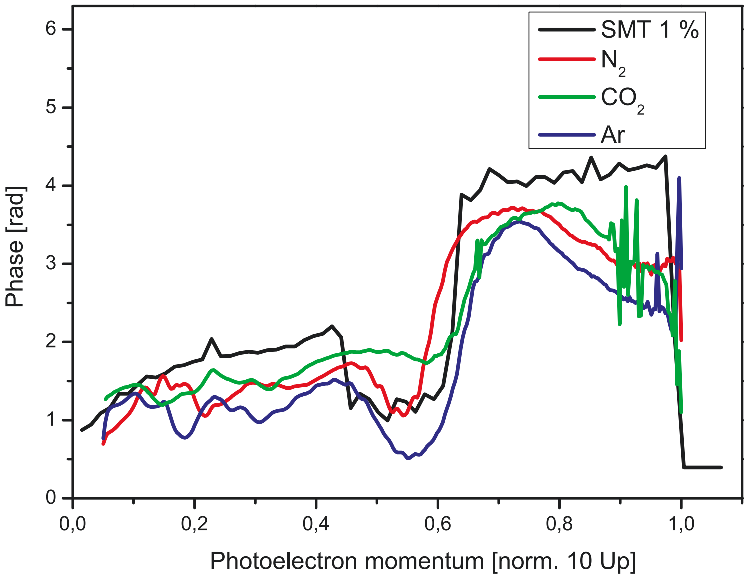

Figure 5.2: PP extracted along the laser polarization axis for N_2 (red) and CO_2 (green) are in good agreement with results for Ar (blue) and the refined SMT model (black). Similar relative phase courses underline the importance of wavepacket spreading and DSC. Both the experiments and the calculations are performed with $\xi = 0.1$.

SMT model are shown in Fig. 5.2. Molecular spectra are found to be very similar to the Ar signal, obtained under comparable laser parameters. A characteristic phase jump at $p_{norm} = 0.6\,\mathrm{a.u.}$ ($E_{kin} \approx 3U_p$) is preceded by a small dip in the spectrum. The good agreement with the refined model and with the reference Ar signal underlines the importance of wavepacket dispersion and the first and second return in the ionization in small molecules. Thus, our experiments confirm the universal character of the scattering dynamics as presented in previous chapter.

PP spectra from molecules provide insight into oscillations in the interference pattern at large angles with respect to the polarization axis. In the previous chapter, we discussed analogous observations for atomic targets. The interference between wavepackets is sensitive to the ω-2ω phase, which controls the ionization and the rescattering times. Two important conclusions can be derived from the presence of this interference in a small molecular target. First, the Coulomb field does not significantly influence the relevant trajectories. Second, this interference can be employed as precise timing tool, since it reflects the phase accumulated during propagation. In contrast to atomic targets, in the molecules the wavepackets can be emitted from two atomic centres separated in space. Such spatial offsets modify accumulated phase. Thus, a detailed comparison with atomic systems could provide information about spatial offsets and enable retrieving e.g., a bond length from molecular data.

Photoelectrons rescattering in the backward direction contain a wealth of information about both the electronic structure and the scattering dynamics, as shown in recent studies [125; 199; 200; 201; 202]. Thus, *𝒫o𝒫* spectroscopy on aligned molecules could provide more insight into a scattering center or the elastic scattering cross-section. For instance, Ar and N_2 have very similar ionization potentials (15.76 eV and 15.58 eV, respectively [203]). The tunnelling process should be very similar in both cases if one neglects the spatial offset of atomic centres in the molecule. Thus, the electronic structure is one primary factor that influences the rescattering dynamics [204]. The corresponding PP spectra are very similar, down to small details (e.g., the red arc feature at $2U_p$). RPC, however, reveals more target-specific features, such as the angular distribution of the $10U_p$ ridge, or enhanced signal at large angles and low momenta for Ar.
Potentially, a deconvolution of the dynamical system response may reveal interesting aspects of multielectron dynamics, or coupling between energy levels in molecules. For example, charge resonance enhanced ionization (CREI) depends on the pulse length [205]. One could imagine a *𝒫o𝒫* experiment conducted on CO_2 with a different pulse length. By comparing data in experimental conditions with suppressed CREI, one could reveal signatures that characterize such process. However, the assignment of particular spectral features requires sophisticated quantum models to be compared with experimental data. SFA-based models or quantum dynamics would be an alternative for time-consuming TDSE calculations.

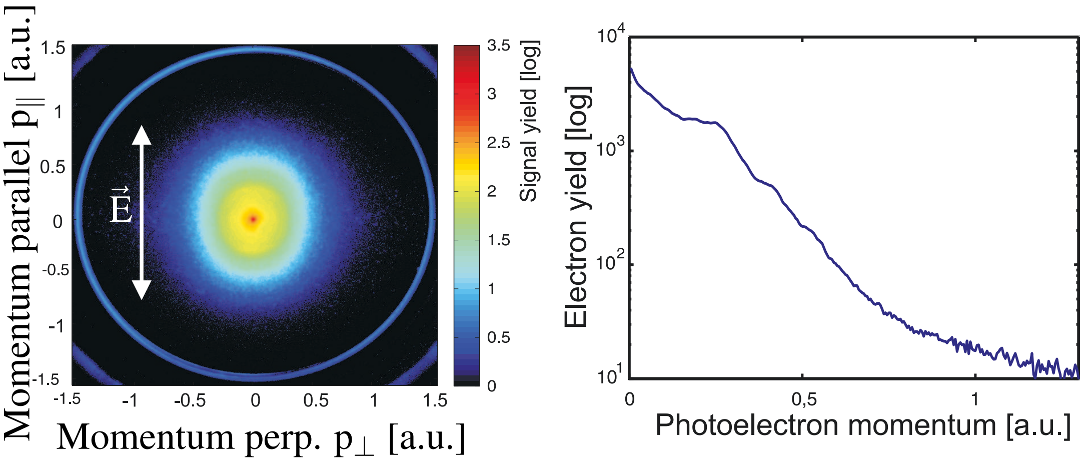

Figure 5.3: Momentum-resolved photoelectrons spectrum (left) from C_{60} molecule ionized with ω-2ω laser pulses with $I_\omega = 1 \cdot 10^{13}$ W/cm^2 and intensity ratio $I_{2\omega}/I_\omega \approx 0.05$ and a relative phase $\phi = 0$. The corresponding photoelectron momentum spectrum along the laser polarization axis (right) shows thermal electron emission (with an exponential decrease of electron yield [209]. The laser polarization direction is indicated by arrow.

5.2 Ionization of C_{60} with ω-2ω pulses

We perform experiments on fullerene molecules to investigate whether $\mathcal{P}o\mathcal{P}$ can control photoelectron emission in large molecular system. The photoelectron spectra of C_{60} are known to exhibit strong contribution of thermionic ionization [206; 207]. We demonstrate that with $\mathcal{P}o\mathcal{P}$ those can be well discriminated on favour of, e.g., ATI signals. Moreover, it is interesting to test systems in a multiphoton ionization range, in view of our recent studies on ionization of C60 with CEP pulses in the tunneling range [208]. An effusive molecular beam was created by evaporation of high-purity C_{60} powder from a resistively heated oven. Typically, temperatures of ≅420 °C are needed to obtain a reasonable signal in the VMI. The temperature is controlled by a thermocouple (K-typ) which is in contact with the outer side of the powder cartridge. The effusive beam is collimated by two irises with apertures of 2 mm. Additionally, two blades mounted on manipulators enables precise adjustment of the beam and avoid contamination of the vacuum chamber due to extensive powder dissemination.

Fig. 5.3 (left) displays a typical angle-resolved photoelectron spectrum resulting from C_{60} ionization. The signal is dominated by a thermal contribution, which can be identified by its isotropically distributed signal. Such behaviour is typical for pulses longer than 100 fs [210]. Thermal contributions arise from the extensive heating of the molecule [207; 209] due to the population of the so-called Doorway state (LUMO-1) which

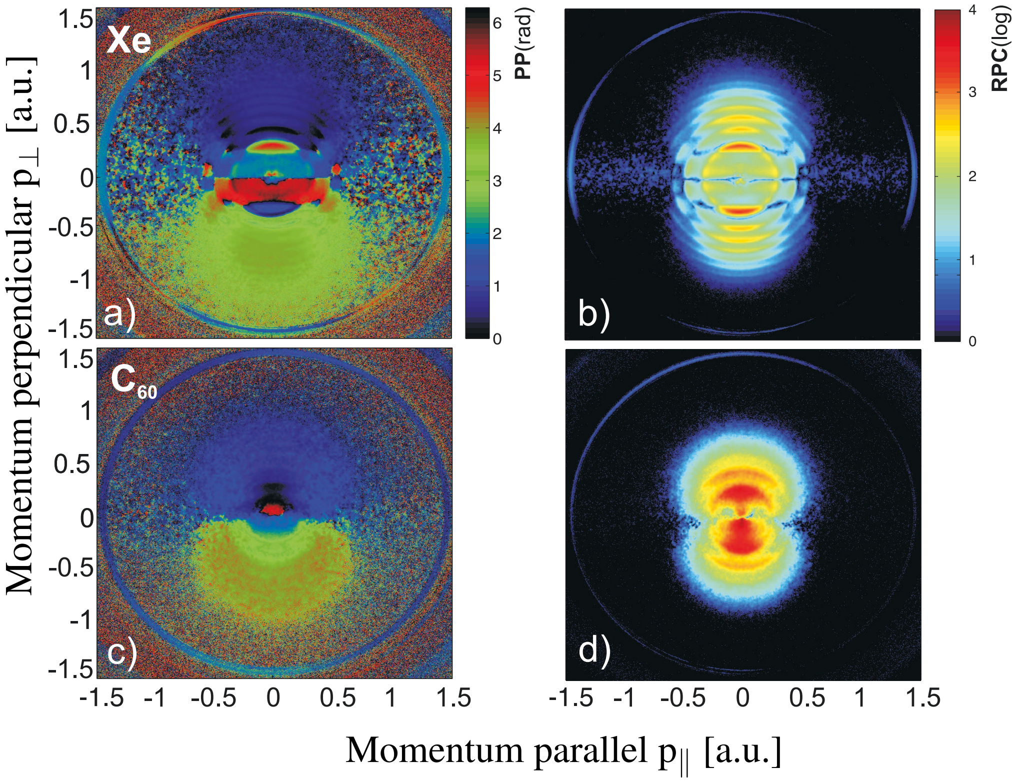

Figure 5.4: PP (left) and RPC (right) spectra resulting from ionization of Xe (a,b) and C_{60} (c,d) with two-color laser pulses. The fundamental laser intensity $I_\omega = 1 \cdot 10^{13}$ W/cm^2 drives ionization into the multiphoton range resulting in an intense ATI structure (b). The SHG component with intensity $I_{2\omega} = 5 \cdot 10^{11}$ W/cm^2 introduces weak perturbation to the process. PP shows similar phase dependencies (a,c). RPC from C_{60} reveals ATI-like features, with signal enhanced along a laser polarization axis. Note that ATI cannot be resolved in Fig. 5.3 due to an extensive thermal ionization signal.

creates a kind of thermal sink where an extensive amount of energy can be stored [206; 211]. The only fingerprint of multiphoton transition is a single ring at about $p = 0.25$ a.u. which corresponds to $E_{kin} = 1\,\text{eV}$ for present VMI settings. A peak emerges at position of the first ATI peak [212; 213], on top of which a signal from many Rydberg states can be typically found [206; 211]. Recently, it was demonstrated that super-atomic molecular orbital (SAMO) states contribute in the same energy range [210; 214; 215]. In order to discriminate thermal contributions we utilize $\mathcal{P}o\mathcal{P}$ to analyse multiphoton ionization in C_{60}. As a reference, atomic Xe is ionized with the same laser conditions.

In Fig. 5.4 PP (left) and RPC (right) spectra resulting from Xe (a,b) and C_{60} (c,d) are presented. Characteristic ATI rings and lack of the holographic side lobes in RPC from Xe (b) indicate that the system is probed in the multiphoton ionization range.

PP reaveals two regions with isotropically distributed phase signal for both Xe (a) and C_{60} (c). SFA calculations performed in the MPI range reveal a similar phase contrast [216]. Small discrepancies from a monotonical PP course can only be resolved at the low momenta. The RPC spectra exhibit characteristic rings that appear at the ATI peak positions. The rich angular pattern resolved in RPC for Xe indicates that maxima and minima in the angular distribution change their position. For C_{60} broadened rings with signal enhanced along the laser polarization direction correspond to the ATI peaks. Due to the ionization mechanism both PP and RPC differ substantially from spectra presented in Chapter 4. Systems are probed in the multiphoton ionization range and features characteristic for rescattering e.g., club structure are not present in PP.

This experiment demonstrates that the directional photoemission from a large system like C_{60} can be realized in the MPI range by sculpted two-color fields. Furthermore, $\mathcal{P}o\mathcal{P}$ enables us to discriminate thermal contributions. We note that thermal signal suppression has recently been reported for SiO_2 nanoparticles excited with CEP pulses [188; 189]. The RPC signal strongly enhances ATI contributions in C_{60}, which are typically dominated by thermal contributions. PP reveals characteristic phase dependence which is similar for both systems. Finally, interesting phase behaviour for region where Rydberg levels and SAMO contribute is resolved and will be studied in future.

5.3 Gouy phase shift

The phenomenon of the Gouy phase shift in focused laser beams can be demonstrated with a ω-2ω experiment. As presented in chapter 1.5 focused laser beam experience phase slip as it travels through the focus volume. For this experiment, we must perform *in situ* measurement of the phase slip along the focus area. Generally, VMI can be operated in two ways: velocity-map imaging mode and spatial imaging mode as shown in chapter 3. In the latter mode, direct projection of the focus area on the 2D position sensitive detector can be realized. In the experiment, a Ti:Sapphire laser output ($I_\omega = 1.3\cdot 10^{14}$ W/cm^2, $I_{2\omega} = 7.7\cdot 10^{12}$ W/cm^2 130fs, 1 kHz) generates the ω-2ω laser pulses. They are focused into the VMI chamber by a spherical mirror (f=300 mm). The phase dependent photoemission is measured as described in Chapter 4. Briefly, the spatial imaging spectra are recorded for different time-lags between ω-2ω fields. A scan interval of $\varphi = 3\pi$ is chosen and split into 200 motor steps. The photoelectrons released by tunnel ionization from Xe are projected onto the position-sensitive detector. In order to quantify the relevant energy range of electrons projected onto detector, SIMION calculations were performed. Most of the information about the kinetic energies of the electron is lost. Low-energy electrons ($E_{kin} < 0.1\, eV$) primarily contribute in the direction of the laser propagation, see Fig. More energetic electrons are projected into the detector area offset from the central line, and are not taken into consideration.

Both component of the ω-2ω electric field experience the Gouy phase shift, which depends on the position within the focus. The electric field of the ω-2ω pulse can be written as:

$$E(t,z) = E_0(sin(\omega t + \varphi^{Gouy}_{793\,nm}(z)) + \xi sin(2\omega t + \varphi_{rel} + \varphi^{Gouy}_{397\,nm}(z))) \qquad (5.1)$$

where E_0 is the electric field amplitude, φ_{ref} is the relative phase between the ω and 2ω fields and φ^{Gouy} is the Gouy phase shift. This situation is schematically depicted in Fig. 5.5. The Gouy phase shift modulates the relative phase of the ω-2ω laser pulse that for sake of analysis, is assumed to have a spherical wavefront (for details see [145]). The tunnelling probability (green) is calculated for the Landau rate [152], and shows a clear dependence on position. Since it scales as $exp(-2/3E(t,z))$, the total electron yield in particular sections of the laser focus should be dependent on a total phase. It should be noted that the absolute ionization rate is not determined in the experiment.

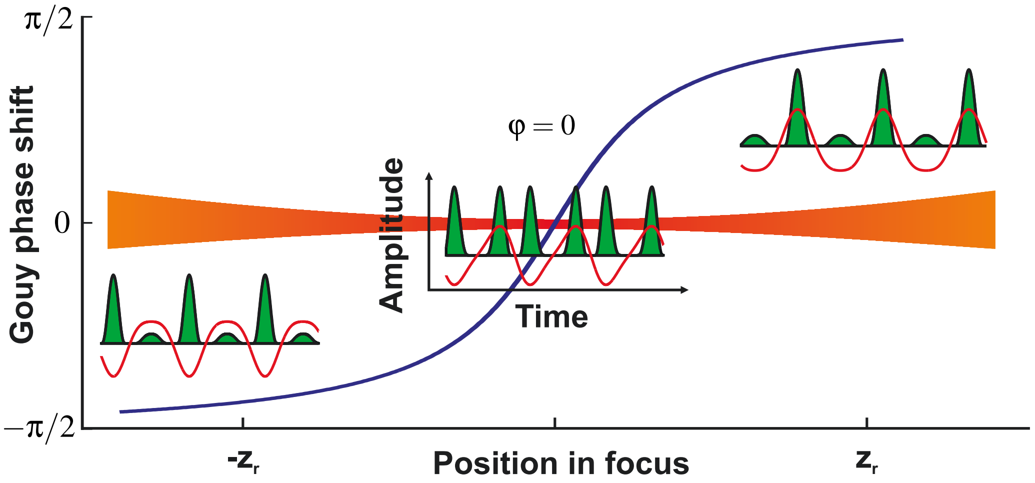

Figure 5.5: Schematic representation of the Gouy phase shift for a focused two-color laser beam. In this illustration, the electric field (red) and ionization rate (Eq. 2.1, (green)) depends on the position in the focus. Calculations are performed for $\xi = 0.1$ and focus-center phase $\varphi_{rel}(z = 0) = \pi$. The relative phase slips by π when the beams travels from $-z_r$ to z_r, where z_r is the Rayleigh length.

The electron yield along the laser propagation axis, averaged over an angular section 2° wide is shown in Fig. 5.6 (blue). The phase dependence can readily be resolved around the central minimum, which stems from the beam waist where the ionization volume is minimal. The Gaussian distribution (Eq. 5.2) with FWHM = 5 mm is plotted as a reference (green).

$$f(x) = exp\left(-\frac{(x - x_c)^2}{2\sigma^2} \right) \tag{5.2}$$

The $\mathcal{PoP}$ technique is employed to analyse the relative photoelectron signal oscillation in the spectra. PP and the RPC spectra retrieved from the focal area of the ω-2ω pulse are shown in Fig. 5.7. PP reveals a clear phase slip which can be identified along the laser focus area, which is represented with white contour lines. RPC shows that the strongest contrast appears along the laser propagation axis. Phase-dependent signals that can be resolved away from the focus area are not considered in determining the Gouy phase shift: this part of the spectrum stems from energetic electrons hitting the detector.

The PP dependency along the laser polarization axis extracted from Fig 5.7 is plotted in Fig. 5.8 (blue). In order to quantify this dependency we derive an equation for φ_{total} that modulates the photoelectron yield along the laser polarization axis [217]. Consider the

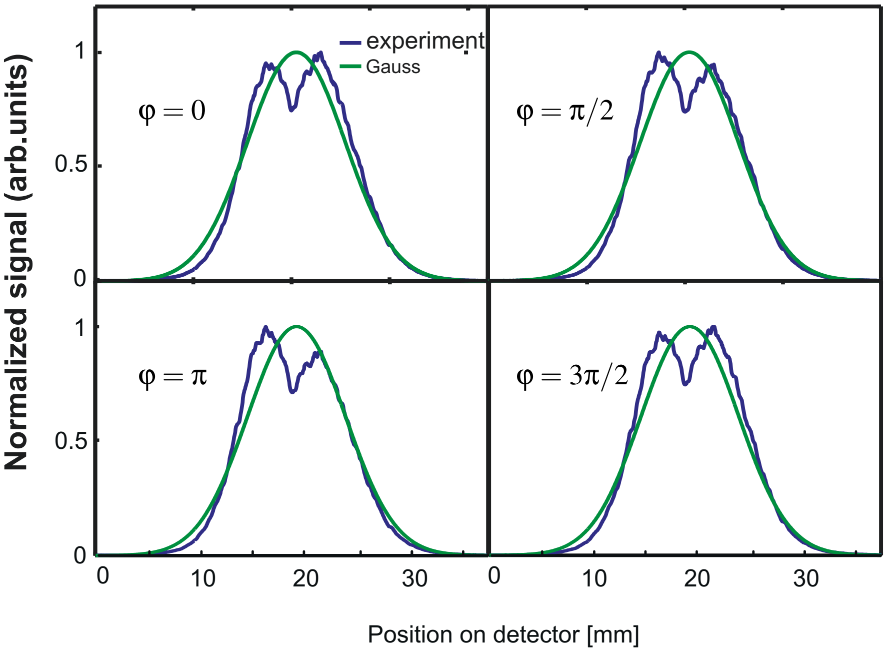

Figure 5.6: Photoelectron signal yield (blue), extracted along a focal volume for different relative phases ϕ. Clear phase dependencies in the signal are due to the Gouy phase shift in the focused laser beam. A Gaussian distribution (green) is plotted for reference.

sine terms from Eq. 5.1:

$$sin(\omega t + \varphi_{793\,nm}^{Gouy}(z)) + \xi\, sin(2\omega t + \varphi_{rel} + \varphi_{397\,nm}^{Gouy}(z)) \tag{5.3}$$

The argument of the first term can be written as $\omega t' = \omega t + \varphi_{793\,nm}^{Gouy}(z)$. By substituting $t = t' - \varphi_{793\,nm}^{Gouy}(z)$, the electric field is expressed as:

$$sin(\omega t') + sin(2\omega t' - 2\varphi_{793\,nm}^{Gouy}(z) + \varphi_{397\,nm}^{Gouy}(z) + \varphi_{rel}) \tag{5.4}$$

At this point, only the 2ω field is phase dependent. Thus, the total phase is:

$$\varphi_{total} = -2\varphi_{793\,nm}^{Gouy}(z) + \varphi_{397\,nm}^{Gouy}(z) + \varphi_{rel} \tag{5.5}$$

The SHG process scales as the second power of the electric field. Therefore the laser beam diameter $d_{2\omega} = d_{\omega}/\sqrt{2}$ [47]. One can show that the Rayleigh parameters for both frequency components are equal:

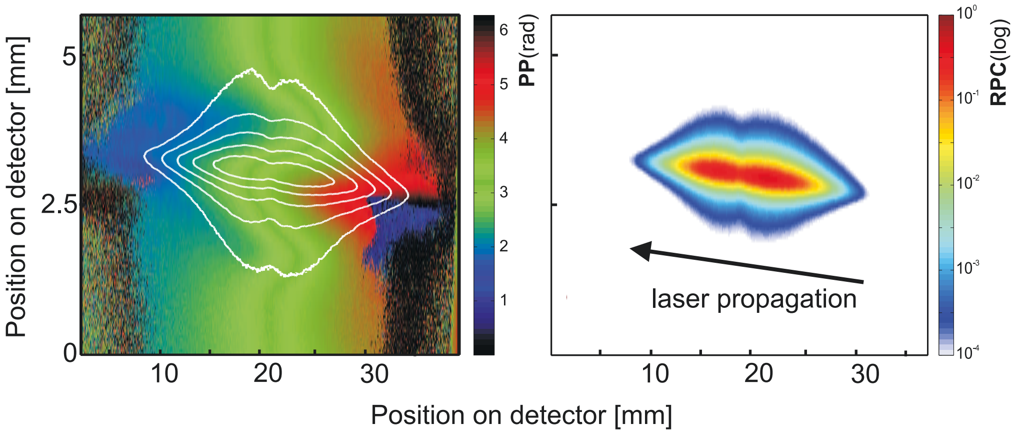

Figure 5.7: PP (left) and RPC (right), extracted from photoelectron signal released from a focal volume of a ω-2ω pulse. Note that a spatial imaging mode is applied, which enables direct visualisation of the focal volume. Results of RPC are overlaid in PP to illustrate the position of the focus volume. A clear phase slip can be resolved along the smallest contour line. Phase information is extracted from PP by integration of the phase signal over an angular section of 2° width, and is depicted in Fig. 5.8.. The laser propagation direction is indicated by arrow.

$$z_{r\omega} = \frac{\pi w_{0_\omega}}{\lambda_\omega} = \frac{\pi\lambda_\omega^2}{\lambda_\omega D_\omega^2} = \frac{\pi\lambda_\omega}{D_\omega^2} = \frac{\pi\lambda_{2\omega}/2}{D_{2\omega}^2/2} = \frac{\pi\lambda_{2\omega}}{D_{2\omega}^2} = z_{r2\omega} \tag{5.6}$$

which implies that the Gouy shift for both components are equal:

$$\varphi_{793\,nm}^{Gouy}(z) = \varphi_{397\,nm}^{Gouy}(z) \tag{5.7}$$

Substituting this into Eq. 5.5 indicates that the phase measured in the experiment is:

$$\varphi_{total} = \varphi_{rel} - \varphi_{793\,nm}^{Gouy}(z) \tag{5.8}$$

The relative phase which is independent of z, is modulated by the Gouy phase. Since the ionization rate is dependent on the electric field of the laser pulse, Eq. 2.1 [152], the Gouy phase can directly be measured by means of the direct electron yield along the laser propagation direction. In Fig. 5.8, we show a comparison of the calculation with the outcome of the experiment. Very good quantitative agreement is achieved within the Rayleigh range ($z_r = 2.1\,\mathrm{mm}$). For $z > z_r$, however, the measured phase shift deviates from the prediction of Eq. 5.8 but deviates quite symmetrically. One should note that Eq. 5.8 neglects φ_{rel} dependence on the position within the focus. Obviously, it

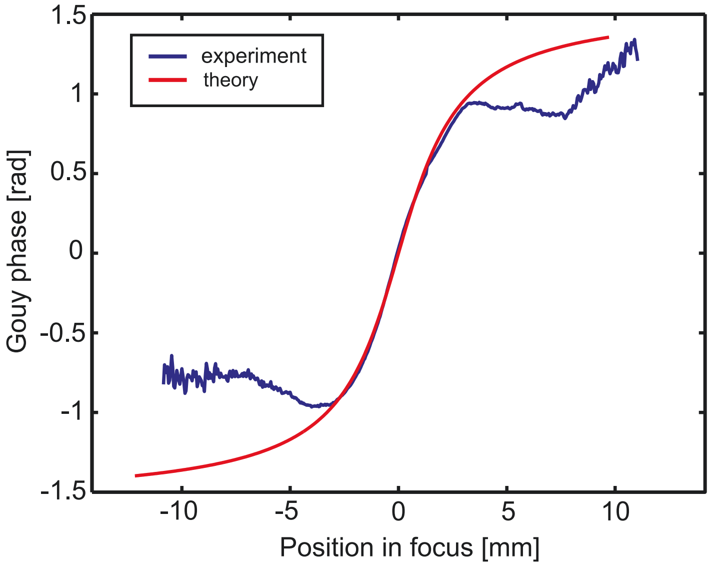

Figure 5.8: Comparison of the experimentally measured Gouy phase shift obtained from the PP spectrum in Fig. 5.7 (blue) and the prediction of Gouy theory calculated for $\lambda = 793\,\text{nm}$ and Rayleigh length $z_r = 2.1\,\text{mm}$. Good qualitative agreement is obtained within the range where tunnel ionization dominates ($z = \pm 3$). In the outer region interplay between multiphoton ionization and tunnelling leads to deviation from theory.

is valid only if the tunnelling ionization occurs along projected part of the laser focus. Otherwise, φ_{rel} influences other ionization processes, e.g., REMPI. Beyond $z = 2.8\,\text{mm}$ where the laser intensity drops below $5.6 \cdot 10^{13}\,\text{W/cm}^2$ the Gouy phase shift signal levels out. In this intermediate range electrons are released by both multiphoton and tunnelling mechanism. Hence at least in the optical tunnelling regime, the Gouy phase shift can clearly be identified with $\mathcal{PoP}$. As a possible application, electron acceleration in a vacuum by Gouy-phase-induced interference in a focused laser volume can be considered. It has been demonstrated theoretically that two-color co-propagating circularly polarized laser field can effectively accelerate electrons [218]. $\mathcal{PoP}$ could potentially be used for *in situ* characterisation of Gouy phase in a focused laser beam.

Conclusions and Outlook

I have presented studies of momentum-resolved photoemission from atoms, molecules, and fullerenes ionized by intense sculpted two-color fs laser pulses. By introducing a weak perturbation in the form of a second-harmonic (2ω), and controlling its relative time delay with respect to the fundamental field (ω) with sub-fs precision, ionization and rescattering times can be tuned. Phase-of-the-phase spectroscopy ($\mathcal{PoP}$) is introduced and utilized to characterize electron yield oscillations in momentum-resolved spectra. Moreover, I have shown that $\mathcal{PoP}$ enables to discriminate thermal and statistical contributions, and to enhance ATI features. $\mathcal{PoP}$ quantifies the phase-dependent signal oscillations in terms of relative phase contrast (RPC) and phase-of-the-phase (PP), describing how much the signal oscillates, and with which time lag in respect to the relative phase of ω-2ω laser field.

I described a refined simple man's theory (SMT) that enables to model the influence of both the wavepacket spreading and differential scattering cross-section (DSC) on the rescattering dynamics. To the best of our knowledge, this work for the first time employs SMT to study momentum resolved photoemission in ω-2ω fields. PP enables to unambiguously distinguish electrons that rescatter during the first and second returns from the parent ion. First-return scattering is favoured by wavepacket dispersion, and creates characteristic club-like regions in PP with phase offsets of $\varphi = \pi$. Second-return contributions are favoured by the differential scattering cross-section (DSC) and form circular patterns extending beyond the classical $2U_p$ cut-off. Moreover, DSC modifies phase dependencies for the first return, which explains the smaller phase offset in PP between contributions from successive laser cycles. Accompanying TDSE calculations confirm our experimental findings, and the outcome of SMT modelling.

RPC significantly enhances target-dependent features in photoelectron spectra. For He and Ne, the RPC signal forms a fan-like pattern at a low momentum range. In contrast, for other gases the signal is enhanced at higher angles relative to the laser polarization axis. Finally, target dependencies show up at high momentum.

Characteristic maxima, resolved at large emission angles with respect to the laser polarization axis, result from interference between electron wavepackets released in opposite directions, and are not affected by the Coulomb potential. Their angular coordinates depend on a relative ω-2ω phase. There is evidence that the ω-2ω field modulates ionization times and, as a result, the phase that particular wavepackets accumulate as they propagate. Modulations in the positions of interference maxima reflect changes in the accumulated phase.

Our first applications of $\mathcal{P}o\mathcal{P}$ spectroscopy to signals from small molecules reveals similar rescattering features to those reported for rare gas atoms. RPC spectra show target dependencies, which can only be analysed qualitatively. Multiphoton ionization of C_{60} proves that directional photoemission can be realized in a large system with many degrees of freedom. Finally, *in situ* measurements of the Gouy phase shift have been demonstrated by employing VMI in spatial imaging mode. We found that the experimental phase shift within the Rayleigh range shows good agreement with Gouy theory for a Gaussian beam with a spherical wavefront. However, at larger distances from the focus center the laser intensity level drops into a range where both MPI and tunnel ionization contributes, which leads to significant deviations from the expected phase behaviour.

Outlook

The $\mathcal{P}o\mathcal{P}$ method is not restricted to rare gases, but could be extended to study electron rescattering in other systems such as alkali atoms, molecules, clusters and even nanostructures. In principle questions could be address not only about the nature of the rescattering process but also about the dynamics of transient systems.

Although I report on the universal patterns in PP spectra from rare gases and small molecules, the influence of the scattering potential and the ground state configuration is still undiscovered. In order to test the influence of the ground state on PP and RPC, atomic hydrogen could be measured. This will allow to switch-off core polarisability effects. In principle, the system under study could be prepared in an excited state using, e.g., optical pumping. Thus, PP and RPC spectra would be influenced only by the parity of the state from which the emission occurs. Analogously, spectra from rare gases could be compared with emission from excited states of hydrogen ionized. He and Ne could be prepared in 3p, 4p and 5p and compared with other gases.

Experiments on aligned molecules could reveal further details on the influence of a molecular orbital and a scattering potential on rescattering dynamics in multielectron systems. This raises the interesting question of how large a molecular system must be to smear out the effects of a rescattering process based on the three-step model. This question can be investigated by systematically increasing the molecular size, for instance, by utilizing hydrocarbons. Other interesting aspects of rescattering could potentially be investigated, for instance the influence of Coulomb explosion. Finally, a *PoP* experiment on a jellium-type system (i.e. a system with delocalized electrons) could uncover aspects of rescattering from a softened potential.

The ionization dynamics of clusters embedded in helium droplets is one of the active research area in our group [219; 220; 221]. Experimental as well as theoretical work has shown that, due to Pauli repulsion, electrons are expelled from the helium environment [222]. Details of this process could be studied by embedding a single noble gas atom and performing of *PoP* experiments similar to those presented in Chapter 4. SMT theory predicts that the excursion and final momentum of an electron is uniquely determined by the ionization and rescattering times. Thus, the way in which helium influences rescattering trajectories could reveal a wealth of information about the interaction of an electron in proximity to a (superfluid) environment.

The Buckminster fullerene (C_{60}) molecule could serve as a benchmark system, where the transient electron dynamics significantly influence the ionization process. The transient population of the LUMO-1 state influences the population of Rydberg levels, ionization, and fragmentation [206]. Following this idea, a pump-probe experiment where a ω-2ω pulse probes the time evolution of a highly excited system could be performed. The existence of super-atomic molecular orbitals (SAMO) has been reported [210]. *PoP* spectroscopy could serve as a sensitive tool to reveal details of the population mechanism of SAMO states. Recently, it has been demonstrated theoretically that C_{60} can undergo asymmetrical fission due to its large dipole moment when irradiated with a two-color laser field [223]. Investigation of electron and ion channels with the *PoP* technique would be a proof-of-principle test of this idea.

Insight into nanoplasma formation and its influence on electron acceleration can be achieved through the pump-probe experiment on metal clusters. The first pump-pulse ionizes the cluster and initiates expansion of the system, while the second ω-2ω pulse probes rescattering dynamics and electron acceleration in the expanding system by means of PP and RPC spectra. This would be a continuation of an experiment performed by Johannes Passig, me and others at MPQ in Garching with CEP laser pulses. In that experiment, directional photoemission has been observed by means of stereo-TOF spectrometer where the results could be analyzed by an asymmetry parameter. At the nanoplasma resonance, energetic electrons up to 1 keV are clearly influenced by the CEP phase [76]. PP and RPC spectra could reveal further details due to the additional momentum resolution of a VMI spectrometer. The present setup is capable of mapping such high electron energies.

The *PoP* technique can be considered not only as an experiment testing rescattering dynamics, but also as a precise timing experiment. As discussed in Chapter 4, the interference pattern that builds up at large angles relative to the laser polarization axis originates from two electron trajectories released in opposite directions along the laser polarization axis. Oscillations in the positions of the interference maxima reflect differences in the accumulated phase. In modifying the ionisation with the ω-2ω field any contribution which modifies the accumulated phase will change the interference pattern. Hence, PoP provides a tool that may allow us to attack fundamental issues such like tunnelling time, ionisation delay or, spatial offsets.

Bibliography

[1] C. Winterfeldt, C. Spielmann, and G. Gerber, "Colloquium:optimal control of high-harmonic generation," *Rev. Mod. Phys.*, p. 117, 2008.

[2] T. Baumert, R. Thalweiser, and G. Gerber, "Femtosecond two-photon ionization spectroscopy of the b state of Na_3 clusters," *Chem. Phys. Lett.*, p. 29, 1993.

[3] P. B. Corkum and F. Krausz, "Attosecond science," *Nat. Phys.*, p. 381, 2007.

[4] F. Krausz and M. Ivanov, "Attosecond physics," *Rev. Mod. Phys.*, vol. 81, p. 163, 2009.

[5] A. H. Zewail, "Femtochemistry: Atomic-scale dynamics of the chemical bond," *J. Phys. Chem. A*, p. 5660, 2000.

[6] M. M. Martin and J. T. Hynes, eds., *Femtochemistry and Femtobiolgy*. Elsevier, Amsterdam, 2004.

[7] A. W. J. Castelman and M. L. Kimble, eds., *Femtochemistry VII*. Elsevier, Amsterdam, 2006.

[8] A. Baltuška, M. Uiberacker, E. Goulielmakis, R. Kienberger, V. Yakovlev, T. Udem, T. Hänsch, and F. Krausz, "Phase-controlled amplification of few-cycle laser pulses," *Selected Topics in Quantum Electronics, IEEE Journal of*, p. 972, 2003.

[9] M. Nisoli, S. De Silvestri, and O. Svelto, "Generation of high energy 10 fs pulses by a new pulse compression technique," *Appl. Phys. Lett.*, 1996.

[10] M. Gensch, L. Bittner, A. Chesnov, H. Delsim-Hashemi, M. Drescher, B. Faatz, J. Feldhaus, U. Fruehling, G. Geloni, C. Gerth, O. Grimm, U. Hahn, M. Hesse, S. Kapitzki, V. Kocharyan, O. Kozlov, E. Matyushevsky, N. Morozov, D. Petrov, E. Ploenjes, M. Roehling, J. Rossbach, E. Saldin, B. Schmidt, P. Schmueser, E. Schneidmiller, E. Syresin, A. Willner, and M. Yurkov, "New infrared undulator beamline at flash," *Infrared Physics & Technology*, vol. 51, p. 423, 2008.

[11] N. Stojanovic and M. Drescher, "Accelerator- and laser-based sources of high-field terahertz pulses," *J. Phys. B*, vol. 46, p. 192001, 2013.

[12] K. Zhao, Q. Zhang, M. Chini, Y. Wu, X. Wang, and Z. Chang, “Tailoring a 67 attosecond pulse through advantageous phase-mismatch,” *Opt. Lett.*, p. 3891, 2012.

[13] H. Wabnitz, L. Bittner, A. R. B. de Castro, R. Dohrmann, P. Gurtler, T. Laarmann, W. Laasch, J. Schulz, A. Swiderski, K. von Haeften, T. Moller, B. Faatz, A. Fateev, J. Feldhaus, C. Gerth, U. Hahn, E. Saldin, E. Schneidmiller, K. Sytchev, K. Tiedtke, R. Treusch, and M. Yurkov, “Attosecond science,” *Nat. Phys.*, p. 381, 2007.

[14] U. Zastrau, P. Sperling, M. Harmand, A. Becker, T. Bornath, R. Bredow, S. Dziarzhytski, T. Fennel, L. B. Fletcher, E. Förster, S. Göde, G. Gregori, V. Hilbert, D. Hochhaus, B. Holst, T. Laarmann, H. J. Lee, T. Ma, J. P. Mithen, R. Mitzner, C. D. Murphy, M. Nakatsutsumi, P. Neumayer, A. Przystawik, S. Roling, M. Schulz, B. Siemer, S. Skruszewicz, J. Tiggesbäumker, S. Toleikis, T. Tschentscher, T. White, M. Wöstmann, H. Zacharias, T. Döppner, S. H. Glenzer, and R. Redmer, “Resolving ultrafast heating of dense cryogenic hydrogen,” *Phys. Rev. Lett.*, p. 105002, 2014.

[15] R. R. Fäustlin, T. Bornath, T. Döppner, S. Düsterer, E. Förster, C. Fortmann, S. H. Glenzer, S. Göde, G. Gregori, R. Irsig, T. Laarmann, H. J. Lee, B. Li, K.-H. Meiwes-Broer, J. Mithen, B. Nagler, A. Przystawik, H. Redlin, R. Redmer, H. Reinholz, G. Röpke, F. Tavella, R. Thiele, J. Tiggesbäumker, S. Toleikis, I. Uschmann, S. M. Vinko, T. Whitcher, U. Zastrau, B. Ziaja, and T. Tschentscher, “Observation of ultrafast nonequilibrium collective dynamics in warm dense hydrogen,” *Phys. Rev. Lett.*, p. 125002, 2010.

[16] S. H. Glenzer, G. Gregori, R. W. Lee, F. J. Rogers, S. W. Pollaine, and O. L. Landen, “Demonstration of spectrally resolved x-ray scattering in dense plasmas,” *Phys. Rev. Lett.*, p. 175002, 2003.

[17] G. Steinmeyer, D. H. Sutter, L. Gallmann, N. Matuschek, and U. Keller, “Frontiers in ultrashort pulse generation: Pushing the limits in linear and nonlinear optics,” *Science*, vol. 286, p. 1507, 1999.

[18] M. Nisoli, S. D. Silvestri, O. Svelto, R. Szipöcs, K. Ferencz, C. Spielmann, S. Sartania, and F. Krausz, “Compression of high-energy laser pulses below 5 fs,” *Opt. Lett.*, vol. 22, pp. 522–, 1997.

[19] M. T. Hassan, A. Wirth, I. Grguraš, A. Moulet, T. T. Luu, J. Gagnon, V. Pervak, and E. Goulielmakis, “Invited article: Attosecond photonics: Synthesis and control of light transients,” *Rev. Sci. Instrum.*, vol. 83, p. 111301, 2012.

[20] C. Manzoni, O. D. Mücke, G. Cirmi, S. Fang, J. Moses, S.-W. Huang, K.-H. Hong, G. Cerullo, and F. X. Kärtner, "Coherent pulse synthesis: towards sub-cycle optical waveforms," *Laser & Photonics Reviews*, vol. 9, p. 129, 2015.

[21] A. Baltuška, T. Udem, M. Uiberacker, M. Hentschel, E. Goulielmakis, C. Gohle, R. Holzwarth, V. S. Yakovlev, A. Scrinzi, T. W. Hänsch, and F. Krausz, "Attosecond control of electronic processes by intense light fields," *Nature*, vol. 421, p. 611, 2003.

[22] M. Hentschel, R. Kienberger, C. Spielmann, G. A. Reider, N. Milošević, T. Brabec, P. Corkum, U. Heinzmann, M. Drescher, and F. Krausz, "Attosecond science," *Nat. Phys.*, p. 381, 2007.

[23] M. Shapiro, J. W. Hepbrun, and P. Brumer, "Simplified laser control of unimolecular reactions: Simultaneous (ω_1, ω_3) excitation," *Chem. Phys. Lett.*, vol. **149**, p. 451, 2015.

[24] P. W. Brumer and M. Shapiro, *Principles of the Quantum Control of Molecular Processes*. Wiley, New York, 2003.

[25] D. J. Tannor and S. A. Rice, "Control of selectivity of chemical reaction via control of wave packet evolution," *J. Chem. Phys.*, vol. 83, p. 5013, 1985.

[26] D. J. Tannor, R. Kosloff, and S. A. Rice, "Coherent pulse sequence induced control of selectivity of reactions: Exact quantum mechanical calculations," *J. Chem. Phys.*, vol. 85, p. 5805, 1986.

[27] L. Zhu, V. Kleiman, X. Li, S. P. Lu, K. Trentelman, and R. J. Gordon, "Coherent laser control of the product distribution obtained in the photoexcitation of HI," *Science*, vol. 270, p. 77, 1995.

[28] L. Zhu, K. Suto, J. A. Fiss, R. Wada, T. Seideman, and R. J. Gordon, "Effect of resonances on the coherent control of the photoionization and photodissociation of HI and DI," *Phys. Rev. Lett.*, vol. 79, p. 4108, 1997.

[29] R. Bowman, M. Dantus, and A. Zewail, "Femtosecond multiphoton dynamics of higher-energy potentials," *Chem. Phys. Lett.*, vol. 174, p. 546, 1990.

[30] R. J. Gordon and S. A. Rice, "Active control of the dynamics of atoms and molecules," *Ann. Rev. Phys. Chem.*, p. 601, 1997.

[31] C. Brif, R. Chakrabarti, and H. Rabitz, "Control of quantum phenomena: past, present and future," *New J. Phys.*, p. 075008, 2010.

[32] H. G. Muller, H. B. van Linden van den Heuvell, and M. J. van der Wiel, “Dressing of continuum states and MPI of Xe in a two-color experiment,” *J. Phys. B*, vol. 19, p. L733, 1986.

[33] G. G. Paulus, W. Becker, and H. Walther, “Classical rescattering effects in two-color above-threshold ionization,” *Phys. Rev. A*, vol. 52, p. 4043, 1995.

[34] P. M. Paul, E. S. Toma, P. Breger, G. Mullot, F. Augé, P. Balcou, H. G. Muller, and P. Agostini, “Observation of a train of attosecond pulses from high harmonic generation,” *Science*, vol. 292, p. 1689, 2001.

[35] M. Drescher, M. Hentschel, R. Kienberger, G. Tempea, C. Spielmann, G. A. Reider, P. B. Corkum, and F. Krausz, “X-ray pulses approaching the attosecond frontier,” *Science*, vol. 291, p. 1923, 2001.

[36] R. Kienberger, E. Goulielmakis, M. Uiberacker, A. Baltuška, V. Yakovlev, F. Bammer, A. Scrinzi, T. Westerwalbesloh, U. Kleineberg, U. Heinzmann, M. Drescher, and F. Krausz, “Atomic transient recorder,” *Nature*, vol. 427, p. 817, 2004.

[37] E. Goulielmakis, M. Uiberacker, R. Kienberger, A. Baltuška, V. Yakovlev, A. Scrinzi, T. Westerwalbesloh, U. Kleineberg, U. Heinzmann, M. Drescher, and F. Krausz, “Direct measurement of light waves,” *Science*, vol. 305, p. 1267, 2004.

[38] E. Goulielmakis, M. Schultze, M. Hofstetter, V. S. Yakovlev, J. Gagnon, M. Uiberacker, A. L. Aquila, E. M. Gullikson, D. T. Attwood, R. Kienberger, F. Krausz, and U. Kleineberg, “Single-cycle nonlinear optics,” *Science*, vol. 320, p. 1614, 2008.

[39] M. Drescher, M. Hentschel, R. Kienberger, M. Uiberacker, V. Yakovlev, A. Scrinzi, T. Westerwalbesloh, U. Kleineberg, U. Heinzmann, and F. Krausz, “Time-resolved atomic inner-shell spectroscopy,” *Nature*, vol. 419, p. 803, 2002.

[40] E. Goulielmakis, Z.-H. Loh, A. Wirth, R. Santra, N. Rohringer, V. S. Yakovlev, S. Zherebtsov, T. Pfeifer, A. M. Azzeer, M. F. Kling, S. R. Leone, and F. Krausz, “Real-time observation of valence electron motion,” *Nature*, vol. 466, p. 739, 2010.

[41] A. Wirth, M. T. Hassan, I. Grguraš, J. Gagnon, A. Moulet, T. T. Luu, S. Pabst, R. Santra, Z. A. Alahmed, A. M. Azzeer, V. S. Yakovlev, V. Pervak, F. Krausz, and E. Goulielmakis, “Synthesized light transients,” *Science*, vol. 334, p. 195, 2011.

[42] A. Harth, M. Schultze, T. Lang, T. Binhammer, S. Rausch, and U. Morgner, "Two-color pumped OPCPA system emitting spectra spanning 1.5 octaves from VIS to nir," *Opt. Express*, vol. 20, p. 3076, 2012.

[43] H. G. Muller, P. H. Bucksbaum, D. W. Schumacher, and A. Zavriyev, "Above-threshold ionisation with a two-color laser field," *J. Phys. B*, vol. 23, p. 2761, 1990.

[44] D. W. Schumacher, F. Weihe, H. G. Muller, and P. H. Bucksbaum, "Phase dependence of intense field ionization: A study using two colors," *Phys. Rev. Lett.*, vol. 73, p. 1344, 1994.

[45] Y. Huo, Z. Zeng, R. Li, and Z. Xu, "Single attosecond pulse generation using two-color polarized time-gating technique," *Opt. Express*, vol. 13, p. 9897, 2005.

[46] J. Mauritsson, P. Johnsson, E. Gustafsson, A. L'Huillier, K. J. Schafer, and M. B. Gaarde, "Attosecond pulse trains generated using two color laser fields," *Phys. Rev. Lett.*, vol. 97, p. 013001.

[47] N. Dudovich, O. Smirnova, Y. Levesque, J. aand Mairesse, M. Y. Ivanov, D. M. Villeneuve, and P. B. Corkum, "Measuring and controlling the birth of attosecond xuv pulses," *Nat. Phys.*, vol. 2, p. 781, 2006.

[48] Z. Zeng, Y. Cheng, X. Song, R. Li, and Z. Xu, "Generation of an extreme ultraviolet supercontinuum in a two-color laser field," *Phys. Rev. Lett.*, vol. 98, p. 203901, 2007.

[49] D. Shafir, Y. Mairesse, D. M. Villeneuve, P. B. Corkum, and N. Dudovich, "Atomic wavefunctions probed through strong-field light-matter interaction," *Nat. Phys.*, vol. 5, p. 412, 2009.

[50] H. Niikura, N. Dudovich, D. M. Villeneuve, and P. B. Corkum, "Mapping molecular orbital symmetry on high-order harmonic generation spectrum using two-color laser fields," *Phys. Rev. Lett.*, vol. 105, p. 053003, 2010.

[51] L. Brugnera, D. J. Hoffmann, T. Siegel, F. Frank, A. Zaïr, J. W. G. Tisch, and J. P. Marangos, "Trajectory selection in high harmonic generation by controlling the phase between orthogonal two-color fields," *Phys. Rev. Lett.*, vol. 107, p. 153902, 2011.

[52] J. M. Dahlström, A. L'Huillier, and J. Mauritsson, "Quantum mechanical approach to probing the birth of attosecond pulses using a two-color field," *J. Phys. B*, vol. 44, p. 095602, 2011.

[53] D. Shafir, H. Soifer, B. D. Bruner, M. Dagan, Y. Mairesse, S. Patchkovskii, M. Y. Ivanov, O. Smirnova, and N. Dudovich, “Coulomb focusing in intense field atomic processes,” *Nature*, vol. 485, p. 343, 2012.

[54] P. M. Kraus, D. Baykusheva, and H. J. Wörner, “Two-pulse orientation dynamics and high-harmonic spectroscopy of strongly-oriented molecules,” *J. Phys. B*, vol. 47, p. 124030, 2014.

[55] Y. Zhou, Q. Liao, Q. Zhang, W. Hong, and P. Lu, “Controlling nonsequential double ionization via two-color few-cycle pulses,” *Opt. Express*, vol. 18, p. 632, 2010.

[56] Z. Yue-Ming, L. Qing, H. Cheng, T. Ai-Hong, and L. Pei-Xiang, “Electron correlation in nonsequential double ionization of helium by two-color pulses,” *Chinese Physics Letters*, vol. 27, p. 123201, 2010.

[57] Y. Zhou, C. Huang, A. Tong, Q. Liao, and P. Lu, “Correlated electron dynamics in nonsequential double ionization by orthogonal two-color laser pulses,” *Opt. Express*, vol. 19, p. 2301, 2011.

[58] L. Chen, Y. Zhou, C. Huang, Q. Zhang, and P. Lu, “Attosecond-resolved electron emission in nonsequential double ionization,” *Phys. Rev. A*, vol. 88, p. 043425, 2013.

[59] M. Richter, M. Kunitski, M. Schöffler, T. Jahnke, L. P. H. Schmidt, M. Li, Y. Liu, and R. Dörner, “Streaking temporal double-slit interference by an orthogonal two-color laser field,” *Phys. Rev. Lett.*, vol. 114, p. 143001, 2015.

[60] M. Kitzler and M. Lezius, “Spatial control of recollision wave packets with attosecond precision,” *Phys. Rev. Lett.*, vol. 95, p. 253001, 2005.

[61] D. Ray, Z. Chen, S. De, W. Cao, I. V. Litvinyuk, A. T. Le, C. D. Lin, M. F. Kling, and C. L. Cocke, “Momentum spectra of electrons rescattered from rare-gas targets following their extraction by one- and two-color femtosecond laser pulses,” *Phys. Rev. A*, vol. 83, p. 013410, 2011.

[62] X. Xie, S. Roither, D. Kartashov, E. Persson, D. G. Arbó, L. Zhang, S. Gräfe, M. S. Schöffler, J. Burgdörfer, A. Baltuška, and M. Kitzler, “Attosecond probe of valence-electron wave packets by subcycle sculpted laser fields,” *Phys. Rev. Lett.*, vol. 108, p. 193004, 2012.

[63] X. Xie, S. Roither, S. Gräfe, D. Kartashov, E. Persson, C. Lemell, L. Zhang, M. S. Sch{"affler, A. Baltuška, J. Burgd{"orfer, and M. Kitzler, “Probing the influence of the coulomb field on atomic ionization by sculpted two-color laser fields,” *New J. Phys.*, vol. 15, p. 043050, 2013.

[64] L. Zhang, X. Xie, S. Roither, D. Kartashov, Y. Wang, C. Wang, M. Schöffler, D. Shafir, P. B. Corkum, A. Baltuška, I. Ivanov, A. Kheifets, X. Liu, A. Staudte, and M. Kitzler, "Laser-sub-cycle two-dimensional electron-momentum mapping using orthogonal two-color fields," *Phys. Rev. A*, vol. 90, p. 061401, 2014.

[65] C. A. Mancuso, D. D. Hickstein, P. Grychtol, R. Knut, O. Kfir, X.-M. Tong, F. Dollar, D. Zusin, M. Gopalakrishnan, C. Gentry, E. Turgut, J. L. Ellis, M.-C. Chen, A. Fleischer, O. Cohen, H. C. Kapteyn, and M. M. Murnane, "Strong-field ionization with two-color circularly polarized laser fields," *Phys. Rev. A*, vol. 91, p. 031402, 2015.

[66] X. Xie, "Two-dimensional attosecond electron wave-packet interferometry," *Phys. Rev. Lett.*, vol. **114**, p. 173003, 2015.

[67] S. De, I. Znakovskaya, D. Ray, F. Anis, N. G. Johnson, I. A. Bocharova, M. Magrakvelidze, B. D. Esry, C. L. Cocke, I. V. Litvinyuk, and M. F. Kling, "Field-free orientation of co molecules by femtosecond two-color laser fields," *Phys. Rev. Lett.*, vol. 103, p. 153002, 2009.

[68] M. Spanner, S. Patchkovskii, E. Frumker, and P. Corkum, "Mechanisms of two-color laser-induced field-free molecular orientation," *Phys. Rev. Lett.*, vol. 109, p. 113001, 2012.

[69] E. Frumker, C. T. Hebeisen, N. Kajumba, J. B. Bertrand, H. J. Wörner, M. Spanner, D. M. Villeneuve, A. Naumov, and P. B. Corkum, "Oriented rotational wave-packet dynamics studies via high harmonic generation," *Phys. Rev. Lett.*, vol. 109, p. 113901, 2012.

[70] X. Xie, K. Doblhoff-Dier, H. Xu, S. Roither, M. S. Schöffler, D. Kartashov, S. Erattupuzha, T. Rathje, G. G. Paulus, K. Yamanouchi, A. Baltuška, S. Gräfe, and M. Kitzler, "Selective control over fragmentation reactions in polyatomic molecules using impulsive laser alignment," *Phys. Rev. Lett.*, vol. 112, p. 163003, 2014.

[71] P. M. Kraus, D. Baykusheva, and H. J. Wörner, "Two-pulse field-free orientation reveals anisotropy of molecular shape resonance," *Phys. Rev. Lett.*, vol. 113, p. 023001, 2014.

[72] P. M. Kraus, O. I. Tolstikhin, D. Baykusheva, A. Rupenyan, J. Schneider, C. Z. Bisgaard, T. Morishita, F. Jensen, L. B. Madsen, and H. J. Wörner, "Observation of laser-induced electronic structure in oriented polyatomic molecules," *Nat. Commu.*, vol. 6, 2015.

[73] D. Ray, S. De, H. Mashiko, I. Znakovskaya, F. He, U. Thumm, G. G. Paulus, M. Kling, I. Litvinyuk, and C. L. Cocke, "Asymmetric dissociation of H_2 and D_2 by a two-color laser field," *Journal of Physics: Conference Series*, vol. 194, p. 032064, 2009.

[74] D. Ray, F. He, S. De, W. Cao, H. Mashiko, P. Ranitovic, K. P. Singh, I. Znakovskaya, U. Thumm, G. G. Paulus, M. F. Kling, I. V. Litvinyuk, and C. L. Cocke, "Ion-energy dependence of asymmetric dissociation of D_2 by a two-color laser field," *Phys. Rev. Lett.*, vol. 103, p. 223201, 2009.

[75] I. Znakovskaya, *Light-waveform control of molecular processes.* Ludwig-Maximilians-Universität München, 2012.

[76] J. Passig, *Steuerung der Electronenemission aus Silberclustern in Intensiven, Geformten Laserfeldern.* PhD Dissertation, Universtität Rostock, 2012.

[77] P. B. Corkum, "Plasma perspective on strong field multiphoton ionization," *Phys. Rev. Lett.*, vol. 71, p. 1994, 1994.

[78] P. Salières, B. Carrè, L. Le Déroff, F. Grasbon, G. G. Paulus, H. Walther, R. Kopold, W. Becker, D. B. Milošević, A. Sanpera, and M. Lewenstein, "Feynman's path-integral approach for intense-laser-atom interactions," *Science*, vol. 292, p. 902, 2001.

[79] D. B. Milošević, G. G. Paulus, D. Bauer, and W. Becker, "Above-threshold ionization by few-cycle pulses," *J. Phys. B*, vol. 39, p. R203, 2006.

[80] W. Becker, F. Grasbon, R. Kopold, D. Milošević, G. Paulus, and H. Walther, "Above-threshold ionization: From classical features to quantum effects," *Advances in Atomic Molecular and Optical Physics*, vol. 48, p. 35, 2002.

[81] G. Mainfray and C. Manus, "Multiphoton ionization of atoms.," *Rep. Prog. Phys.*, vol. 54, p. 1333, (1991).

[82] B. W. Boreham and B. Luther-Davies, "High-energy electron acceleration by ponderomotive forces in tenuous plasmas," *J. App. Phys.*, vol. 50, p. 2533, 1979.

[83] H. A. H. Boot and R. B. R. S. Harvie, "Charged particles in non-uniform radio-frequency field.," *Nature*, vol. 30, p. 1187, (1957).

[84] J. H. Eberly, J. Javanainen, and K. Rzażewski, "Above-Threshold Ionization," *Phys. Rep.*, vol. 204, p. 331, (1991).

[85] A. Einstein, "On a Heuristic Viewpoint Concerning the Production and Transformation of Light.," *Annalen der Physik*, vol. 17, p. 132, (1905).

[86] P. Agostini, G. Barjot, J. F. Bonnal, G. Mainfray, C. Manus, and J. Morellec, "Multiphoton ionization of Hydrogen and Rare Gases.," *J. Quantum. Electron.*, vol. QE-4, p. 667, (1968).

[87] J. L. Keldysh, "Ionization in the field of a strong electromagnetic wave," *Soviet Physics JETP*, vol. 20, p. 1307, 1965.

[88] M. J. DeWitt and R. J. Levis, "Calculating the keldysh adiabaticity parameter for atomic, diatomic, and polyatomic molecules," *J. Chem. Phys.*, vol. 108, p. 7739, 1998.

[89] S. L. Chin, ed., *Multiphoton lonization of Atoms*. Elsevier, 2012.

[90] N. Delone and V. Krainov, *Multiphoton Processes in Atoms (Springer Series on Atomic, Optical, and Plasma Physics)*. Springer, 2000.

[91] R. Wallace, "Perturbation theory of multiphoton processes," *Phys. Rev. Lett.*, vol. 17, p. 397, 1966.

[92] L. A. Lompre, G. Mainfray, C. Manus, and J. Thebault, "Multiphoton ionization of rare gases by a tunable-wavelength 30-psec laser pulse at 1.06 μm," *Phys. Rev. A*, vol. 15, p. 1604, 1977.

[93] P. Agostini, A. Antonetti, P. Breger, M. Crance, A. Migus, H. G. Muller, and G. Petite, "Resonant multiphoton ionisation of xenon with high-intensity femtosecond pulses," *J. Phys. B*, vol. 22, p. 1971.

[94] H. G. Muller, A. Tip, and M. J. van der Wiel, "Ponderomotive force and ac stark shift in multiphoton ionisation," *J.Phys. B*, vol. 16, p. L679, 1983.

[95] V. P. Krainov and N. B. Delone, "Ac stark shift of atomic energy levels," *Phys-Usp*, vol. 42, p. 669, 1999.

[96] P. Kruit, J. Kimman, H. G. Muller, and M. J. van der Wiel, "Electron spectra from multiphoton ionization of xenon at 1064, 532 and 355 nm.," *Phys. Rev. A*, vol. 28, p. 248, 1983.

[97] R. R. Freeman, P. H. Buksbaum, H. Milchberg, S. Darack, D. Schumacher, and M. E. Geusic, "Above-threshold ionization with subpicosecond laser pulses," *Phys. Rev. Lett.*, vol. 59, p. 1092, 1987.

[98] H. H. V. Schyja, T. Lang, "Chanel switching in above-threshold ionization of xenon," *Phys. Rev. A*, vol. 57, p. 3692, 1998.

[99] P. Hansch, M. A. Walker, and L. D. V. Woerkom, "Eight- and nine-photon resonances in multiphoton ionization of xenon," *Phys. Rev. A*, vol. 57, p. 57, (1998).

[100] T. Marchenko, H. G. Muller, K. J. Schafer, and M. J. J. Vrakking, "Wavelength dependence of photoelectron spectra in above-threshold ionization," *J. Phys. B*, vol. 43, p. 185001, 2010.

[101] M. Protopapas, C. H. Keitel, and P. L. Kight, "Atom physics with supe-high intensity lasers.," *Rep. Prog. Phys*, vol. 60, p. 389, (1997).

[102] M. V. Ammosov, N. B. Delone, and V. P. Krainov, "Tunnel ionization of complex atoms and of atomic ions in an alternating electromagnetic fiels," *Sov. Phys. JETP*, vol. 64, p. 1191, 1986.

[103] P. B. Corkum, N. H. Burnett, and F. Brunel, "Above-threshold ionization in the long-wavelength limit," *Phys. Rev. Lett.*, vol. 62, p. 1259, 1989.

[104] P. Agostini and L. F. Di Mauro, "The physics of attosecond light pulses," *Reports on Progress in Physics*, vol. 67, p. 813, 2004.

[105] M. Lewenstein, P. Balcou, M. Y. Ivanov, A. L'Huillier, and P. B. Corkum, "Theory of high-harmonic generation by low-frequency laser fields," *Phys. Rev. A*, vol. 49, p. 2117, 1994.

[106] J. L. Krause, K. J. Schafer, and K. C. Kulander, "High-order harmonic generation from atoms and ions in the high intensity regime," *Phys. Rev. Lett.*, vol. 68, p. 3535, 1992.

[107] D. B. Milošević and W. Becker, "Classical cutoffs for laser-induced nonsequential double ionization," *Phys. Rev. A*, vol. 68, p. 065401, 2003.

[108] J. Itatani, J. Levesque, D. Zeidler, H. Niikura, H. Pepin, J. Kieffer, P. Corkum, and D. Villeneuve, "Tomographic imaging of molecular orbitals," *Nature*, vol. 432, p. 867, 2004.

[109] P. Hansch, M. Walker, and L. VanWoerkom, "Resonant hot-electron production in above-threshold ionization," *Phys. Rev. A*, vol. 55, p. R2535, 1997.

[110] M. Hertlein, P. Bucksbaum, and H. Muller, "Evidence for resonant effects in high-order ATI spectra," *J. Phys. B*, vol. 30, p. L197, 1997.

[111] F. H. M. Faisal, "Strong-Field Physics Ionization surprise," *Nat. Phys.*, vol. 5, p. 319, 2009.

[112] D. Bauer. Private communication, Universität Rostock, 2015.

[113] B. Sheehy, R. Lafon, M. Widmer, B. Walker, L. DiMauro, P. Agostini, and K. Kulander, "Single- and multiple-electron dynamics in the strong-field tunneling limit," *Phys. Rev. A*, vol. 58, p. 3942, 1998.

[114] S. Larochelle, A. Talebpour, and S. Chin, "Non-sequential multiple ionization of rare gas atoms in a Ti : Sapphire laser field," *J. Phys. B*, vol. 31, pp. 1201,, 1998.

[115] R. Moshammer, B. Feuerstein, W. Schmitt, A. Dorn, C. Schroter, J. Ullrich, H. Rottke, C. Trump, M. Wittmann, G. Korn, K. Hoffmann, and W. Sandner, "Momentum distributions of $\mathrm{N}e^{n+}$ ions created by an intense ultrashort laser pulse," *Phys. Rev. Lett.*, vol. 84, p. 447, 2000.

[116] B. Feuerstein, R. Mommer, D. Fischer, A. Dorn, C. D. Schröter, J. Deipenwisch, J. R. Crespo Lopez-Urrutia, C. Höhr, P. Neumayer, J. Ullrich, H. Rottke, C. Trump, M. Wittmann, G. Korn, and W. Sandner, "Separation of recollision mechanisms in nonsequential strong field double ionization of ar: The role of excitation tunneling," *Phys. Rev. Lett.*, vol. 87, p. 043003, 2001.

[117] R. Kopold, W. Becker, H. Rottke, and W. Sandner, "Routes to nonsequential double ionization," *Phys. Rev. Lett.*, vol. 85, p. 3781, 2000.

[118] B. Bergues, M. Kuebel, N. G. Johnson, B. Fischer, N. Camus, K. J. Betsch, O. Herrwerth, A. Senftleben, A. M. Sayler, T. Rathje, T. Pfeifer, I. Ben-Itzhak, R. R. Jones, G. G. Paulus, F. Krausz, R. Moshammer, J. Ullrich, and M. F. Kling, "Attosecond tracing of correlated electron-emission in non-sequential double ionization," *Nat. Commun.*, vol. 3, 2012.

[119] C. Chen, Y.-Y. Yin, and D. S. Elliott, "Interference between optical transitions," *Phys. Rev. Lett.*, vol. 64, p. 507, 1990.

[120] Y.-Y. Yin, C. Chen, D. S. Elliott, and A. V. Smith, "Asymmetric photoelectron angular distributions from interfering photoionization processes," *Phys. Rev. Lett.*, vol. 69, p. 2353, 1992.

[121] D. Ray, *Photo-Electron Momentum Distribution and Electron Localization Studies from Laser-Induced Atomic and Molecular Dissociation.* PhD Dissertation, Kansas State University, 2010.

[122] G. G. Paulus, F. Lindner, H. Walther, A. Baltuška, E. Goulielmakis, M. Lezius, and F. Krausz, "Measurement of the phase of few-cycle laser pulses," *Phys. Rev. Lett.*, vol. 91, p. 253004, 2003.

[123] G. G. Paulus, W. Nicklich, H. Xu, P. Lambropoulos, and H. Walther, "Plateau in above threshold ionization spectra," *Phys. Rev. Lett.*, vol. 72, p. 2851, 1994.

[124] M. F. Kling, J. Rauschenberger, A. J. Verhoef, E. Hasovic, T. Uphues, D. B. Milosevic, H. G. Muller, and M. J. J. Vrakking, “Imaging of carrier-envelope phase effects in above-threshold ionization with intense few-cycle laser fields,” *New J. Phys.*, vol. 10, 2008.

[125] T. Morishita, A.-T. Le, Z. Chen, and C. D. Lin, “Potential for ultrafast dynamic chemical imaging with few-cycle infrared lasers,” *New J. Phys.*, vol. 10, p. 025011, 2008.

[126] P. Agostini, F. Fabre, G. Mainfray, G. Petite, and N. K. Rahman, “Free-free transitions following six-photon ionization of xenon atoms,” *Phys. Rev. Lett.*, vol. 42, p. 1127, 1979.

[127] T. J. McIlrath, P. H. Bucksbaum, R. R. Freeman, and M. Bashkansky, “Above-threshold ionization processes in xenon and krypton,” *Phys. Rev. A*, vol. 35, p. 4611, 1987.

[128] M. Wollenhaupt, A. Assion, D. Liese, C. Sarpe-Tudoran, T. Baumert, S. Zamith, M. A. Bouchene, B. Girard, A. Flettner, U. Weichmann, and G. Gerber, “Interferences of ultrashort free electron wave packets,” *Phys. Rev. Lett.*, vol. 89, p. 173001, 2002.

[129] F. Lindner, M. G. Schätzel, H. Walther, A. Baltuška, E. Goulielmakis, F. Krausz, D. B. Milošević, D. Bauer, W. Becker, and G. G. Paulus, “Attosecond double-slit experiment,” *Phys. Rev. Lett.*, vol. 95, p. 040401, 2005.

[130] H. G. Muller and A. Tip, “Multiphoton ionization in strong fields,” *Phys. Rev. A*, vol. 30, p. 3039, 1984.

[131] J. J. Macklin, J. D. Kmetec, and C. L. Gordon, “High-order harmonic generation using intense femtosecond pulses,” *Phys. Rev. Lett.*, vol. 70, p. 766, 1993.

[132] D. N. Fittinghoff, P. R. Bolton, B. Chang, and K. C. Kulander, “Observation of nonsequential double ionization of helium with optical tunneling,” *Phys. Rev. Lett.*, vol. 69, p. 2642, 1992.

[133] A. S. Landsman, M. Weger, J. Maurer, R. Boge, A. Ludwig, S. Heuser, C. Cirelli, L. Gallmann, and U. Keller, “Ultrafast resolution of tunneling delay time,” *Optica*, vol. 1, p. 343, 2014.

[134] P. Korneev, S. Popruzhenko, S. Goreslavski, T.-M. Yan, D. Bauer, W. Becker, M. Kübel, M. Kling, C. Rödel, M. Wünsche, and G. Paulus, “Interference carpets in above-threshold ionization: From the coulomb-free to the coulomb-dominated regime,” *Phys. Rev. Lett.*, vol. 108, p. 223601, 2012.

[135] P. A. Korneev, S. V. Popruzhenko, S. P. Goreslavski, W. Becker, G. G. Paulus, B. Fetić, and D. B. Milošević, “Interference structure of above-threshold ionization versus above-threshold detachment,” *New J. Phys.*, vol. 14, p. 055019, 2012.

[136] Y. Huismans, A. Rouzée, A. Gijsbertsen, J. H. Jungmann, A. S. Smolkowska, P. S. W. M. Logman, F. Lépine, C. Cauchy, S. Zamith, T. Marchenko, J. M. Bakker, G. Berden, B. Redlich, A. F. G. van der Meer, H. G. Muller, W. Vermin, K. J. Schafer, M. Spanner, M. Y. Ivanov, O. Smirnova, D. Bauer, S. V. Popruzhenko, and M. J. J. Vrakking, “Time-resolved holography with photoelectrons,” *Science*, vol. 331, p. 61, 2011.

[137] D. D. Hickstein, P. Ranitovic, S. Witte, X.-M. Tong, Y. Huismans, P. Arpin, X. Zhou, K. E. Keister, C. W. Hogle, B. Zhang, C. Ding, P. Johnsson, N. Toshima, M. J. J. Vrakking, M. M. Murnane, and H. C. Kapteyn, “Direct visualization of laser-driven electron multiple scattering and tunneling distance in strong-field ionization,” *Phys. Rev. Lett.*, vol. 109, p. 073004, 2012.

[138] S. Micheau, Z. Chen, A. T. Le, J. Rauschenberger, M. F. Kling, and C. D. Lin, “Accurate retrieval of target structures and laser parameters of few-cycle pulses from photoelectron momentum spectra,” *Phys. Rev. Lett.*, vol. 102, p. 073001, 2009.

[139] T. Morishita, M. Okunishi, K. Shimada, G. Prümper, Z. Chen, S. Watanabe, K. Ueda, and C. D. Lin, “Retrieval of experimental differential electron-ion elastic scattering cross sections from high-energy ati spectra of rare gas atoms by infrared lasers,” *J. Phys. B*, vol. 42, p. 105205, 2009.

[140] J. W. Goodman, *Introduction To Fourier Optics*. McGraw-Hill Science/Engineering/Math, 1996.

[141] F. Lindner, G. G. Paulus, H. Walther, A. Baltuška, E. Goulielmakis, M. Lezius, and F. Krausz, “Gouy phase shift for few-cycle laser pulses,” *Phys. Rev. Lett.*, vol. 92, p. 113001, 2004.

[142] L. G. Gouy, “Sur une propriete nouvelle des ondes lumineuses,” *C. R. Acad. Sci.*, p. 1251, 1890.

[143] N. C. R. Holme, B. C. Daly, M. T. Myaing, and T. B. Norris, “Gouy phase shift of single-cycle picosecond acoustic pulses,” *Appl. Phys. Lett.*, vol. 83, p. 392, 2003.

[144] A. B. Ruffin, J. V. Rudd, J. F. Whitaker, S. Feng, and H. G. Winful, “Direct observation of the gouy phase shift with single-cycle terahertz pulses,” *Phys. Rev. Lett.*, vol. 83, p. 3410, 1999.

[145] S. Feng and H. G. Winful, "Physical origin of the gouy phase shift," *Opt. Lett.*, vol. 26, p. 485, 2001.

[146] N. Shivaram, A. Roberts, L. Xu, and A. Sandhu, "In situ spatial mapping of gouy phase slip for high-detail attosecond pump-probe measurements," *Opt. Lett.*, vol. 35, p. 3312, 2010.

[147] P. Balcou and A. L'Huillier, "Phase-matching effects in strong-field harmonic generation," *Phys. Rev. A*, vol. 47, p. 1447, 1993.

[148] M. Lewenstein, P. Salières, and A. L'Huillier, "Phase of the atomic polarization in high-order harmonic generation," *Phys. Rev. A*, vol. 52, p. 4747, 1995.

[149] T. Popmintchev, M.-C. Chen, P. Arpin, M. M. Murnane, and H. C. Kapteyn, "The attosecond nonlinear optics of bright coherent x-ray generation," *Nat. Phot.*, vol. 4, p. 822, 2010.

[150] P. Mulser and D. Bauer, *High Power Laser-Matter Interaction*. Springer, Berlin Heidelberg, 2010.

[151] M. A. Almajid, *Coulomb-Volkov approximation for above-threshold ionization by few-cycle linearly polarized laser pulses*. Master Thesis, Universtität Rostock, 2014.

[152] L. Landau and E. Lifshitz, *Volume 3 of Course of Theoretical Physics: Quantum Mechanics*. Pergamon, Oxford, 1965.

[153] D. Batani, C. Joachain, S. Martellucci, and A. Chester, eds., *Atom, Solids and Plasmas in Super-Intense Laser Fields*. Springer US, 2001.

[154] A. Becker, R. Li, and S. L. Chin, eds., *Progress in Ultrafast Intense Laser Science*.

[155] C. J. Joachain, N. Kylstra, and R. M. Potvliege, *Atoms in intense laser fields*.

[156] T. Brabec, M. Ivanov, and P. Corkum, "Coulomb focusing in intense field atomic processes," *Phys. Rev. A*, vol. 54, p. R2551, 1996.

[157] O. Raz, O. Pedatzur, B. D. Bruner, and N. Dudovich, "Spectral caustics in attosecond science," *Nat. Phot.*, vol. 6, p. 170, 2012.

[158] A. Altland, "Lecture notes in advanced quantum mechanics."

[159] L. V. Keldysh, "Ionization in the field of a strong electromagnetic wave.," *Sov. Phys. JEPT*, vol. 20, p. 1307, (1965).

[160] H. R. Reiss, “Effect of an intense electromagnetic field on a weakly bound system,” *Phys. Rev. A*, vol. 22, p. 1786, 1980.

[161] F. H. M. Faisal, “Multiple absorption of laser photons by atoms,” *J. Phys. B*, vol. 6, p. L89, 1973.

[162] D. G. Arbó, J. E. Miraglia, M. S. Gravielle, K. Schiessl, E. Persson, and J. Burgdörfer, “Coulomb-volkov approximation for near-threshold ionization by short laser pulses,” *Phys. Rev. A*, vol. 77, p. 013401, 2008.

[163] D. W. Chandler and P. L. Houston, “Two-dimensional imaging of state-selected photodissociation products detected by multiphoton ionization,” *J. Chem. Phys*, vol. 87, p. 1445, 1987.

[164] H. Helm, N. Bjerre, M. Dyer, D. Huestis, and M. Saeed, “Images of photoelectrons formated in intense laser fields,” *Phys. Rev. Lett.*, vol. 70, p. 3221, 1993.

[165] A. T. J. B. Eppink and D. H. Parker, “Velocity map imaging of ions and electrons using electrostatic lenses: Application in photoelectron and photofragment ion imaging of molecular oxygen.,” *Rev. Sci. Instr.*, vol. 68, p. 3477, 1997.

[166] Y. Jia, X. Zhang, T. Zhang, and L. Lu, “BBO crystal component design for ultrashort laser pulse measurement,” *Proc. SPIE*, vol. 9284, p. 92840B, 2014.

[167] J. yuan Zhang, J. Y. Huang, H. Wang, K. S. Wong, and G. K. Wong, “Second-harmonic generation from regeneratively amplified femtosecond laser pulses in BBO and LBO crystals,” *J. Opt. Soc. Am. B*, vol. 15, p. 200, 1998.

[168] S. Skruszewicz, J. Passig, A. Przystawik, N. X. Truong, M. Kötter, J. Tiggesbäumker, and K.-H. Meiwes-Broer, “A new design for imaging of fast energetic electrons,” *Int. J. Mass. Spectr.*, vol. 365-366, p. 338, 2014.

[169] G. Gademann, Y. Huismans, A. Gijsbertsen, J. Jungmann, J. Visschers, and M. J. J. Vrakking, “Velocity map imaging using an in-vacuum pixel detector,” *Rev. Sci. Instrum.*, vol. 80, p. 103105, 2009.

[170] A. Oelsner, O. Schmidt, M. Schicketanz, M. Klais, G. Schönhense, V. Mergel, O. Jagutzki, and H. Schmidt-Böcking, “Microspectroscopy and imaging using a delay line detector in time-of-flight photoemission microscopy,” *Rev. Sci. Instrum.*, vol. 72, p. 3968, 2001.

[171] C. Bordas, F. Pauling, H. Helm, and D. L. Huestis, “Photoelectron imaging spectrometry: Principle and inversion method.,” *Rev. Sci. Instrum.*, vol. 67, p. 2257, (1996).

[172] S. Keller, *Resonante Auger-Raman-Spektroskopie als Untersuchungsmethode von dynamischen Prozessen bei Adsorbatsystemen*. PhD Dissertation, Technische Universtität München, 1998.

[173] J. J. Yeh and I. Lindau, "Atomic subshell photoionization cross-sections and asymmetry parameters," *At. Data Nucl. Data Tables*, vol. 32, p. 1, 1985.

[174] C. U. S. Larsson, A. Beutler, O. Bjorneholm, F. Federmann, U. Hahn, A. Riecs, T. Verbina, and T. Möller, "First results from the high-resolutiopn xuv undulator beamline BW3 at hasylab," *Nucl. Instr. Meth. Phys. Res. Sec. A*, vol. 337, p. 603, 1994.

[175] R. Reininger and V. Saile, "A soft-x-ray grating monochromator for undulator radiation," *Nucl. Instr. Meth. Phys. Res. Sec. A*, vol. 288, p. 343, 1990.

[176] D. Kennedy and S. Manson, "Photoionization of noble-gases-cross-sections and angular-distributions," *Phys. Rev. A.*, vol. 5, p. 227, 1972.

[177] J. Cooper and R. N. Zare, "Angular distribution of photoelectrons," *J. Chem. Phys*, vol. 48, p. 942, 1968.

[178] H. A. Bethe and E. E. Salpeter, *Quantum Mechanics of One- and Two-Electron Atoms*. Dover Publications , INC., 2008.

[179] C. J. Dasch, "One-dimensional tomography: a comparison of abel, onion-peeling, and filtered backprojection methods," *Appl. Opt.*, vol. 31, p. 1146, 1992.

[180] G. M. Roberts, J. L. Nixon, J. Lecointre, E. Wrede, and J. R. R. Verlet, "Toward real-time charged-particle image reconstruction using polar onion-peeling," *Rev. Sci. Instrum.*, vol. 80, p. 053104, 2009.

[181] B. Dick, "Inverting ion images without abel inversion: maximum entropy reconstruction of velocity maps," *Phys. Chem. Chem. Phys.*, vol. 16, p. 570, 2014.

[182] M. Deutsch, "Abel inversion with a simple analytic representation for experimental data," *Appl. Phys. Lett.*, vol. 42, p. 237, 1983.

[183] S. Gueron and M. Deutsch, "A fast abel inversion algorithm," *J. Appl. Phys.*, vol. 75, p. 4313, 1994.

[184] G. Pretzler, H. Jäger, T. Neger, H. Philipp, and J. Woisetschläger, "Comparison of different methods of abel inversion using computer simulated and experimental side-on data," *Z. Naturfors.* , vol. 47, pp. 955–970, 1992.

[185] F. Renth, J. Riedel, and F. Temps, “Inversion of velocity map ion images using iterative regularization and cross validation,” *Rev. Sci. Instrum.*, vol. 77, p. 033103, 2006.

[186] J. Winterhalter, D. Maier, J. Honerkamp, V. Schyja, and H. Helm, “Imaging of charged atomic reaction products: Inversion by a two-dimensional regularization method,” *J. Chem. Phys.*, vol. 110, p. 11187, 1999.

[187] M. J. J. Vrakking, “An iterative procedure for the inversion of two-dimensional ion/photoelectron imaging experiments,” *Rev. Sci. Instrum.*, vol. 72, p. 4084, 2001.

[188] F. Süßmann, S. Zherebtsov, J. Plenge, N. G. Johnson, M. Kübel, A. M. Sayler, V. Mondes, C. Graf, E. Rühl, G. G. Paulus, D. Schmischke, P. Swrschek, and M. F. Kling, “Single-shot velocity-map imaging of attosecond light-field control at kilohertz rate,” *Rev. Sci. Instrum.*, vol. 82, p. 093109, 2011.

[189] S. Zherebtsov, T. Fennel, J. Plenge, E. Antonsson, I. Znakovskaya, A. Wirth, O. Herrwerth, F. Süßmann, C. Peltz, I. Ahmad, S. A. Trushin, V. Pervak, S. Karsch, M. J. J. Vrakking, B. Langer, C. Graf, M. I. Stockman, F. Krausz, E. Ruhl, and M. F. Kling, “Controlled near-field enhanced electron acceleration from dielectric nanospheres with intense few-cycle laser fields,” *Nat Phys*, vol. 7, p. 656, 2011.

[190] S. Augst, D. Strickland, D. D. Meyerhofer, S. L. Chin, and J. H. Eberly, “Tunneling ionization of noble gases in a high-intensity laser field,” *Phys. Rev. Lett.*, vol. 63, p. 2212, 1989.

[191] T. Kanai, E. J. Takahashi, Y. Nabekawa, and K. Midorikawa, “Destructive interference during high harmonic generation in mixed gases,” *Phys. Rev. Lett.*, vol. 98, p. 153904, 2007.

[192] J. C. Delagnes and M. A. Bouchene, “Compensation of electron wavepacket spreading with linearly chirped pulses; theoretical analysis,” *J. Phys. B*, vol. 35, p. 1819, 2002.

[193] T.-M. Yan, S. Popruzhenko, M. Vrakking, and D. Bauer, “Low-energy structures in strong field ionization revealed by quantum orbits,” *Phys. Rev. Lett.*, vol. 105, p. 253002, 2010.

[194] S. Petretti, Y. V. Vanne, A. Saenz, A. Castro, and P. Decleva, “Alignment-dependent ionization of $\mathbf{n}_2$, o_2, and co_2 in intense laser fields,” *Phys. Rev. Lett.*, vol. 104, p. 223001, 2010.

[195] D. Pavičić, K. F. Lee, D. M. Rayner, P. B. Corkum, and D. M. Villeneuve, "Direct measurement of the angular dependence of ionization for N_2, O_2, and CO_2 in intense laser fields," *Phys. Rev. Lett.*, vol. 98, p. 243001, 2007.

[196] J. Itatani, J. Levesque, D. Zeidler, H. Niikura, H. Pepin, J. Kieffer, P. Corkum, and D. Villeneuve, "Tomographic imaging of molecular orbitals," *Nature*, vol. 432, p. 867, 2004.

[197] J. Itatani, J. Levesque, D. Zeidler, H. Niikura, P. Corkum, and D. Villeneuve, "Tomographic imaging of molecular orbitals with high-harmonic generation," *Laser Physics*, vol. 15, p. 525, 2005.

[198] C. Vozzi, M. Negro, F. Calegari, G. Sansone, M. Nisoli, S. De Silvestri, and S. Stagira, "Generalized molecular orbital tomography," *Nat. Phys.*, vol. 7, p. 822, 2011.

[199] T. Morishita, A.-T. Le, Z. Chen, and C. D. Lin, "Accurate retrieval of structural information from laser-induced photoelectron and high-order harmonic spectra by few-cycle laser pulses," *Phys. Rev. Lett.*, vol. 100, p. 013903, 2008.

[200] C. I. Blaga, J. Xu, A. D. DiChiara, E. Sistrunk, K. Zhang, P. Agostini, T. A. Miller, L. F. DiMauro, and C. D. Lin, "Imaging ultrafast molecular dynamics with laser-induced electron diffraction," *Nature*, vol. 483, p. 194, 2012.

[201] T. Zuo, A. Bandrauk, and P. Corkum, "Laser-induced electron diffraction: a new tool for probing ultrafast molecular dynamics," *Chem. Phys. Lett.*, vol. 259, p. 313, 1996.

[202] Z. Chen, A.-T. Le, T. Morishita, and C. D. Lin, "Quantitative rescattering theory for laser-induced high-energy plateau photoelectron spectra," *Phys. Rev. A*, vol. 79, p. 033409, 2009.

[203] "National institute of standarts and technology." `http://www.nist.gov/`. Accessed: 2014-09-30.

[204] M. Y. Ivanov. Private communication, Imperial College London, 2014.

[205] I. Bocharova, R. Karimi, E. F. Penka, J.-P. Brichta, P. Lassonde, X. Fu, J.-C. Kieffer, A. D. Bandrauk, I. Litvinyuk, J. Sanderson, and F. Légaré, "Charge resonance enhanced ionization of co_2 probed by laser coulomb explosion imaging," *Phys. Rev. Lett.*, vol. 107, p. 063201, 2011.

[206] M. Boyle, M. Hedén, C. P. Schulz, E. E. B. Campbell, and I. V. Hertel, "Two-color pump-probe study and internal-energy dependence of rydberg-state excitation in C_{60}, journal = Phys. Rev. A, volume = 70, pages = 051201, year = 2004,,"

[207] J. O. Johansson, G. G. Henderson, and E. E. B. Campbell, "Dynamics of thermal electron emission from highly excited C_{60}," *J. Phys. Chem. A*, vol. 118, p. 8067, 2014.

[208] H. Li, B. Mignolet, G. Wachter, S. Skruszewicz, S. Zherebtsov, F. Süßmann, A. Kessel, S. A. Trushin, N. G. Kling, M. Kübel, B. Ahn, D. Kim, I. Ben-Itzhak, C. L. Cocke, T. Fennel, J. Tiggesbäumker, K.-H. Meiwes-Broer, C. Lemell, J. Burgdörfer, R. D. Levine, F. Remacle, and M. F. Kling, "Coherent electronic wave packet motion in c_{60} controlled by the waveform and polarization of few-cycle laser fields," *Phys. Rev. Lett.*, vol. 114, p. 123004, 2015.

[209] K. Hansen, K. Hoffmann, and E. E. B. Campbell, "Thermal electron emission from the hot electronic subsystem of vibrationally cold C_{60}," *J. Chem. Phys.*, vol. 119, p. 2513, 2003.

[210] J. O. Johansson, G. G. Henderson, F. m. c. Remacle, and E. E. B. Campbell, "Angular-resolved photoelectron spectroscopy of superatom orbitals of fullerenes," *Phys. Rev. Lett.*, vol. 108, p. 173401, 2012.

[211] M. Boyle, K. Hoffmann, C. P. Schulz, I. V. Hertel, R. D. Levine, and E. E. B Campbell, "Excitation of rydberg series in C_{60}," *Phys. Rev. Lett.*, vol. 87, p. 273401, 2001.

[212] E. E. B. Campbell, K. Hansen, K. Hoffmann, G. Korn, M. Tchaplyguine, M. Wittmann, and I. V. Hertel, "From above threshold ionization to statistical electron emission: The laser pulse-duration dependence of C_{60} photoelectron spectra," *Phys. Rev. Lett.*, vol. 84, p. 2128, 2000.

[213] E. E. B. Campbell, Hoffmann, and I. V. Hertel, "Transition from direct to delayed ionisation of C_{60}," *Eur. Phys. J. D*, vol. 16, p. 345, 2001.

[214] M. Feng, J. Zhao, and H. Petek, "Atomlike, hollow-core-bound molecular orbitals of C_{60}," vol. 320, p. 359, 2008.

[215] G. P. Zhang, H. P. Zhu, Y. H. Bai, J. Bonacum, X. S. Wu, and T. F. George, "Imaging superatomic molecular orbitals in a C_{60} molecule through four 800-nm photons," *arXiv:1504.06899.*

[216] M. A. Almajid. Private communication, Universität Rostock, 2015.

[217] T. Fennel. Private communication, Universität Rostock, 2015.

[218] J. W. Liang and F. X. Kärtner, "Two-color-laser-driven direct electron acceleration in infinite vacuum," *arXiv:1311.5791*, 2010.

[219] T. Döppner, J. P. Müller, A. Przystawik, S. Göde, J. Tiggesbäumker, K.-H. Meiwes-Broer, C. Varin, L. Ramunno, T. Brabec, and T. Fennel, "Steplike intensity threshold behavior of extreme ionization in laser-driven xenon clusters," *Phys. Rev. Lett.*, vol. 105, p. 053401, 2010.

[220] N. X. Truong, P. Hilse, S. Göde, A. Przystawik, T. Döppner, T. Fennel, T. Bornath, J. Tiggesbäumker, M. Schlanges, G. Gerber, and K. H. Meiwes-Broer, "Optimal control of the strong-field ionization of silver clusters in helium droplets," *Phys. Rev. A*, vol. 81, p. 013201, 2010.

[221] A. Przystawik, S. Göde, T. Döppner, J. Tiggesbäumker, and K.-H. Meiwes-Broer, "Light-induced collapse of metastable magnesium complexes formed in helium nanodroplets," *Phys. Rev. A*, vol. 78, p. 021202, 2008.

[222] J. Tiggesbäumker and S. Frank, "Formation and properties of metal clusters isolated in helium droplets," *Phys.Chem. Chem. Phys.*, vol. 9, p. 4748, 2007.

[223] R. Schmidt. Private communication, Technische Universität Dresden, 2015.

Scientific collaborations

Control of the electron acceleration in Ag clusters with few-cycles CEP laser pulses

Collaborators	M.F. Kling
Facility	AS5 at MPQ in Garching
Time period	July 2012-April 2012

Angular-resolved photoemission from atoms ionized with 6 μm CEP stabilized few-cycle laser pulses

Collaborators	A. Alnaser
Facility	MPQ in Garching
Time period	November/December 2012

Angular-resolved photoemission from C_{60} with few-cycle CEP laser pulses

Collaborators	M. F. Kling
Facility	AS5 at MPQ in Garching
Time period	Juli/August 2012

Thomson scattering on Hydrogen droplets studied with XUV pulses

Collaborators	R. Redmer, Th. Tschenscher
Facility	FLASH DESY Hamburg
Time period	September 2009 - January 2013

Ionization of C_{60} with XUV pulses

Collaborators	T. Laarmann
Facility	FLASH DESY Hamburg
Time period	July 2014

Warm dense matter investigation with Hydrogen Droplets

Collaborators	S. Glenzer
Facility	MEC at SLAC in Menlo Park
Time period	July/August 2014

X-ray scattering on nanoplasma in Ag clusters

Collaborators	T. Döppner
Facility	AMO at SLAC in Menlo Park
Time period	July - 2015 - now

Formation of coherent rotational wavepackets in small molecule-helium clusters using impulsive alignment

Collaborators	K. v. Haeften
Facility	AG Cluster und Nanostrukturen
Time period	October-2012 - January-2013

Efficient photocatalytic hydrogen production using metal nanoparticles created by femtosecond laser ablation

Collaborators	S. Wohlrab
Facility	LIKAT in Rostock
Time period	January-2013 - January-2015

Generation of metal nanoparticles by femtosecond laser ablation

Collaborators	R. Peters
Facility	GSI SLV in Rostock
Time period	January-2013 - January-2015

REXUS/BEXUS *in-situ* study of mesospheric turbulences

Collaborators	A. Szewczyk
Facility	IAP in Kühlungsborn, DLR Oberphaffenhoffen
Time period	October 2012 - Juni 2013

Calibration of vacuum ultraviolet flash lamps

Collaborators	M. R. Saraji-Bozorgzad, R. Zimmermann
Facility	AG Cluster und Nanostrukturen
Time period	December 2012 - November 2011

Calibration of vacuum ultraviolet xenon flash lamps used for photoionization of meteor smoke particles

Collaborators	M. Rapp
Facility	IAP in Kühlungsborn
Time period	July 2009 - January-2011

C_{60} meeting in Rostock University

Organizator	S. Skruszewicz,
Guests	E.E.B. Cambpell, F. Remarkle, M.F. Kling
Date	17.01.12013

List of publications

1. *Two-Color Strong-Field Photoelectron Spectroscopy and the Phase of the Phase*, S. Skruszewicz, J. Tiggesb/"aumker, K.-H. Meiwes-Broer, M. Arbeiter, Th. Fennel adn D. Bauer, *Phys. Rev. Lett.*, **115**, 043001 (2015)

2. *A new design for imaging of fast energetic electrons*, S. Skruszewicz, J. Passig, A. Przystawik, N. X. Truong, M. Kötter, J. Tiggesbäumker and K.-H. Meiwes-Broer, *Int. J. Mass. Spec.*, **365-366**, 338 (2014)

3. *Coherent Electronic Wave Packet Motion in* C_{60} *Controlled by the Waveform and Polarization of Few-Cycle Laser Fields*, H. Li, B. Mignolet, G. Wachter, S. Skruszewicz, S. Zherebtsov, F. Süßmann, A. Kessel, S. A. Trushin, Nora G. Kling, M. Kübel, B. Ahn, D. Kim, I. Ben-Itzhak, C. L. Cocke, T. Fennel, J. Tiggesbäumker, K.-H. Meiwes-Broer, C. Lemell, J. Burgdörfer, R. D. Levine, F. Remacle, and M. F. Kling *Phys. Rev. Lett*, **114**, 123004 (2015)

Conference talks

1. *Strong field ionization in* ω-2ω *laser pulses: phase-of-the-phase spectroscopy*

   DPG Frühjahrstagung, 2015, Heidelberg, Deutschland.

2. *Can we see electron trajectories ?*
   Treffen des Graduiertennetzwerkes "Life, Light and Matter", 2014, Rostock, Deutschland.

3. *Ionization dynamics of atoms and molecules in sculpted two-color laser fields*

   DPG Frühjahrstagung, 2014, Berlin, Deutschland.

4. *Angular resolved photoionization study of* C_{60} *in ultrashort (4 fs) and short (40 fs) laser pulses*

   DPG Frühjahrstagung, 2013, Hannover, Deutschland.

5. *Controlled photoemission from fullerene molecule in two-color laser pulses*
   C_{60} Meeting, 2013, Rostock, Deutschland.

6. *Efficient photocatalytic hydrogen production using metal nanoparticles created by femtosecond laser ablation*
   Treffen des Graduiertennetzwerkes "Life, Light and Matter", 2013, Rostock, Deutschland.

7. *Asymmetrical photoemission from fullerene molecule*
   GDK Seminar, 2012, Rostock, Deutschland.

8. *Correlation in the multiphoton ionization of fullerenes and clusters*
   Treffen des Graduiertennetzwerkes "Life, Light and Matter", 2010, Rostock, Deutschland.

9. *Characteristics of High Energy Velocity Map Imaging (HEVMI) spectrometer designed to study electron emission from clusters in strong laser fields*
   DPG Frühjahrstagung, 2010, Hannover, Deutschland.

10. *Angular resolved photoemission from Xenon and* C_{60}
    DPG Frühjahrstagung, 2009, Hamburg, Deutschland.

Erklärung

gemäß §4 der Promotionsordnung
der Mathematisch-Naturwissenschaftlichen Fakultät
der Universität Rostock

Ich gebe folgende Erklärung ab:

1. Die Gelegenheit zum vorliegenden Promotionsvorhaben ist mir nicht kommerziell vermittelt worden. Insbesondere habe ich keine Organisation eingeschaltet, die gegen Entgelt Betreuerinnen/Betreuer für die Anfertigung von Dissertationen sucht oder die mir obliegenden Pflichten hinsichtlich der Prüfungsleistungen für mich ganz oder teilweise erledigt.
2. Ich versichere hiermit an Eides statt, dass ich die vorliegende Arbeit selbstständig angefertigt und ohne fremde Hilfe verfasst habe. Dazu habe ich keine außer den von mir angegebenen Hilfsmitteln und Quellen verwendet und die den benutzten Werken inhaltlich und wörtlich entnommenen Stellen habe ich als solche kenntlich gemacht.

Rostock, den 21.08.2015

Slawomir Skruszewicz

Acknowledgements

I would like to express my deepest thanks to Prof. Karl-Heinz Meiwes-Broer for giving me opportunity to work in excellently equipped lab in exciting field of science. Especially i am gratefull for freedom, trust, support and practically unlimited resources to realize many ideas during my PhD time. I appreciate excellent conditions offered by SFB 625 which supports all experiments, collaborations and conferences.

I deeply appreciate deep scientific supervision and collaboration with Josef Tiggesbäumker, for countless discussions and ideas which inspired this work (and many others) and made final result visible. I am gratefull not only for always being open for discussion and help but also for musical inspirations, mini-performances and playing together music composed by Josef !

I am deply indebted to Prof. Dieter Bauer who occupies a central position in ω-2ω project. It is a great adventure and luck to have opportunity to work together. Since beginning of the project Prof. Bauer guides me through strong laser physics ' seen from electron point of view'. I appreciate time he spend to explain, and support me with programs which enable to calculate and understand dynamics of electron in oscillatory laser field, ideas and inspirations for experiments. Without his strong support, motivations and crucial idea to model spectra with SMT results of this work would still be very elusive.

It is a pleasure to appreciate collaboration with Prof. Thomas Fennel and Mathias Arbeiter who spend countless hours to calculate TDSE spectra in our project. Thomas is driving force of this project and inspired me at many points of my adventure with physics.

I spend few wonderful years of my life in friendly and inspiring environment of work group AG Cluster and Nanostructures where I met many friends and authorities. This thesis is sum of all my experience I gain during participating in numbers of experiments, group meeting, conversations with many generation of physicists whom I encountered here. I would like to thank people who guided me through world of experimental physics at the beginning of my story in Rostock, especially Johannes Passig, Volkmar Senz, Sebastian Göde and Andreas Przystawik for solid education in lab. I am obligated to Robert Irsig who prepared a laser system for many experiments, and for collaboration at

projects in Garching, Hamburg and LIKAT in Rostock. I appreciate working with Mohammad Adel Almajid who perform many SFA simulation for me. I would like to thank to my colleagues Dzmitr Komar, Lev Kazak, Michael Kelbg, Patrice OelÃ§ner, Stefan Bartling, Hannes Hartman, Michael Kötter, Franklin Martinez, Christian Peltz, Mathias Arbeiter, Madlen Müller for friendly atmosphere and support of my work. I hope this is the right point to acknowledge many generation of physicists who contributed to development of the group and left their fingerprints so further generations can benefit from them.

I am appreciated to acknowledge representative for all collaborators of many project, should be mentioned in connection with:

- MPQ Garching Prof. Matthias Kling for offering me opportunity to work in one of the greatest labs I ever entered. During my stay at MPQ i got familiar not only with CEP technology but also with many experimental techniques and procedures to analyze phase-dependent signals which i could applied in our experiments. Matthias Kling also introduced us to w2w technology and contribute to firrst experiments on clusters. I enjoyed to work together with Sergey Zherebtsov, Hui Li, Ali Alnaser, Yunpei Deng and Boris Berques and thank to all of you for great time in lab !

- FLASH at DESY in Hamburg for Tim Laarmann, Thomas Tschentcher, Sven Toleikis, Ulf Zastrau for great period of research on Thomson Scattering on Hydrogen droplets. We spend many months in Lab, often during night shifts hunting for elusive plasmons signals.

- MEC Team led by Prof. Siegfried Glenzer for inviting me tocollaboration in world-leading scientific center at SLAC in Menlo Park. It was for me a completely new piece of physics with only a dozen of laser shots but very exciting and inspiring.

- AMO collaboration leaded by Tilo Döppner, Christoph Bostedt and Thomas Fennel for inviting me to another great lab at SLAC where we could together once more look into the world of cluster physics but in completely new light !

- GSI SLV lead by Rigo Peters for offering practically unlimited access to laser facility where we could investigate generation of nanoparticles by laser ablation. At this place I would like to acknowledge Rafael Da Silva from group of Sebastian Wohlrab in LIKAT in Rostock for great 'coffee idea' which brought us close (and hopefully entire world) to sources of hydrogen generated in catalytic reactions using metal nanoparticles generated in laser ablation.

- IAP Kühlungsborn Prof. Markus Rapp (currently at DLR Oberpfaffenhoffen) and Artur Szewczyk. Markus Rapp was my second supervisor during sholarship time of Interdisciplinary Faculty Life, Light and Matter. Artur invite me to the most crazy and inspiring project I ever participated namely shooting a rocket into mesosphere in REXUS/BEXUS Project at DLR in Oberpfaffenhoffen.

Our work wouldn't be possible without our administration. I would like to acknowledge excellent work of Mechanical Workshops under division of Frank Richter and other colleagues for unlimited support. I extend my thanks to our electronics master Jan Ditrich for outstanding help. Smooth operation of most important administrative tasks wouldn't be possible without Annika Machotzek.

I am happy to have many friends in Rostock whom i would like to thanks: Johannes, Joanna, Artur, Mateusz, Teresa, Rafael. Many firends left already Rostock but i thank you guys for being here.

Finally, i would like to thanks to my familly for support and visiting me in Rostock. Final stage of my work wouldn't be possible without Malgosia and Alina and i would like thank them for love and patience.